January 2015

Phase Field Modeling of Grain Growth in Porous Polycrystalline Solids

Karim Ahmed
Purdue University

Graduate School Form 30
Updated 1/15/2015

PURDUE UNIVERSITY
GRADUATE SCHOOL
Thesis/Dissertation Acceptance

This is to certify that the thesis/dissertation prepared

By Karim Ahmed

Entitled

Phase Field Modeling of Grain Growth in Porous Polycrystalline Solids

For the degree of Doctor of Philosophy

Is approved by the final examining committee:

Anter El-Azab Chair	Edwin Garcia
Ahmed Hassanein	
Allen Garner	
Marisol Koslowski	

To the best of my knowledge and as understood by the student in the Thesis/Dissertation Agreement, Publication Delay, and Certification Disclaimer (Graduate School Form 32), this thesis/dissertation adheres to the provisions of Purdue University's "Policy of Integrity in Research" and the use of copyright material.

Approved by Major Professor(s): Anter El-Azab

Approved by: Ahmed Hassanein 9/23/2015

Head of the Departmental Graduate Program Date

PHASE FIELD MODELING OF GRAIN GROWTH IN POROUS POLYCRYSTALLINE SOLIDS

A Dissertation

Submitted to the Faculty

of

Purdue University

by

Karim E Ahmed

In Partial Fulfillment of the

Requirements for the Degree

of

Doctor of Philosophy

December 2015

Purdue University

West Lafayette, Indiana

For my family and friends

ACKNOWLEDGEMENTS

First, I would like to express my sincere gratitude to my advisor, Professor Anter El-Azab, for his guidance, patience, and continuous support. He has constantly provided me with all possible kinds of help over all these years. He consistently encouraged me to explore and learn new things and work on challenging research topics. I would like to thank him for valuable tips and fruitful discussions. Without his help and support this dissertation would not have been possible.

I would like to thank Prof. Amr Mohamed for encouraging me to pursue graduate studies. He has generously offered me all kinds of advice and help. He has positively influenced my perspective on life. My feeling of gratitude towards him is beyond words.

I would like to thank Prof. Ahmed Hassanein, Prof. Allen Garner, Prof. Marisol Koslowski, and Prof. Edwin Garcia for serving on my Ph.D. committee. I am very grateful to them for their valuable feedback and inputs which have helped me improve this dissertation.

I would also like to thank Dr. Michael Tonks and Dr. Yongfeng Zhang for kindly hosting me at Idaho National Laboratory during the spring and summer semesters of 2015. Thanks are also due to the members of the Computational Microstructure Science Group for their help and encouragement, especially during my early days of learning MOOSE and MARMOT. During my stay at Idaho Falls, I enjoyed the discussions of

research ideas with every member of this group, the group meetings and lunches, and the unique scenic beauty of Idaho.

Financial support for most part of this dissertation was provided through the Center for Materials Science of Nuclear Fuel, an Energy Frontier Research Center funded by the U.S. Department of Energy, Office of Sciences, Office of Basic Energy Sciences under award number FWP 1356, through subcontract number 00122223 at Purdue University. In addition, support provided by the Nuclear Energy Advanced Modeling and Simulation (NEAMS) program during my internship at Idaho National Laboratory is also duly acknowledged. A word of thanks is also due to the Fuel Modeling and Simulation Department at Idaho National Laboratory for hosting me and allowing me to use their HPC facilities where several simulations presented in this work were performed.

TABLE OF CONTENTS

Page

ABSTRACT

Ahmed, Karim E. Ph.D., Purdue University, December 2015. Phase Field Modeling of Grain Growth in Porous Polycrystalline Solids. Major Professor: Anter El-Azab.

The concurrent evolution of grain size and porosity in porous polycrystalline solids is a technically important problem. All the physical properties of such materials depend strongly on pore fraction and pore and grain sizes and distributions. Theoretical models for the pore-grain boundary interactions during grain growth usually employ restrictive, unrealistic assumptions on the pore and grain shapes and motions to render the problem tractable. However, these assumptions limit the models to be only of qualitative nature and hence cannot be used for predictions. This has motivated us to develop a novel phase field model to investigate the process of grain growth in porous polycrystalline solids. Based on a dynamical system of coupled Cahn-Hilliard and Allen-Cahn equations, the model couples the curvature-driven grain boundary motion and the migration of pores via surface diffusion. As such, the model accounts for all possible interactions between the pore and grain boundary, which highly influence the grain growth kinetics. Through a formal asymptotic analysis, the current work demonstrates that the phase field model recovers the corresponding sharp-interface dynamics of the co-evolution of grain boundaries and pores; this analysis also fixes the model kinetic parameters in terms of real materials properties. The model was used to investigate the effect of porosity on the

kinetics of grain growth in UO_2 and CeO_2 in 2D and 3D. It is shown that the model captures the phenomenon of pore breakaway often observed in experiments. Pores on three- and four- grain junctions were found to transform to edge pores (pores on two-grain junction) before complete separation. The simulations demonstrated that inhomogeneous distribution of pores and pore breakaway lead to abnormal grain growth. The simulations also showed that grain growth kinetics in these materials changes from boundary-controlled to pore-controlled as the amount of porosity increases. The kinetic growth parameters such as the growth exponent and the rate constant (or equivalently the activation energy) were found to depend strongly on the precise amount and distribution of porosity, which reconciles the different experimental results reported for grain growth in such materials.

CHAPTER 1. INTRODUCTION

1.1 Motivation and Objectives

All physical properties of polycrystalline solids such as yield stress, fracture strength, electrical breakdown strength, dielectric constant, etc. are strongly dependent on the grain size [1, 6]. This is due to the prominent role of grain boundaries in influencing material properties [1, 64, 155, and 156]. Samples with smaller grain size have higher grain boundary area per unit volume. Moreover, controlling grain growth is crucial for achieving the desired density for ceramics during sintering [1]. Larger grain size means longer diffusion path for atoms and/or point defects before reaching the pores, which are usually located on the grain boundaries during the final stage of sintering [1, 46-53]. This hinders the pore shrinkage rate and hence retards the densification process [1, 155]. Furthermore, it was found out that the performance of several structural materials under extreme conditions, such as irradiation, high temperature, high stresses, etc., depends strongly on the grain size [1, 155, and 156]. For example, it is widely accepted that nanocrystalline materials are more radiation tolerant than regular polycrystalline materials with micron size grains [155, 156]. This is attributed to the fact that grain boundaries act as sinks for point defects impairing their ability to form detrimental microstructural features such as voids and dislocation loops which inversely affect the physical properties of materials [62, 154-156]. In another situation, it was found out that

fission gas swelling and release in irradiated uranium dioxide, the main nuclear fuel, decrease with increasing grain size [7, 155]. Therefore, investigating the process of grain growth is of paramount importance for different technological and industrial applications.

For grain growth in pure and fully-dense solids, which is usually termed *ideal grain growth*, the classical models by Burke and Turnbull [3], Mullins [4], and Hillert [5] demonstrate that grain boundary motion is a mean-curvature driven motion [65], meaning that the grain boundary velocity is proportional to the mean curvature of the grain boundary. This gives rise to the well-known parabolic kinetics for the average grain size [1-5]. However, modeling the process of grain growth kinetics in porous polycrystalline solids is more complicated by the interaction between the grain boundaries and pores in such materials [1, 46-58]. Basically, the pores exert a drag force on the grain boundaries and hinder their motion, thereby retarding the grain growth process. This pore-induced retardation of grain growth is an example of the so-called *particle-inhibited grain growth* [1]. Furthermore, nearby pores can in some cases merge together (coalesce) as they move along grain boundaries, and thus they themselves contribute to reduction of the interfacial free energy in solids. The concurrent pore coalescence and grain growth is known to proceed during the final stage of sintering in porous solids [1, 46-58].

The first models to investigate the effect of pores on grain growth were proposed by Nichols [46], Brook [47], and Carpay [48]. These models assume the microstructure to be homogeneous. Therefore, they only considered an isolated pore on a grain boundary and assumed the deduced kinetics represents the average kinetics of the whole system. Moreover, these models assume nearly spherical pores that can only move along with the boundary as a rigid body without changing their shape. They also neglect pore

coalescence that usually takes place simultaneously with grain growth. Such simplified models succeeded at least qualitatively in describing some aspects of the physics of the process that were observed experimentally [1]. Nonetheless, the quantitative results of these models did not agree well with the experimental data. This discrepancy was primarily attributed to the absence of the details of the pore and grain boundary geometries in these models.

In order to alleviate the shortcomings of the above mean-field models, spatiotemporal models were proposed to take into consideration the details of the geometry of the pore and the boundary, and hence capture the nature of the heterogeneous structure of the system [49-55]. Evans and co-workers [49, 50] and later Riedel and Svoboda [51, 52] formulated the sharp-interface description of the problem. These sharp-interface models gave new insights that could not be gained from the classical models. For instance, it has been demonstrated that the possibility of pore separation depends strongly on the pore configuration. Higher-order pore configurations (pores on three-, and four-grain junctions) never separate directly from the migrating boundary. Instead, they transform into edge pores (pores on two-grain junctions) before breakaway. However, as it is well-known for all sharp-interface models, the task of solving these models numerically is cumbersome. In particular, applying the boundary conditions for general pore/grain configurations and the criterion of pore separation is complicated [49-52]. In fact, only 2D numerical simulations have been conducted since Evans and co-workers introduced their formulation [49, 50] nearly three decades ago. Only recently, Barrett et al. [67] presented the first 3D solution of coupled surface and grain boundary motion. However, that study was limited to bi- and tri-crystals with

applications only to thermal grooving and sintering of two unequal-sized particles. Large scale 3D simulations of grain growth in porous polycrystalline solids based on the sharp-interface model have not been attempted yet. With this in mind, the motivation for developing a phase field (diffuse-interface) model of the problem is obvious.

1.2 Contributions to Research

In this work, the first phase field (diffuse-interface) model for grain growth in porous polycrystalline solids was developed. The phase field model relaxes all the restrictive assumptions employed in the classical and sharp-interface models. It provides insight into the dynamics of the pore-grain boundary interactions which influence the overall grain growth kinetics. The model captures the coevolution of porosity and grain size, and hence represents the microstructure evolution in porous polycrystalline solids during the final stage of sintering. The model has been applied to investigate grain growth in uranium dioxide and ceria. The model results agree well with published experimental studies of grain growth in these materials [56-58]. The details of the contributions of this work are the following:

- The pore-grain boundary interactions complicate the investigation of grain growth in porous polycrystalline solids. Here, we present a novel phase field model that captures all possible pore-grain boundary interactions in a straightforward manner. Phase field models for sintering [74-76], ideal grain growth [70, 71], and the effect of solute segregation and immobile second-phase particles on the kinetics of grain growth [124-127] have appeared before in the literature. However, a phase field model of the effect of mobile particles such as pores on the kinetics of grain growth was never developed before. The current work represents the first

application of this modeling approach to study the process of grain growth in porous polycrystalline solids.

- By using a formal asymptotic analysis of the current phase field model, it was demonstrated that it recovers the well-known sharp-interface dynamics of the coevolution of pores and grains [49-52]. Performing such analysis has two major benefits. First, it proves the consistency of using a phase field (diffuse-interface) to represent inherently sharp interfaces (e.g., grain boundaries and free surfaces). Second, it establishes direct relations between the phase field model parameters and the regular thermodynamic and kinetic parameters that appear in the sharp-interface models. Such relations render the phase field model quantitative, which facilitates comparison with experiments. Indeed, the model results for grain growth in ceria and uranium dioxide shows good agreement with experiments.
- The model equations were solved numerically using two distinct techniques. First, a standard explicit finite-difference scheme was employed using in-house codes written in FORTRAN 90. Then, a fully-coupled, fully-implicit finite-element scheme was implemented using MARMOT, the mesoscale simulator developed at Idaho National Laboratory [123]. The results obtained from the two schemes were consistent, raising the confidence in the model formulation and implementation. The current phase field model, which is now part of MARMOT framework, will be used to investigate the effect of microstructure evolution on the nuclear fuel performance.
- The 3D simulations presented here are the first general 3D simulations of grain growth in porous polycrystalline solids in the literature. The 3D simulations

demonstrated that the effect of pore drag on the grain growth kinetics is exaggerated in the 2D simulations. This is due to the fact that 2D simulations, which implicitly assume cylindrical shapes for the pores and grains, overestimate the contact area between the pore and the grain boundary. Therefore, performing 3D simulations is necessary for obtaining accurate grain growth rates.

1.3 Dissertation Layout

First, the technical background related to the grain growth process and phase field modeling approach is reviewed in Chapter 2. In the first part of the review, the process of grain growth in fully-dense and porous polycrystalline solids is discussed. The different theoretical models developed for investigating the grain growth process are summarized. In the second part of the review, the general concepts of the phase field method are introduced.

Chapter 3 presents the development of the phase field model for grain growth in porous polycrystalline solids. First, the thermodynamic and kinetic formulations are introduced. Then, the procedure for determining the model parameters is discussed. Lastly, the details of the numerical implementation are highlighted.

In Chapter 4, the results obtained by solving the phase field model are presented and discussed. Test cases for benchmarking the model were performed first. Then, a quantitative investigation of the effect of pore drag on the grain growth kinetics, using idealized 2D pore and grain shapes, was performed. General 2D and 3D simulations of grain growth in porous polycrystalline solids such as uranium dioxide and ceria are then analyzed.

Finally, Chapter 5 summarizes the research conducted in this study and sheds light on possible directions for future research. Parts of this dissertation have been published in Ahmed k et al. [56-58, 62, 159].

CHAPTER 2. TECHNICAL BACKGROUND

This chapter presents the essential background for investigating the process of grain growth in porous solids using the phase field approach. In the first section, the underlying physics of the problem of grain growth in solids is discussed. In the second section, the basic ingredients of the phase field approach will be summarized in preparation for introducing the novel phase field model for grain growth in porous polycrystalline solids in the next chapter.

2.1 Grain Growth in Polycrystalline Solids

Grain growth takes place in polycrystalline solids at sufficiently high temperature [1-5]. The driving force for grain growth is the decrease in the interfacial free energy via the reduction of the total grain boundary area. During grain growth, the number of grains decreases and hence the average grain size of a polycrystalline solid increases. From atomistic point of view, grain growth proceeds as atoms diffuse less than an interatomic distance from one side of the boundary to the other side resulting in the movement of grain boundary in the opposite direction. This picture is illustrated schematically in Figure 2.1. The atoms move from the higher curvature (and hence higher chemical potential) “convex” side to the lower curvature “concave” side. Hence the net atomic flux results in the movement of boundary toward its center of curvature.

All physical properties of polycrystalline solids are strongly dependent on the grain size [1]. For example, it is well-known that the yield stress and fracture strength of metals decrease as the grain size increases [6]. It was also shown that the electrical breakdown strength and dielectric constant of most ceramics increase with decreasing the grain size [1]. Moreover, the sintering or densification rate of porous solids is drastically reduced with increasing grain size; hence controlling grain growth is crucial for achieving the desired density for such materials [1]. Furthermore, it was found out that the fission gas swelling and release in irradiated uranium dioxide, the main nuclear fuel, decrease with increasing grain size [7]. Therefore, investigating the process of grain growth is of paramount importance for different technological and industrial applications.

In general, grain growth in solids is classified into two categories: (1) *normal grain growth* and (2) *abnormal grain growth*. Normal grain growth is characterized by a time-invariant grain size distribution since on average all growing gains grow with the same rate. On the other hand, in abnormal grain growth some few gains grow faster than the rest of gains which usually gives rise to a bimodal gain size distribution. Figure 2.2 schematically depicts the difference between the normal and abnormal grain growth. The occurrence of abnormal grain growth is primarily attributed to the anisotropy in grain boundary energy and/or mobility [1]. Grains with boundaries that have a higher mobility or a lower energy than the neighboring grains will grow faster. However, any local inhomogeneity in the microstructure of polycrystalline solids due to the presence of dopants, impurities, inclusions or pores could in turn lead to local changes in the grain boundary energy and/or mobility. Therefore, the presence of such features can also initiate abnormal grain growth [1].

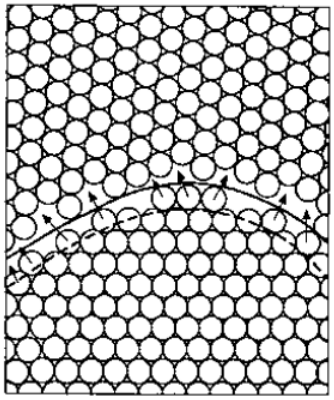

Figure 2.1. A schematic illustration showing the grain boundary migration during grain growth. Due to the difference in curvature (and hence in chemical potential), atoms tend to move from the convex side to the concave side. The net effect is that a boundary moves towards its center of curvature [1].

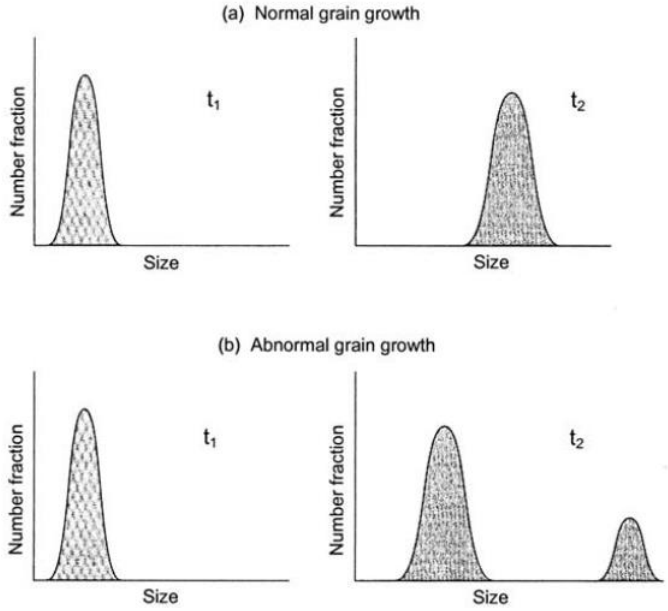

Figure 2.2. Normal versus abnormal grain growth. In normal grain growth, most of the growing grains grow with the same rate leading to a time-invariant distribution. In abnormal grain growth, some grains grow faster than the rest of growing grains resulting in a bimodal distribution at later time [1].

2.1.1 Ideal Grain Growth

As early as 1950, theoretical models were introduced to investigate the process of grain growth in pure, isotropic, and fully dense solids. Grain growth in such materials is commonly known as *ideal grain growth*. The most notable models are the one put forward by Burke and Turnbull [3], Mullins [4], and Hillert [5]. These models invoke the standard principles of linear irreversible thermodynamics to derive the growth kinetics. In such approach, it is assumed that the grain boundary velocity is linearly proportional to the driving force as follows;

$$v_{\mathrm{b}} = M_{\mathrm{b}} F_{\mathrm{b}} . \tag{2.1}$$

In the above, the subscript b denotes the boundary; v is the grain boundary velocity, M is its mobility and F is the driving force. The driving force is the chemical potential difference across the boundary which is assumed to be proportional to its curvature, e.g.,

$$F_{\mathrm{b}} = \frac{\alpha \gamma_{\mathrm{gb}}}{D}, \tag{2.2}$$

where, α is a geometric factor (e.g., α equals 4 for a spherical grain), γ_{gb} is the grain boundary energy, and D is the grain size (diameter). Now, if one approximates the boundary velocity as $v_{\mathrm{b}} \approx dD/dt$ and substitutes by Eq. (2.2) in Eq. (2.1), one obtains

$$\frac{dD}{dt} = \frac{\alpha M_{\mathrm{b}} \gamma_{\mathrm{gb}}}{D}. \tag{2.3}$$

Direct integration of Eq. (2.3) gives the well-known parabolic grain growth kinetics, e.g.,

$$D^2(t) - D_{\circ}^2 = k\,t. \tag{2.4}$$

Here, $D(t)$ is the grain size at time, t , $D_{\circ}$ is the initial grain size and $k = 2\alpha \gamma_{\mathrm{gb}} M_{\mathrm{b}}$ is the rate constant.

The initial derivation by Burke and Turnbull [3] considered only one grain and assumed that the final result can still be valid to represent the average kinetics for a system of grains. Using a mean-field theory, Hillert generalized the analysis to the case of a system with a distribution of grain sizes [5]. In this case, the grain size that appears in Eq. (2.4) is the average grain size. Hillert's analysis basically showed that the curvature-driven grain growth follows the boundary-controlled Lifshitz-Slyozov-Wagner (LSW) theory [1, 8, 9].

While the above mentioned models only address the curvature-driven grain growth, Eq. (2.1) is also valid to study other driving forces. Stress and temperature gradient were also proposed in literature as driving forces [10-12]. However, it was concluded that curvature is usually the dominant driving force for grain growth in solids at temperatures of interest. One also should note that grain rotation could provide another mechanism for the reduction of grain boundary energy in anisotropic materials [13-16]. In such materials, the grain boundary energy is function of the misorientation between the grains and hence the system can simply decreases its interfacial energy by rotating the grains to minimize the misorientation. Nonetheless, it was found out that for micron-size or larger grains the grain rotation rate is much smaller than the grain boundary migration rate [16].

Several computational models were proposed to simulate the curvature-driven grain growth process. The most common of these models are the Monte Carlo Potts models [17-21], front tracking methods [22, 23], vertex models [24-28], cellular automata [29, 30] and phase field models [31-35]. For such ideal grain growth in pure solids, these models, in spite of their differences, reach the same conclusions that were reached by the classical theories on the kinetics of grain growth [3-5]. In particular, these models confirmed the

parabolic growth law and the existence of time-independent grain size distribution in the scaling regime.

Many experimental studies of grain growth in solids, however, reported deviations from the parabolic growth kinetics [1, 36-40]. Such deviations were primarily attributed to the presence of second-phase particles (precipitates/inclusions) or pores. Such particles exert a drag force on the grain boundary which hinders its motion, and hence retards the overall grain growth rate. Grain growth under such situations is commonly called *particle-inhibited grain growth* [1].

2.1.2 Particle-Inhibited Grain Growth

In order to investigate the so-called particle-inhibited grain growth, new theoretical models were then proposed [1]. These models can be classified into two categories depending on whether the particles are treated as mobile or immobile. Second-phase particles are usually considered immobile while pores are often considered mobile.

2.1.2.1 Zener's Pining Model for Immobile Particles

The effect of immobile particles on the grain growth process was first tackled by Zener [1, 41]. He considered the particles to be immobile, spherical, mono-size, insoluble, and randomly distributed in the polycrystalline solid. Zener considered the curvature to be the driving force for the boundary motion. Hence, Eq. (2.2) is valid to represent the driving force of the particle-free boundary, F_{b} . However, the presence of the particles exerts a drag force on the boundary that hinders its motion. This is schematically depicted in Figure 2.3. The drag force is given by

$$F_{\mathrm{d}} = 2\pi r \gamma_{\mathrm{gb}} \cos\theta \sin\theta \,. \tag{2.5}$$

Here, r is the particle radius and θ is the contact (drag) angle (see Figure 2.3). The retarding force is maximum when $\theta = 45^\circ$. The maximum drag force, $F_{\mathrm{d}}^{\max}$ experienced by the boundary due to the presence of N_{A} particles per unit area of the boundary is then,

$$F_{\mathrm{d}}^{\max} = N_{\mathrm{A}} \pi r \gamma_{\mathrm{gb}} . \tag{2.6}$$

For randomly distributed spherical particles, N_{A} can be simply expressed in terms of the particle volume fraction, f and Eq. (2.6) becomes [1]

$$F_{\mathrm{d}}^{\max} = \frac{3 f \gamma_{\mathrm{gb}}}{2r} . \tag{2.7}$$

From Eq. (2.2) and Eq. (2.7), the net driving force of the boundary is

$$F_{\mathrm{net}} = F_{\mathrm{b}} - F_{\mathrm{d}}^{\max} = \gamma_{\mathrm{gb}} \left(\frac{\alpha}{D} - \frac{3f}{2r} \right). \tag{2.8}$$

Clearly, the boundary migration will cease when $F_{\mathrm{net}} = 0$. This occurs when

$$D_L = \frac{2\alpha r}{3f} . \tag{2.9}$$

In the above, D_L is the limiting grain size at which the growth process stops. Eq. (2.9) is often called the *Zener relationship* [1]. One can also derive a kinetic growth law for the grain size using the same approach conducted to arrive at Eq. (2.4). One now, however, has to use the net driving force given by Eq. (2.8). This gives rise to the logarithmic growth law [36],

$$D_L \left(D_\circ - D(t) \right) + D_L^2 \ln \left(\frac{\left(D_L - D_\circ \right)}{\left(D_L - D(t) \right)} \right) = k t . \tag{2.10}$$

Computational techniques such as Monte Carlo [42, 43] and phase field [44, 45] methods were used to study the pining effect of second-phase particles on grain growth.

These models refined the Zener's model by relaxing some of its assumptions. However the basic trends as captured by Zener relationship were unchanged.

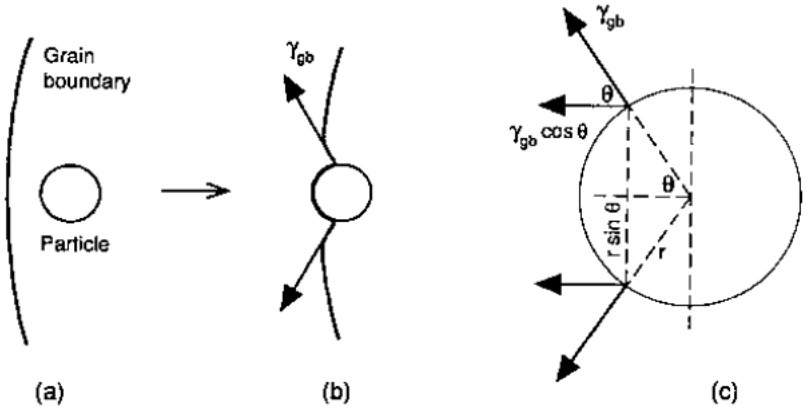

Figure 2.3. A schematic illustration of the particle-grain boundary interaction. (a) The immobile particle is approached by the migrating boundary. (b) The migrating boundary picks up the particle. (c) Detailed geometry of the interaction [1].

2.1.2.2 Grain Growth in Porous Solids

The effect of mobile particles such as pores on the kinetics of grain growth is more complicated. The pores can easily be dragged along by the moving grain boundary [1, 46-58]. This is attributed to the fact that the moving boundary applies a force on the pore causing the pore to change its shape. The leading surface of the pore becomes less curved than the trailing surface, which drives matter flux from the leading surface to the trailing surface (or vacancy flux in the opposite direction). This causes the pore to move forward in the direction of boundary migration. Such scenario is illustrated schematically in Figure 2.4. Matter transport from the leading surface of the pore to the trailing surface can proceed by three distinct mechanisms: vapor transport (evaporation and condensation), surface diffusion, and lattice (volume) diffusion. These mechanisms are also shown in Figure 2.4.

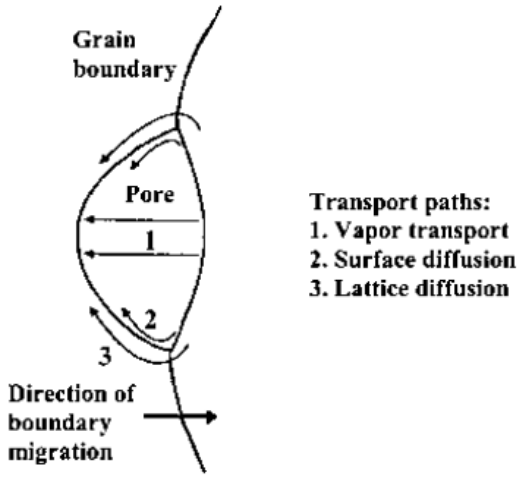

Figure 2.4. Different transport paths for a pore moving with a grain boundary. The mass transport is triggered by the curvature (chemical potential) difference between the leading surface of the pore and the trailing surface [1].

2.1.2.2.1 Classical Homogeneous Models

The first models to investigate the effect of pores on grain growth were proposed by Nichols [46], Brook [47], and carpay [48]. In these simplified models, the microstructure is assumed to be homogeneous. Hence, only one pore-boundary complex is used to represent the behavior of the whole system. Moreover, these models assume the grain and pore to be spherical for the sake of simplicity. Furthermore, these models neglect the pore coalescence and assume the pore moves as a rigid body without changing shape.

According to these models, there are two different scenarios for the interaction between the pore and the boundary. In one case, the migrating boundary could separate from the pore. In the other, the migrating boundary could drag the pore along with it. If the boundary separates from the pore, the boundary moves with its intrinsic velocity as in

the pore-free case. However, the separated pore can be picked up by another moving boundary but such situation is ignored in the classical models.

Pore breakaway will simply occur whenever the grain boundary velocity, v_b exceeds the pore velocity, v_p. This condition can be expressed as [1, 46-58],

$$M_{\mathrm{p}}F_{\mathrm{p}} < M_{\mathrm{b}}(F_{\mathrm{b}} - N_{\mathrm{p}}F_{\mathrm{p}}). \tag{2.11}$$

In the above, the subscript b denotes the boundary and p the pore; *M* is the mobility and *F* the driving force. $F_{\mathrm{b}} = \alpha\gamma_{\mathrm{gb}} / D$ is the driving force on the pore-free boundary due to its curvature. N_{p} is the average number of pores per grain boundary area. $F_{\mathrm{p}} = \pi r\gamma_{\mathrm{gb}}$ is the maximum drag force a pore can exert on a boundary (recall Eq. (2.5)). Hence the term $N_{\mathrm{p}}F_{\mathrm{p}}$ represents the drag force experienced by the boundary due to the presence of pores. Rearranging Eq. (2.11), the pore separation (breakaway) condition is expressed as,

$$F_{\mathrm{b}} > N_{\mathrm{p}}F_{\mathrm{p}} + \frac{M_{\mathrm{p}}F_{\mathrm{p}}}{M_{\mathrm{b}}}. \tag{2.12}$$

Now if one assumes that pore is nearly spherical and moves by surface diffusion, the pore mobility takes on the form [1, 46-52],

$$M_p = \frac{D_{\mathrm{s}} w \upsilon_{\mathrm{m}}}{\pi RT\, r^4}, \tag{2.13}$$

where, D_{s} is the surface diffusion coefficient, w is the thickness of the surface diffusion layer, υ_{m} is the molar volume, R is the universal gas constant, T is the absolute temperature, and r is the pore radius. Substituting Eq. (2.13) in Eq. (2.12) and assuming $N_{\mathrm{p}} \approx 1/D^2$ gives,

$$\left(\frac{D_s w \upsilon_{\mathrm{m}}}{M_{\mathrm{b}} R T r^3}\right) D_{\mathrm{sep}}^2 - D_{\mathrm{sep}} + \pi r = 0 \tag{2.14}$$

Here, D_{sep} is the grain size at which pore separation occurs.

On the other hand, if the pore moves along with the boundary, the velocity of the pore-boundary complex (v) can be obtained, by rearranging Eq. (2.11) and noting that $F_{\mathrm{p}} = v / M_{\mathrm{p}}$, as [1, 46-58]

$$v = M^{\mathrm{eff}} F_{\mathrm{b}}, \tag{2.15a}$$

$$M^{\mathrm{eff}} = \frac{M_{\mathrm{p}} M_{\mathrm{b}}}{M_{\mathrm{p}} + N_{\mathrm{p}} M_{\mathrm{b}}}. \tag{2.15b}$$

In the above, M^{eff} is the effective mobility of the pore-boundary complex. Two limiting cases are immediately obtained from Eq. (2.15). When $M_{\mathrm{p}} \gg N_{\mathrm{p}} M_{\mathrm{b}}$, the effective velocity of the pore-boundary complex reduces to $v = M_{\mathrm{b}} F_{\mathrm{b}}$, hence the effect of pores on the boundary velocity is negligible, a case which is commonly referred to as *boundary-controlled* grain growth. Note that this condition could mean high pore mobility, small pore fraction, low boundary mobility, or any combination of these criteria. The other limiting case is when $M_p \ll N_p M_b$. In this case, the velocity of the pore-boundary complex becomes $v = M_p F_b / N_p$, and hence the boundary velocity is limited by the pore mobility. This case is referred to as *pore-controlled* grain growth. The velocity of the pore-boundary complex can also take on intermediate values between these two extremes.

For the boundary-controlled case, one should expect the same parabolic grain growth kinetics derived for the pore-free system (see Eq. (2.4)). However, for the pore-controlled

case, a few growth laws for the average grain size were derived [1, 46-58]. For example, for pore migration by surface diffusion, the boundary velocity is given by

$$v_{\mathrm{b}} \approx \frac{dD}{dt} = M_{\mathrm{p}} F_{\mathrm{b}} / N_{\mathrm{p}} = \frac{D_{\mathrm{s}} w \upsilon_{\mathrm{m}}}{\pi R T r^4} \frac{F_{\mathrm{b}}}{N_{\mathrm{p}}}. \tag{2.16}$$

Taking $F_{\mathrm{b}} \approx \gamma_{\mathrm{gb}} / D$, $N_{\mathrm{p}} \approx 1/D^2$, and $r \approx D$, Eq. (2.16) can be rewritten as,

$$\frac{dD}{dt} = \frac{k}{D^3}, \tag{2.17}$$

where k is a constant at a particular temperature. Direct integration then gives,

$$D^4 - D_{\circ}^4 = k't. \tag{2.18}$$

Other growth equations were derived by the same procedure for other mechanisms [1]. In general, the growth law is a power law that has the form,

$$D^n(t) - D_{\circ}^n = k\,t. \tag{2.19}$$

The value of the growth exponent, n, is dictated by the prevailing mechanism for pore migration. For pore migration via evaporation and condensation, $n = 2$; while for pore migration by lattice (volume) diffusion, $n = 3$.

In the classical homogeneous models summarized above, it was assumed that the microstructure is homogeneous, the pores have nearly spherical shape, and the pore shape does not change during the interaction with the migrating boundary. These assumptions are unrealistic and hence limit the applicability of these models. In fact, many experimental results of grain growth in porous solids showed that these models cannot provide quantitative predictions and are only able to give a qualitative picture of the

process [36-40]. This motivated the community to develop more advanced models that relax these assumptions. Spatiotemporal models [49-58] were then developed to take into account the detailed geometries of the pore and the grain boundary, and hence the heterogeneity of the microstructure.

2.1.2.2.2 Sharp-Interface Models

The sharp-interface models were the first spatiotemporal models to be developed for investigating grain growth in porous solids [49-53]. These models treat the interfaces between different phases as singular surfaces [59-63]. Therefore, appropriate boundary conditions must be applied at the interface, and hence the interface position must be tracked all the time. Such types of problems are known as free (moving) boundary problems.

Evans and co-workers [49, 50], and Riedel and Svoboda later [51, 52] formulated the sharp-interface description of the problem. In that description, the grain boundary moves by mean curvature while the pore migrates via surface diffusion. Surface diffusion is expected to be the dominant mechanism of pore migration in solids at temperatures of interest [1, 47-58]. Moreover, the shrinkage of pores is ignored and hence the pores have a prescribed constant volume.

The mathematical formulation of the sharp-interface dynamics of the co-evolution of pores and grain boundary can be summarized as follows. The grain boundary moves under the influence of its curvature according to the relation,

$$v_b = -\gamma_{\mathrm{gb}} M_b \kappa_b \,. \tag{2.20}$$

Here, v_b is the velocity of a grain boundary element, γ_{gb} is the grain boundary energy, M_b is the grain boundary mobility, and κ_b is the grain boundary local curvature (mean curvature in 3D). The curvature is positive for convex surfaces and negative for concave surfaces.

On the other hand, the pore moves via surface diffusion as

$$v_p = -w\upsilon_m \nabla_s \cdot J_s , \tag{2.21}$$

where, v_p is the velocity of an element of the pore (free) surface, w is the thickness of the surface diffusion layer, υ_m is the molar volume, ∇_s is the surface gradient operator (i.e., it is a two-dimensional gradient operator in the surface tangent plane), and J_s is the surface flux. The surface flux is related to the gradient of the excess chemical potential along the surface, e.g.,

$$J_s = -\frac{D_s}{RT}\nabla_s \delta\mu . \tag{2.22}$$

D_s is the surface diffusion coefficient, R is the universal gas constant, T is the absolute temperature, and $\delta\mu$ is the excess chemical potential at a curved surface. The excess chemical potential of a curved surface relative to a flat surface is given by the well-known Gibbs-Thompson condition [61-66], e.g.,

$$\delta\mu = \gamma_s \kappa_s , \tag{2.23}$$

where, γ_s is the pore (free) surface energy, and κ_s is the local curvature of the pore (free) surface. By substitution of Eq. (2.22) and Eq. (2.23) into Eq. (2.21) and assuming isotropic surface energy and diffusion coefficient, one obtains

$$v_p = \frac{\gamma_s D_s w\upsilon_m}{RT}\nabla_s^2 \kappa_s . \tag{2.24}$$

In Eq. (2.24), ∇_s^2 is the surface Laplacian operator (e.g., the two-dimensional Laplace operator on the surface). Eq. (2.24) was first derived by Mullins [65]. The type of motion given by Eq. (2.24) is commonly referred to as motion by the Laplacian of mean curvature [66]. Therefore, the dynamical system of the co-evolution of pores and grain boundaries combines motion by mean curvature (Eq. (2.20)) with motion by the Laplacian of mean curvature (Eq. (2.24)).

By solving Eq. (2.20) and Eq. (2.24) simultaneously, the co-evolution of pores and grain boundaries in a porous polycrystalline solid can be tracked. In order to solve these equations, boundary conditions at the pore tip must be supplemented. The appropriate boundary conditions are the continuity of the chemical potential and surface flux. From Eq. (2.22) and Eq. (2.23), this translates into the continuity of κ_s and $\nabla\kappa_s$ at the pore tip. Moreover, mechanical equilibrium requires that the tension forces to be balanced at the pore tip. This means that the equilibrium dihedral angle, Ψ defined by $\Psi = 2\cos^{-1}(\gamma_{gb} / 2\gamma_s)$ must be maintained during the evolution. A schematic illustration of the dihedral angle at the pore tip is shown in Figure (2.5).

Evans and co-workers only obtained a steady-state solution for an idealized (axisymmetric) 2D geometry of an edge pore (a pore on a two-grain junction) [49, 50]. Later, Riedel and Svoboda extended the analysis to other higher-order pore configurations (e.g., pores on three- and four-grain junctions) and non-steady-state motion [51, 52]. However, only idealized 2D geometries of the pore and grains were considered so that the boundary conditions can easily be applied. Nevertheless, the solution of these simplified configurations improved our understanding of the problem. It

was demonstrated that the possibility of pore breakaway depends on the pore configuration. Edge pores can directly separate from a migrating boundary while higher-order pores usually transform to edge pores (partial separation) before complete separation. Moreover, it was also shown that the rate constant (or equivalently the activation energy) is a function of the pore fraction for both boundary- and pore-controlled kinetics. Therefore, quantitative analysis of grain growth in porous solids requires a detailed description of the amount and distribution of porosity.

As mentioned above, for three decades only 2D simulations of the sharp-interface model were conducted. Barrett et al. [67] have recently presented the first 3D solution of coupled surface and grain boundary motion. However, they have only considered simple test cases to validate their finite-element algorithm and numerical scheme. Large scale 3D simulations of the sharp-interface model of grain growth are yet to be performed probably because of numerical difficulties. Therefore, the development of a phase field (diffuse-interface) description of the problem is highly desirable since it is well-known that such models can handle complex microstructures in a straightforward manner [59-62]. This has motivated us to tackle the problem using the phase field approach as explained in the next chapter. However, before we introduce the phase field model, we first review the basic ingredient of the phase field (diffuse-interface) approach.

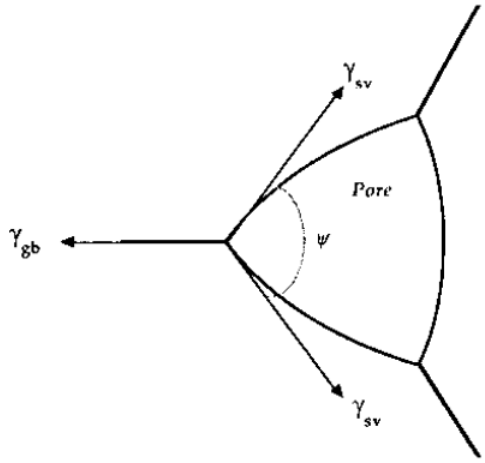

Figure 2.5. The equilibrium dihedral angle at the pore tip [1].

2.2 Phase Field Modeling of Microstructure Evolution in Materials

Phase field modeling has been widely used in predicting microstructural evolution in materials [59-62]. The main feature of this approach is the treatment of the interfaces between phases as diffuse. The material properties of interest, which are represented by phase fields or order parameters, are assumed to change rapidly but smoothly across the interfaces. This is captured schematically in Figure 2.6. The position of the interface is implicitly given by a constant phase field level, which obviates the necessity of explicitly tracking the interface. Based on this powerful concept, phase field methods enabled the simulation of complex evolution problems such as the solidification [68], solid-state transformations [69], grain growth [70, 71], crack propagation [72], dislocation dynamics [73], sintering [74-76], electromigration [77, 78], vesicle membranes [79], and void growth in irradiated materials [62]. Historical developments of the diffuse interface concepts can be traced back to the works of Van der Waals on gas condensation [80],

Landau on phase transitions [81] (where the concept of order parameter or phase field was first introduced), Landau and Ginzburg on superconducting states [82], and Cahn and Hilliard on the thermodynamics of heterogeneous systems [83-85]. In all of these and in subsequent works, order parameters may represent conserved quantities such as mass and energy density or non-conserved quantities such as polarization, long-range order and grain orientation.

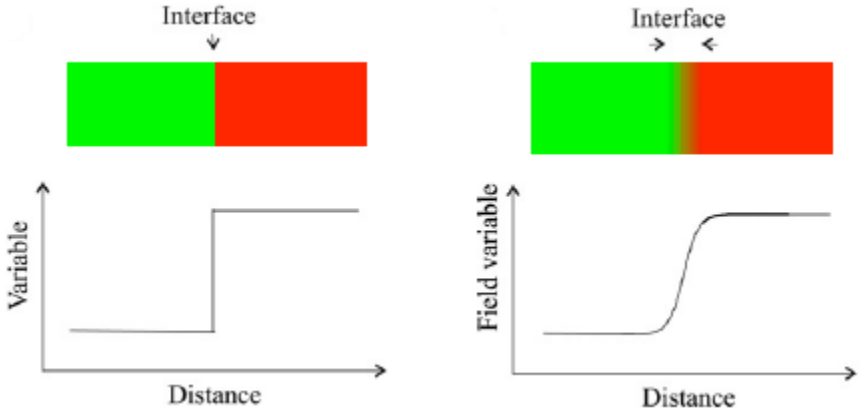

Figure 2.6. Sharp-interface versus diffuse-interface descriptions of interfaces in heterogeneous materials. In the sharp-interface description, the order parameter (the material property of interest) changes sharply across the interface; hence the interface is a singular surface that must be tracked during the evolution of the system (e.g., a moving boundary problem). In the diffuse-interface description, the order parameter (phase field) changes rapidly but smoothly across the interface. The interface position is then implicitly given by the gradients of the order parameters, and hence explicit tracking of the interface is no longer required [90].

A typical procedure for constructing a phase field model is as follows. First, the free energy of the heterogeneous system is expressed in the Ginzburg-Landau (or Cahn-Hilliard) functional form in terms of the order parameter as [81-83],

$$F = \int [f(\phi(r)) + \frac{\kappa_\phi}{2} |\nabla \phi(r)|^2] \, d^3 r \, . \tag{2.25}$$

In the above, ϕ is the order parameter of interest and $f(\phi)$ is the bulk (local/homogeneous) chemical (short-range) free energy density. Contributions of long-

range interactions such as elastic or electrostatic energies to the free energy of the system can easily be added to the Ginzburg-Landau (Cahn-Hilliard) free energy functional thanks to its varitional formulation [59-62, 86-90]. The gradient term represent the excess free energy due to the heterogeneous nature of the system, i.e., presence of interfaces. The gradient coefficient κ_ϕ is a material constant that is usually related to the specific energy of the interface (e.g., surface energy, grain boundary energy, etc.)

The second step is to derive a kinetic evolution equation for the order parameter. This is usually carried out by invoking the principles of irreversible thermodynamics [59-61, 86-95]. Following that approach, the order parameter evolves in such a way that the free energy of the system decreases monotonically while the entropy production is non-negative. However, depending on whether the order parameter is a conserved or non-conserved quantity, additional constraints may apply. This usually leads to three different categories of phase field models. In analogy to the stochastic models of dynamic critical phenomena [96], phase field models are often classified into three types: models of type A, B and C. Models of type A describe systems with non-conserved order parameters. Models of type B describe systems with conserved order parameters. Models of type C describe systems with both conserved and non-conserved order parameters. These models can be considered as the continuum (macroscopic/coarse-grained) description of the discrete (microscopic) kinetic Ising models developed in the condensed-matter physics literature [97, 98].

Phase field model A is used to describe the evolution of systems where conservation principles are not required to hold locally such as in diffusionless phase transformations. This is the continuum analog of the spin-flip Glauber kinetics model [97]. It has been

successfully applied for investigating martensitic transformations, order/disorder transition and antiphase/grain boundary motion in magnetic domain walls/polycrystalline solids [59-62, 86-90]. The non-conserved order parameter in this model evolves according to the time-dependent Ginzburg-Landau (or Allen-Cahn) equation [99], which has the form

$$\frac{\partial \phi}{\partial t} = -L\frac{\delta F}{\delta \phi} = -L\left[\frac{df(\phi)}{d\phi} - \kappa_\phi \nabla^2 \phi\right]. \tag{2.26}$$

Here $\delta F / \delta \phi$ is the functional derivative of the free energy functional (see Eq. (2.25)] with respect to the order parameter and L is a mobility.

Phase field model B is usually utilized when local conservation principles must be followed. This is the case for example in diffusion-controlled particle growth and coarsening (e.g., precipitation, solidification, etc.). This is the continuum analog of the spin-exchange Kawaski kinetics model [98]. It has been used to study spinodal decomposition, precipitation, Ostwald ripening, and void growth in irradiated solids [59-62, 100-106]. The conserved order parameter evolves according to Cahn-Hilliard equation [100], which takes on the form

$$\frac{\partial \phi}{\partial t} = \nabla \cdot M(\phi)\nabla\frac{\delta F}{\delta \phi} = \nabla \cdot M(\phi)\nabla\left[\frac{df(\phi)}{d\phi} - \kappa_\phi \nabla^2 \phi\right]. \tag{2.27}$$

$M(\phi)$ is a mobility that, in general, may depend on the order parameter. In this description, the functional derivative of the free energy functional with respect to the conserved order parameter, $\delta F / \delta \phi$, is considered as a generalized (non-classical/non-local) chemical potential. Hence, the Cahn-Hilliard equation is simply a continuity equation for the conserved order parameter.

Phase field model C has been introduced to investigate the evolution of systems with coupled conserved and non-conserved order parameters. It has been successfully utilized in investigating concurrent phase separation and order/disorder transition in alloys, sintering in polycrystalline solids, solute drag effect on solidification, second-phase/solute drag effect on grain growth [59-62, 107-112]. The most general and thermodynamically-consistent version of the model is the one suggested by Bi and Sekerka [91]. In this version, the free energy functional of the system is expressed as,

$$F = \int [\, f\left(c(r), \eta(r)\right) + \frac{\kappa_c}{2} |\nabla c(r)|^2 + \frac{\kappa_\eta}{2} |\nabla \eta(r)|^2]\, d^3 r \,. \tag{2.28}$$

In the above equation, c is the conserved order parameter and η is the non-conserved order parameter. The evolution of the system is then described by coupled Cahn-Hilliard and Allen-Cahn equations;

$$\frac{\partial \eta}{\partial t} = -L \frac{\delta F}{\delta \eta} = -L \left[\frac{\partial f(c,\eta)}{\partial \eta} - \kappa_\eta \nabla^2 \eta \right], \tag{2.29a}$$

$$\frac{\partial c}{\partial t} = \nabla \cdot M(c) \nabla \frac{\delta F}{\delta c} = \nabla \cdot M(c) \nabla \left[\frac{\partial f(c,\eta)}{\partial c} - \kappa_c \nabla^2 c \right]. \tag{2.29b}$$

Again, when needed, long-range interactions, production, reaction, and advection terms can be incorporated into this general formalism in a straightforward manner [59-62].

When interfaces are inherently diffuse, such as with magnetic domain walls and in ordered-disordered systems, phase field formulations offer a natural mathematical description of the physical or chemical phenomenon. In such situations, the sharp-interface descriptions, if desired for any reason, must be constrained to capture the physics of the diffuse interfaces. On the other hand, the sharp interface approach is the natural formalism to describe interfaces that are atomically sharp such as free surfaces,

void or bubble surface in irradiated solids, or grain boundaries. Diffuse interface formalisms of the latter situations must be consistent with the corresponding sharp interface models. This consistency can be ensured by requiring the kinetic equations of the phase field models to reduce to their sharp interface counterparts when the diffuse-interface width approaches zero. This is usually accomplished by using a formal asymptotic analysis based on singular perturbation theory [59-61, 113-119]. Typical of such analysis is the expansion of phase fields in terms of a small parameter, which represents the diffuse-interface width, far from the interface (outer expansion) and within the interface (inner expansion). This is schematically depicted in Figure 2.7. Matching conditions are then applied to guarantee a smooth transition between the outer solution and the inner solution. The matching also provides the equation of motion of the interface, which is to be compared with its sharp-interface counterpart.

Lastly, tracking the microstructure evolution via phase field methods reduces to the problem of obtaining solutions for the Cahn-Hilliard and/or Allen-Cahn equations. Since these equations are nonlinear partial differential equations, numerical techniques are often employed for solving theses equations. The most common numerical techniques used for this purpose are finite difference method, Fourier-spectral method, and finite element method [59-61]. A few open source packages designed for solving the phase field equations have been recently developed [120-123]. These packages have usually the form of libraries written in object oriented C++ with modular structure to allow for easy code reuse and extension.

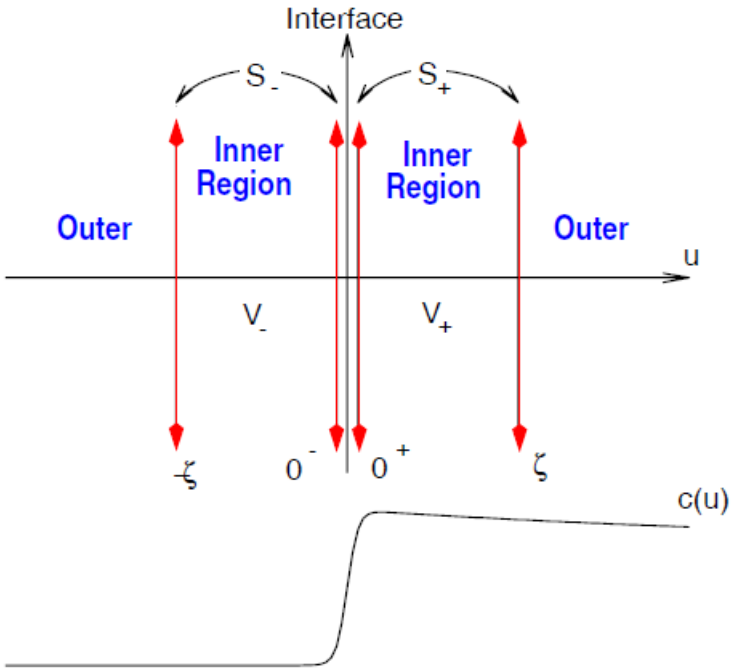

Figure 2.7. A schematic illustration of the inner and outer regions used in the asymptotic analyses of the phase field models. In the outer region, the gradients of the phase fields (order parameters) are small and can be ignored from the perturbative expansion. In the inner region, the gradients are high and must be taken into consideration. Matching the inner and outer expansions gives the complete and smooth profile of the order parameter across the interface and the equation of motion of the interface [59].

CHAPTER 3. PHASE FIELD MODEL DEVELOPMENT

The details of the development of the phase field model for grain growth in porous polycrystalline solids are discussed in this chapter. First, the phase fields (order parameters) that describe the microstructure of a porous polycrystalline solid are introduced in conjunction with their evolution equations, which were derived following the standard procedure that was highlighted in the previous chapter. Then a systematic procedure for determining the model parameters is addressed. Lastly, the numerical implementation of the phase field model is presented.

3.1 Phase Field Modeling of Grain Growth in Porous Polycrystalline Solids

While phase field models for sintering [74-76], ideal grain growth [70, 71], and the effect of solute segregation and immobile second-phase particles on the kinetics of grain growth exist in the literature [124-127], a phase field model of the effect of porosity on grain growth was lacking. This has motivated us to develop a phase field model for grain growth in porous solids [56-58]. As mentioned earlier, the grain growth in porous solids proceeds by two main mechanisms, the curvature-driven motion of grain boundaries and mass transport by diffusion along the pore surface. Pores migrate via surface diffusion, evaporation and condensation or lattice diffusion. Here, in common with previous investigations via classical and sharp-interface models [46-53], surface diffusion is assumed to be the sole mechanism of pore migration. The phase field model must thus be

constructed to couple these different types of motions in order to capture correctly the microstructure evolution and obtain accurately the kinetics of grain growth in porous solids [56-58].

The model can be summarized as follows. A combination of conserved and non-conserved order parameters (phase fields) is used to fully represent the microstructure of a porous polycrystalline solid [56-58]. The conserved field, $\rho(x,t)$, represents the fractional density of the solid, and it takes the value of 1 in the solid phase and 0 in the pore phase. It can also be considered as the complement of vacancy concentration, e.g., $\rho = 1 - c$, with c being the vacancy concentration. In order to distinguish between different grains with different orientations in the solid phase, a set of non-conserved order parameters, η_α, are used, where $\alpha = 1,2,....p$, with p being the total number of grains with different orientations in the solid. $\eta_\alpha = 1$ in the α-th grain and 0 otherwise. A schematic illustration for the phase field variables is shown in Figure 3.1. Tracking the evolution of these fields completely reveals the microstructure evolution in the porous polycrystalline solid [56-58].

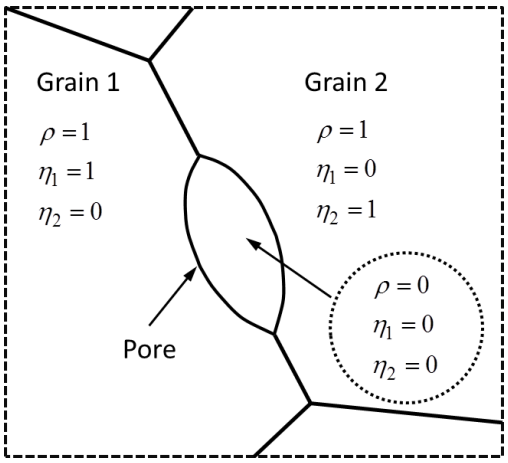

Figure 3.1. A schematic of the order parameters for the case of an edge pore between two grains [57].

In order to track the evolution of the phase fields, kinetic equations for the phase fields must be derived. As mentioned in the previous chapter, this can be accomplished by following the standard approach of irreversible thermodynamics. In this approach, the order parameters evolve such that the free energy monotonically decreases.

The free energy of the heterogeneous system of pores and grains can be constructed by invoking the formulation of Cahn and Hilliard for the free energy of non-uniform media [83]. The specific form used here is

$$F = \int [f(\rho, \eta_1, \eta_2, ..., \eta_\alpha) + \frac{\kappa_\rho}{2} |\nabla \rho|^2 + \frac{\kappa_\eta}{2} \sum_{\alpha=1}^{p} |\nabla \eta_\alpha|^2] \, d^3 r \, . \tag{3.1}$$

In the above expression, the first term represents the bulk free energy density. The two gradient terms account for the excess free energy due to pore (free) surfaces and grain boundaries, respectively. Using constant gradient coefficients is equivalent to the assumption of isotropic surface and grain boundary energies. The bulk free energy density used here is simply a positive-definite multi-well potential that represents the equilibrium phases. It has the form [56-58, 74],

$$f(\rho, \eta_1, \eta_2, ..., \eta_\alpha) = B\rho^2 (1-\rho)^2 + C[\rho^2 + 6(1-\rho)\sum_\alpha \eta_\alpha^2 - 4(2-\rho)\sum_\alpha \eta_\alpha^3 + 3(\sum_\alpha \eta_\alpha^2)^2] \tag{3.2}$$

This particular from has (p+1) minima that correspond to the pore phase and all grains in the solid phase. B, C, κ_ρ and κ_η are material constants related to surface and grain boundary energies. These relations can be derived from the equilibrium profiles of the order parameters across flat interfaces as in the pioneering work by Cahn and Hilliard [83]. The details of such derivation are given in Appendix A.

The conserved density field evolves according to a Cahn-Hilliard equation [100] in the form,

$$\frac{\partial \rho}{\partial t} = \nabla \cdot \mathbf{M} \nabla \mu = \nabla \cdot \mathbf{M} \nabla \frac{\delta F}{\delta \rho} = \nabla \cdot \mathbf{M} \nabla \left[\frac{\partial f(\rho, \eta_1, ..., \eta_\alpha, ..., \eta_p)}{\partial \rho} - \kappa_\rho \nabla^2 \rho \right]. \tag{3.3}$$

In the above equation, μ is a non-classical (non-local) chemical potential, $\delta F / \delta \rho$ is the functional derivative of the free energy with respect to the density field, and $\mathbf{M}$ is the Cahn-Hilliard (chemical) mobility tensor. In general, Cahn-Hilliard equation can represent different diffusion mechanisms, e.g., bulk, grain boundary, and surface [56]. However, we limit our study here to surface diffusion .The expression for the Cahn-Hilliard mobility tensor $\mathbf{M}$ has the form

$$\mathbf{M} = M_s \rho^2 (1-\rho)^2 \mathbf{T}_s \tag{3.4}$$

where M_s is a constant that is related to the surface diffusivity as shown via the asymptotic matching with the sharp-interface model in Appendix B, and $\mathbf{T}_s$ is a surface projection tensor, which guarantees that the surface diffusion is tangential to the surface [56-58, 118]. $\mathbf{T}_s$ has the form

$$\mathbf{T}_s = \mathbf{I} - \mathbf{n}_s \otimes \mathbf{n}_s , \tag{3.5}$$

with $\mathbf{I}$ being the identity tensor, $\otimes$ the dyadic product, and $\mathbf{n}_s$ the unit normal to the pore (free) surface. The latter is given by $\mathbf{n}_s = \nabla \rho / |\nabla \rho|$.

The non-conserved order parameters are governed by a set of Allen-Cahn equations [99]:

$$\frac{\partial \eta_\alpha}{\partial t} = -L \frac{\delta F}{\delta \eta_\alpha} = -L \left[\frac{\partial f(\rho, \eta_1, ..., \eta_\alpha, ..., \eta_p)}{\partial \eta_\alpha} - \kappa_\eta \nabla^2 \eta_\alpha \right] \quad \forall \alpha, \alpha = 1, 2....p . \tag{3.6}$$

Here, L (the Allen-Cahn mobility) is a material property that is directly related to the grain boundary mobility as shown via the asymptotic matching with the sharp-interface model in Appendix B. By using a constant Allen-Cahn mobility, we assume isotropic grain boundary mobility.

The resulting coupled Cahn-Hilliard and Allen-Cahn dynamical system is able to couple the curvature-driven motion of the grain boundary with the pore motion by surface diffusion. Using the method of matched asymptotic expansions, the fact that the proposed phase field model recovers the corresponding sharp-interface model (recall Eq. (2.20) and Eq. (2.24)) is demonstrated in details in Appendix B. Therefore, solving the set of kinetic equations (3.3) and (3.6) reveals the microstructure evolution in a porous polycrystalline solid, and hence the kinetics of grain growth in such materials can be investigated.

3.2 Determination of Model Parameters

There are two types of parameters in the phase field model, e.g., energetic and kinetic parameters. The energetic parameters that appear in the free energy expressions (see Eq. (3.1) and Eq. (3.2)) can be shown to be directly related to thermodynamic properties such as surface and grain boundary energies. Such relations could be established by investigating the equilibrium solutions of phase field variables across flat interfaces as was pioneered by Cahn and Hilliard [83]. The details of this derivation are given in Appendix A. Here, we only summarize the final results. The free energy parameters are related to the surface and grain boundary energy as:

$$B = \frac{12\gamma_{\mathrm{s}} - 7\gamma_{\mathrm{gb}}}{\ell}, \tag{3.7a}$$

$$C = \frac{\gamma_{\mathrm{gb}}}{\ell}\ , \tag{3.7b}$$

$$\kappa_\eta = \frac{3}{4}\gamma_{\mathrm{gb}}\,\ell\ , \tag{3.7c}$$

$$\kappa_\rho = \frac{3}{4}\ell(2\gamma_{\mathrm{s}} - \gamma_{\mathrm{gb}})\ . \tag{3.7d}$$

In the above, ℓ is the diffuse interface width, which, to be consistent with the sharp-interface description of the problem, is on the order of a surface layer/grain boundary thickness.

The kinetics parameters that appear in Cahn-Hilliard (Eq. (3.3)) and Allen-Cahn (Eq. (3.6)) equations are directly related to the surface diffusivity and grain boundary mobility (recall the sharp-interface model, e.g., Eq. (2.20) and Eq. (2.24). This connection can be demonstrated using the asymptotic matching between the diffuse- and sharp-interface models. While the primary goal of the asymptotic analysis is to prove that the phase field (diffuse-interface) model recovers its sharp-interface counterpart, it also provides a clear connection between the parameters of the two models. Such relations are crucial for the phase field model to be quantitative [56-62]. The details of the asymptotic analysis are given in Appendix B. Here, we only quote the final results. According to the asymptotic analysis of the phase field model, the equations of motions for the grain boundary and the pore surface are given by,

$$v_{\mathrm{b}} = -L\,\kappa_\eta\,\kappa_{\mathrm{b}}\,, \tag{3.8a}$$

$$v_{\mathrm{p}} = M_{\mathrm{s}}(\kappa_\eta + \kappa_\rho)\nabla_{\mathrm{s}}^2\kappa_{\mathrm{s}}\ . \tag{3.8b}$$

In the above, the parameters have the same definitions as appeared before (recall Eq. (2.20), Eq. (2.24), Eq. (3.1), Eq. (3.3), and Eq. (3.6)). By comparing the relations of Eq.

(3.8) with their sharp-interface counterparts, e.g., Eq. (2.20) and Eq. (2.24), the Allen-Cahn and Cahn-Hilliard mobilities can be related to the grain boundary mobility and surface diffusivity as follow;

$$L\kappa_\eta = \gamma_{\mathrm{gb}} M_b \,, \tag{3.9a}$$

$$M_{\mathrm{s}}(\kappa_\rho + \kappa_\eta) = \frac{\gamma_{\mathrm{s}} D_{\mathrm{s}} w \upsilon_{\mathrm{m}}}{RT} \,. \tag{3.9b}$$

The relations of Eq. (3.7) and Eq. (3.9) completely fix the phase field model parameters in terms of the physical material properties, which facilitates obtaining quantitative results that can be compared with experiments as will be shown in the next chapter.

3.3 Numerical implementation

3.3.1 Non-dimensionalization of Kinetic Equations

For the sake of convenience during the numerical implementation of the phase field model, a non-dimensional version of the kinetic equations (Eq. (3.3) and Eq. (3.6)) has been used. The non-dimensional form was obtained using a reference energy density, ε, reference length scale, ℓ^*, and reference time scale, t^*. We take $\varepsilon = B$ as a reference energy density, $\ell^* = \sqrt{4\kappa_\eta / 3C}$ as a reference length scale, and $t^* = 1/L\varepsilon$ as a reference time scale. Note that the non-dimensionalization is merely for simplifying the numerical implementation; the model parameters for a specific material can be directly calculated from Eq. (3.8) and Eq. (3.9). The normalized equations are thus given by,

$$\frac{\partial \rho}{\partial \tau} = \ell^* \nabla \cdot \left[\frac{M}{L\ell^{*2}} \ell^* \nabla \left(\frac{1}{\varepsilon} \frac{\delta F}{\delta \rho} \right) \right] = \tilde{\nabla} \cdot \left[\tilde{M} \tilde{\nabla} \left(\frac{\delta \tilde{F}}{\delta \rho} \right) \right] \tag{3.10a}$$

$$\frac{\partial \eta_\alpha}{\partial \tau} = -\left[\frac{1}{\varepsilon}\left(\frac{\delta F}{\delta \eta_\alpha}\right)\right] = -\left(\frac{\delta \tilde{F}}{\delta \eta_\alpha}\right) \tag{3.10b}$$

Here, $\tau = t/t^*$ is the non-dimensional time, $\tilde{\nabla} = \ell^* \nabla$ is the non-dimensional del operator and $\tilde{M} = M/L\ell^{*2}$ is the non-dimensional Cahn-Hilliard (chemical) mobility.

3.3.2 Explicit Finite-difference Scheme

In this scheme, the kinetic equations of the phase field model were discretized using a second-order centered finite difference approximation for all spatial derivatives and a first-order explicit Euler approximation for time derivatives [61, 90]. The Laplacian operator that appears in Eq. (3.3) and Eq. (3.6) was represented using the standard 5(7) point stencil for 2D (3D) solutions. For the sake of ensuring the numerical stability of the explicit scheme, one must satisfy the condition that $\tilde{M}\Delta t/(\Delta x)^4 \le (1/2)^{\mathrm{d}}$, where Δx is the mesh size, Δt is the time step, and d is the dimension of the problem. In all the simulations presented in this dissertation that were conducted via the explicit scheme, these parameters took on the values: $\Delta x = 1.0$, $\tilde{M} = 0.01 - 1.0$, $\Delta t = 0.01 - 0.08$. Moreover, for all the explicit scheme simulations presented here, a periodic boundary condition is considered and the interface includes 5 mesh points. The explicit scheme was implemented using in-house codes written in FORTRAN 90.

When applying the model for investigating the grain growth kinetics in polycrystalline solids, a Voronoi tessellation was utilized to generate the initial polycrystalline structure and each grain was assigned a different order parameter to avoid artificial coalescence of grains during the simulation. Due to the high computational cost associated with the large number of non-conserved order parameters, parallel computing

was used. Specifically, each simulation run was carried out on a single node that contains 48 cores using the shared-memory parallelization concept. All the explicit scheme simulations runs were performed on Hansen cluster at Purdue University. The typical computing time ranges from three to ten days for 2D simulations and from one week to one month for 3D simulations.

3.3.3 Fully-coupled, Fully-implicit Finite-element Scheme Using MARMOT

A more advanced numerical technique was then used to solve the phase field model equations. This technique is based on finite-element discretization of the phase field kinetic equations. The resulting nonlinear system of equations is then solved using the mesoscale simulator, MARMOT developed at Idaho National Laboratory [123].

MARMOT is a phase field framework for simulating microstructure evolution in materials. It is one of several applications based on the Multiphysics Object-Oriented Simulation Environment (MOOSE) developed at Idaho National Laboratory [121-123]. MOOSE is a massively parallel finite element framework suitable for solving multiphysics problems. MOOSE is a winner of the 2014 R&D 100 award. MOOSE currently meets all Nuclear Quality Assurance Level 1 (NQA-1) requirements. MOOSE is now open source software that can be downloaded freely from GitHub [121]. Its modular structure simplifies the development of user programs and maximizes code reuse.

The main structure of MOOSE is schematically depicted in Figure 3.2. As shown in the figure, MOOSE provides a high-level interface that utilizes libMesh, the finite-element library developed at the University of Texas at Austin [128] and the nonlinear solvers available via PETSc, the toolkit for scientific computation developed by Argonne

National Laboratory [129]. MOOSE has built-in time and mesh adaptivity, it is dimension agnostic and automatically parallel .

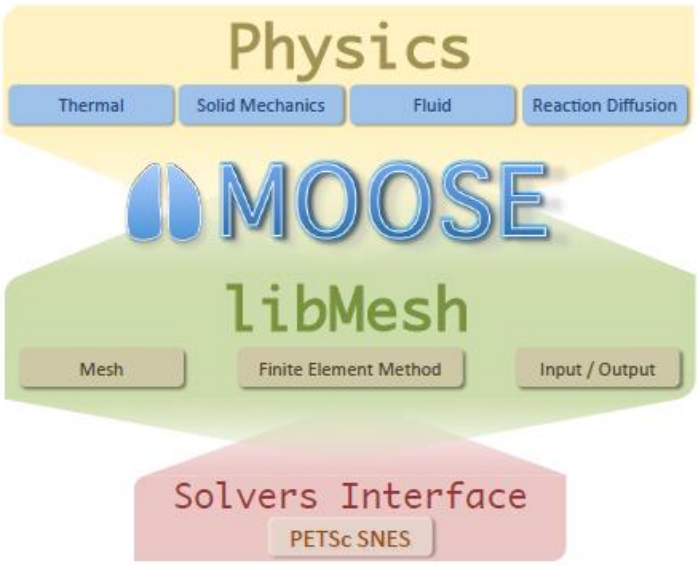

Figure 3.2. A schematic illustration of the structure of the Multiphysics Object-Oriented Simulation Environment (MOOSE) developed at Idaho National Laboratory [121].

As any MOOSE-based application, MARMOT inherits all the advantages and capabilities of MOOSE. It is designed particularly for solving all types of phase field models [123]. It takes advantage of the common structure of the phase field models (their usage of Cahn-Hilliard and Allen-Cahn equations) to provide general C++ base templates that can be modified to implement a specific model. Due to its object-oriented design, this can be accomplished in a straightforward manner [123].

The first step to implement the current model in MARMOT is to form the varitional (weak) form of the partial differential equations (PDEs) (see Eqs (3.3) and (3.6)) [130]. However, one should note that the Cahn-Hilliard equation (Eq. 3.6) is a fourth-order PDE

that requires C^1 continuous basis functions for discretization [123, 130, and 131]. Nonetheless, it can be split into two second-order equations which allows the use of regular C^0 continuous basis functions with linear elements [123, 131]. This can be achieved by using the chemical potential as an auxiliary variable [131]. This drastically decreases the computation time and introduce negligible error to the solution [131]. Moreover, when implementing the model in MARMOT, the vacancy concentration (c) is used instead of the fractional mass density as the conserved parameter. As, we mentioned earlier the two are simply related by $c = 1 - \rho$. Therefore, the kinetic equations of the model become

$$\mu = \frac{\partial f(c,\eta_1,....,\eta_\alpha,....,\eta_p)}{\partial c} - \kappa_c \nabla^2 c\,, \tag{3.11a}$$

$$\frac{\partial c}{\partial t} = \nabla \cdot \mathbf{M} \nabla \mu\,, \tag{3.11b}$$

$$\frac{\partial \eta_\alpha}{\partial t} = -L\frac{\delta F}{\delta \eta_\alpha} = -L\left[\frac{\partial f(c,\eta_1,....,\eta_\alpha,....,\eta_p)}{\partial \eta_\alpha} - \kappa_\eta \nabla^2 \eta_\alpha\right] \quad \forall \alpha,\ \alpha = 1,\ 2....p\,. \tag{3.11c}$$

In the above $\kappa_c \equiv \kappa_\rho$ and $f(c,\eta_1,....,\eta_\alpha,....,\eta_p) \equiv f(\rho,\eta_1,....,\eta_\alpha,....,\eta_p)$ with ρ replaced by $1-c$ in Eq. (3.2). The residual equations in the weak form are then

$$(\mu,\phi) - \left(\frac{\partial f}{\partial c},\phi\right) - (\kappa_c \nabla c, \nabla \phi) + < \kappa_c \nabla c \cdot \mathbf{n}, \phi > = 0\,, \tag{3.12a}$$

$$\left(\frac{\partial c}{\partial t},\phi\right) + (\mathbf{M}\nabla\mu, \nabla\phi) - < \mathbf{M}\nabla\mu \cdot \mathbf{n}, \phi > = 0\,, \tag{3.12b}$$

$$\left(\frac{\partial \eta_\alpha}{\partial t},\phi\right) + L\left(\frac{\partial f}{\partial \eta_\alpha},\phi\right) + L(\kappa_\eta \nabla \eta_\alpha, \nabla\phi) - L < \kappa_\eta \nabla \eta_\alpha \cdot \mathbf{n}, \phi > = 0 \quad \forall \alpha,\ \alpha = 1,\ 2....p\,. \tag{3.12c}$$

In the above ϕ is a test function, $(\cdot,\cdot)$ stands for interior integration, and $<\cdot,\cdot>$ for boundary integration. Linear Lagrange discretization of Eqs (3.12a-3.12c) employing four-node quadrilateral elements in 2D and eight-node hexahedral elements in 3D was performed. The time integration was carried out via a second-order Backward Differentiation Formula (BDF2).

The second step is to solve the nonlinear system. This goal was accomplished using the Jacobian-Free Newton Krylov (JFNK) method [132]. This is a quasi-Newton method where the linear system inside each nonlinear iteration is solved iteratively using a Krylov method. Since usually only the action of the Jacobian on a vector is need, the Jacobian itself is not required to be assembled; hence the name Jacobian-Free Newton Krylov method. Here the generalized minimal residual (GMRES) method is used for solving the linear system [133].

In investigating the grain growth in polycrystalline solids, a Voronoi tessellation was also used to generate the initial polycrystalline structure as in the explicit scheme. However, since the number of degrees of freedom (DOF) is linearly proportional to the number of the non-conserved order parameters representing the grains, simulations of ensembles with large number of grains are unfeasible. Nonetheless, there are some useful algorithms that were developed to remedy this issue [134-138]. Such algorithms use small number of order parameters to simulate large number of grains. This is accomplished by randomly assigning order parameters to grains and then switching these order parameters when two grain represented by the same order parameter are close to each other. MARMOT has its own switching algorithm that is called Grain Tracker. A representation of a polycrystalline structure using Grain Tracker is shown in Figure 3.3.

In this figure, 400 grains are represented using only 15 distinct order parameters (orientations). Nevertheless, the computational cost was still high and parallel computing was used. Specifically, 2D simulation runs were carried out using 72 cores and 3D simulations using 600 cores. All MARMOT simulations runs were performed on Fission cluster at Idaho National Laboratory. The typical computing time ranges from a day to three days for 2D simulations and from four days to one week for 3D simulations.

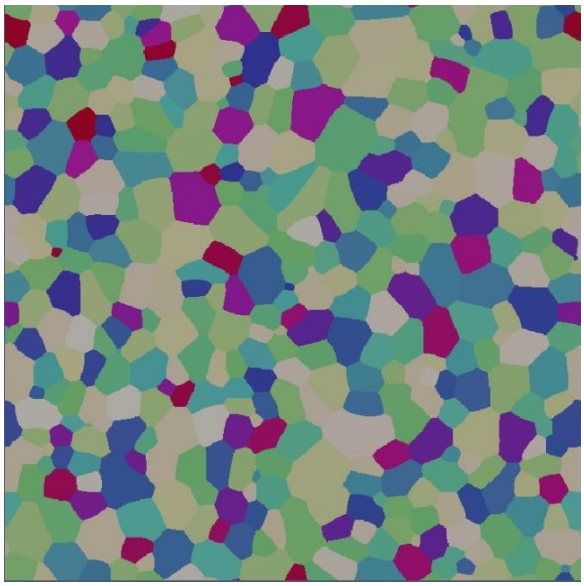

Figure 3.3. Representation of 400 grains with different orientations using only 15 non-conserved order parameters via Grain Tracker algorithm implemented in MARMOT. Different colors represent different orientations.

3.3.4 Increasing Length and Time Scales of the Phase Field Model

When solving the phase field kinetic equations, numerical stability requires few mesh points to be placed within the interfacial regions. Since the physical interface width is in nanometers (i.e., on the order of the thickness of a surface layer), the grid spacing would be limited to about 1 nanometer. In this case, mesoscale simulations (with grain sizes in

micrometers) will not be feasible. A remedy for this problem is to modify the phase field model parameters without altering the thermodynamic driving forces or the kinetics in accordance with equations (3.7 and 3.9). By increasing the gradient coefficients and at the same time decreasing the bulk free energy parameters, the diffuse interface increases while the surface and grain boundary energy remain the same. However, according to the equation of motions (e.g., Eq. 3.8), increasing the gradient coefficients must be accompanied by decreasing the Cahn-Hilliard and Allen-Cahn mobilities in order to keep the kinetics unaltered. This approach of increasing the length and time scales of the phase field models was utilized before [139-141].

CHAPTER 4. RESULTS AND DISCUSSION

The results obtained by solving the phase field model for grain growth in porous solids are presented and discussed in this chapter. In the first section, test cases that demonstrate the capabilities of the model are explained. These test cases also serve as a benchmark for the model before simulating real systems. In the second section, the pore drag effect on the kinetics of grain growth is examined thoroughly using idealized 2D configurations for the pore and grain. In the third section, 2D solutions of the model for grain growth in porous uranium dioxide are introduced. 3D simulations of grain growth in porous ceria are then presented. Lastly, 2D and 3D simulations of grain growth in porous polycrystalline solids using MARMOT are discussed. Some of the results presented here were published in [56-58].

4.1 Test Results

In this section, we examine the model by investigating simple test cases. For some of these cases, analytical solutions exist that can be used to evaluate quantitatively the model solutions. First, we examine the establishment of the equilibrium dihedral angle at the triple-junction and the equilibrium pore configuration. We then study the kinetics of the curvature-driven motion by simulating the shrinkage of an isolated circular grain embedded in a solid matrix. The surface diffusion kinetics is then investigated by simulating the flattening of a perturbed solid surface and the instability of cylindrical

particles. Lastly, the classical example of the sintering of two unequal-sized particles is discussed in details.

4.1.1 Equilibrium Dihedral Angle and Pore Configuration

As mentioned in Chapter 2, mechanical equilibrium requires the balance of surface and grain boundary tensions at the triple-junction (the junction between a grain boundary and two free surfaces). This condition is equivalent to requiring the establishment of an equilibrium dihedral angle defined as $\Psi = 2\cos^{-1}(\gamma_{gb} / 2\gamma_s)$ at the triple-junction. Clearly, different ratios of grain boundary to surface energy give rise to different equilibrium angles. This scenario can be tested using the phase field model by noting that different sets of free energy parameters produce different surface to grain boundary ratios (see Eq. (3.7))) and, hence, different values of the equilibrium dihedral angle, Ψ. For instances, if we set $B = C$ and $\kappa_\rho = \kappa_\eta / 3$, we obtain $\gamma_s = 2\gamma_{gb} / 3$ and $\Psi = 83^\circ$, while if we put $B = 5C$ and $\kappa_\rho = \kappa_\eta$, we obtain $\gamma_s = \gamma_{gb}$ and $\Psi = 120^\circ$. These results are demonstrated in Figure 4.1.

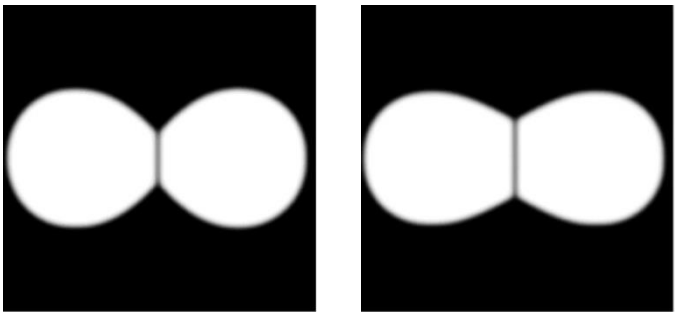

(a) (b)

Figure 4.1. The dependence of the equilibrium dihedral angle on the surface to grain boundary ratio. Two different ratios generated using two different sets of free energy parameters: (a) $B = C$ and $\kappa_\rho = \kappa_\eta / 3$ gives $\Psi = 83^\circ$, while (b) $B = 5C$ and $\kappa_\rho = \kappa_\eta$ gives $\Psi = 120^\circ$ [56].

The condition of mechanical equilibrium has also a direct implication on the equilibrium pore configuration in porous polycrystalline solids. Since the equilibrium dihedral angle must be established at the pore tip, the equilibrium pore shapes are different for pores on two-, three- or higher-order-grain junctions. In general, the equilibrium pore configuration depends on the dihedral angle and number of grains attached to the pore, the latter is commonly called the *pore coordination number* [1]. Different equilibrium pore configurations at different junctions are shown in Figure 4.2, which is a close-up view of a 2D porous polycrystalline structure that was simulated using MARMOT.

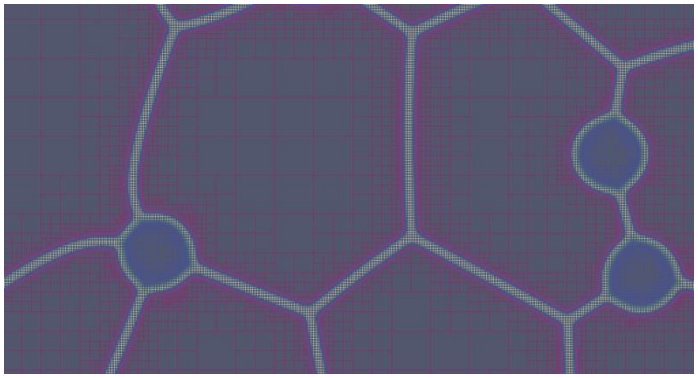

Figure 4.2. Different equilibrium pore configurations at two-, three-, and four-grain junctions. In general, the equilibrium pore configuration depends on the dihedral angle and the pore coordination number (e.g., the number of grains attached to the pore). This simulation was performed in MARMOT with adaptive mesh, i.e., the mesh at the interfaces is much finer than in the bulk regions.

4.1.2 Shrinkage of an Isolated Circular Grain

In the absence of pores, the grain boundary migrates under the influence of its curvature as was discussed in Chapter 2. This gives rise to the well-known parabolic grain growth

kinetics (see Eq. 2.4). The simplest example for studying such kinetics is the shrinkage of an isolated circular grain embedded in a matrix grain. The solution of Eq. (2.20) for this case is simply given by

$$A(t) - A_{\circ} = -k\,t\,, \tag{4.1a}$$

$$k = 2\pi\gamma_{\mathrm{gb}} M_{\mathrm{b}} = 2\pi L\kappa_{\eta}\,. \tag{4.1b}$$

Here, $A(t)$ is the grain area at time, t , $A_{\circ}$ is the initial grain area and k is the rate constant. The last equality in Eq. (4.1b) is based on the relation of Eq. (3.9) that relates the sharp- and diffuse-interface parameters. A simulation of this test case was carried out in MARMOT. Snapshots of this simulation are shown in Figure 4.3. The initial interface width was 20 and the initial grain radius was 600. The values of the non-dimensionalized model parameters that appear in Eq. (4.1b) were $\tilde{\kappa}_{\eta} = 15$, and $\tilde{L} = 1.0$. The kinetics of the shrinkage is quantitatively captured in Figure 4.4. As evident from the figure, the kinetics follows the linear relation of Eq. (4.1). The value of the rate constant calculated from Eq. (4.1b) is 94.2, while the value from the simulation (the slope in Figure 4.4) is 96.

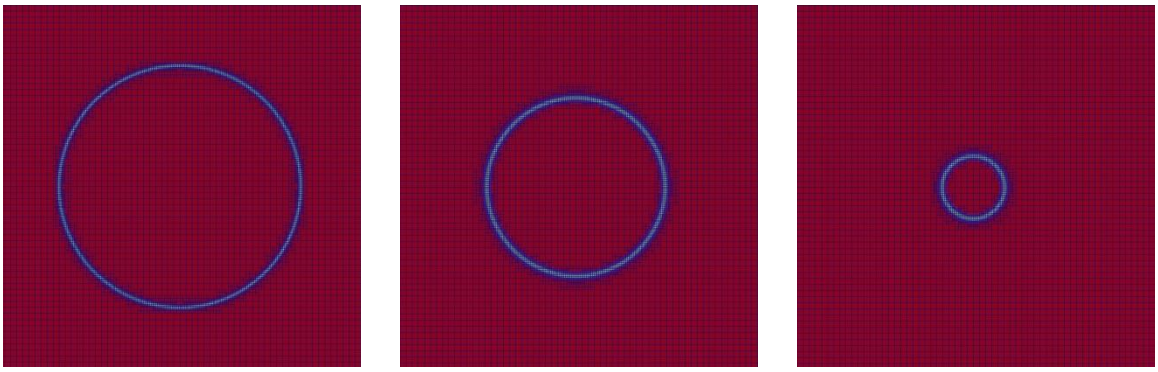

Figure 4.3. Snapshots of the shrinkage of an isolated circular grain embedded in a matrix grain. The simulation was performed using MARMOT with adaptive mesh.

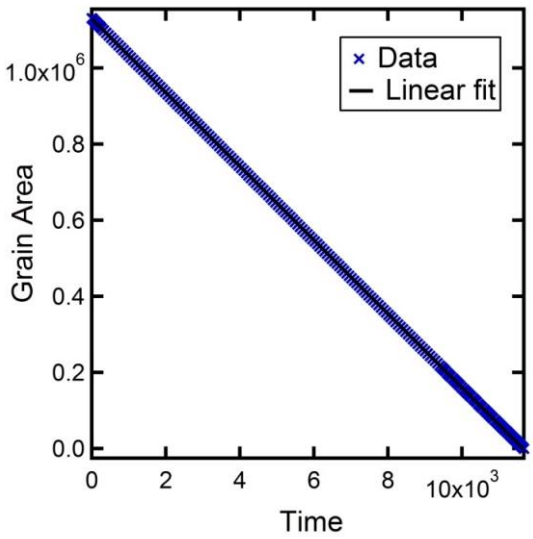

Figure 4.4. The kinetics of the shrinkage of an isolated circular grain embedded in a matrix grain. The kinetics follows closely the relation of Eq. (4.1). The markers represent the simulation data and the line is the fit to Eq. (4.1).

4.1.3 Flatting of a Perturbed Solid Surface via Surface Diffusion

It is well-established that a slightly curved solid surface evolves into a flat surface to decrease its surface area and hence its surface energy [64-66, 142]. Such process takes place by matter transport from the higher curvature side to the lower curvature side via surface diffusion, evaporation and consideration, or volume diffusion. For the case of surface diffusion, the surface velocity is given by Eq. (2.24). For a slightly perturbed surface, Eq. (2.24) can be linearized and the decay rate of the amplitude of surface perturbation can be derived [64-66, 142-145]. For example, the decay rate of the amplitude of perturbation of a surface perturbed by a long wavelength sinusoid is given by

$$A(t) = A(0)\exp[-\gamma_s B_s (2\pi/\lambda)^4 t], \tag{4.2a}$$

$$B_s = \frac{D_s w \upsilon_m}{RT} . \tag{4.2b}$$

In the above, $A(t)$ is the perturbation amplitude at time, t , $A(0)$ is the initial amplitude of perturbation, λ is the perturbation wavelength and B_s is the surface mobility.

A simulation of this test case was conducted using MARMOT. In the simulation, the values of the geometrical parameters were: $A(0) = 100$ and $\lambda = 2000$. Note that the condition $A/\lambda << 1$ must be satisfied in order for the linear approximation to hold. The phase field model parameters took on the values: $\tilde{\kappa}_\rho = 45$, $\tilde{\kappa}_\eta = 15$, and $\tilde{M}_s = 83$. Recall that, from the matching between the sharp- and diffuse-interface models, we have the relation (see Eq. (3.9))

$$M_s(\kappa_\rho + \kappa_\eta) = \gamma_s B_s = \frac{\gamma_s D_s w \upsilon_m}{RT} . \tag{4.3}$$

The evolution of the perturbed surface is captured in Figure 4.5. The kinetics of the decay of the perturbed surface is shown in Figure 4.6. As clear from the figure, the phase field model solution agrees well with the analytical relation of Eq. (4.2). The decay constant defined as $\tau = \gamma_s B_s (2\pi/\lambda)^4 = M_s(\kappa_\rho + \kappa_\eta)(2\pi/\lambda)^4$ equals 4.3×10^{-7}, the simulation gave a value of 4.33×10^{-7}.

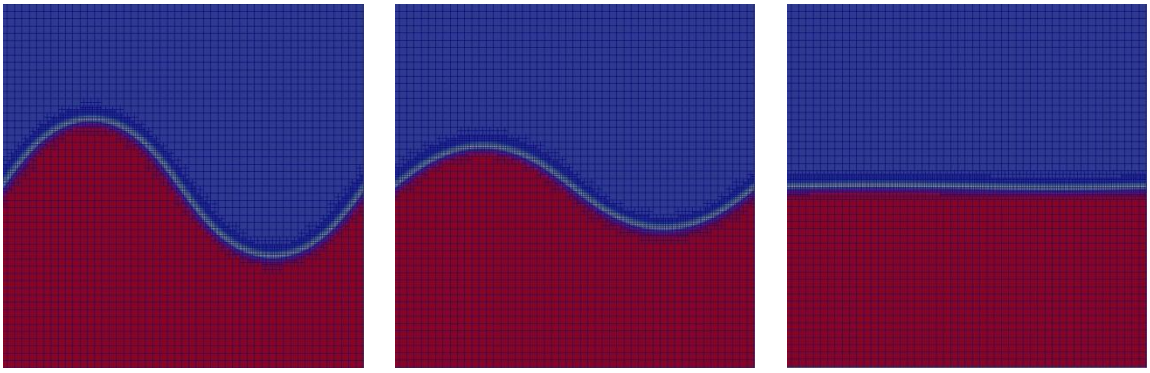

Figure 4.5. Snapshots of the decay of a sinusoidal surface between a solid phase (shown in red) and a vapor/gas phase (shown in blue). The simulation was carried out using MARMOT with adaptive mesh.

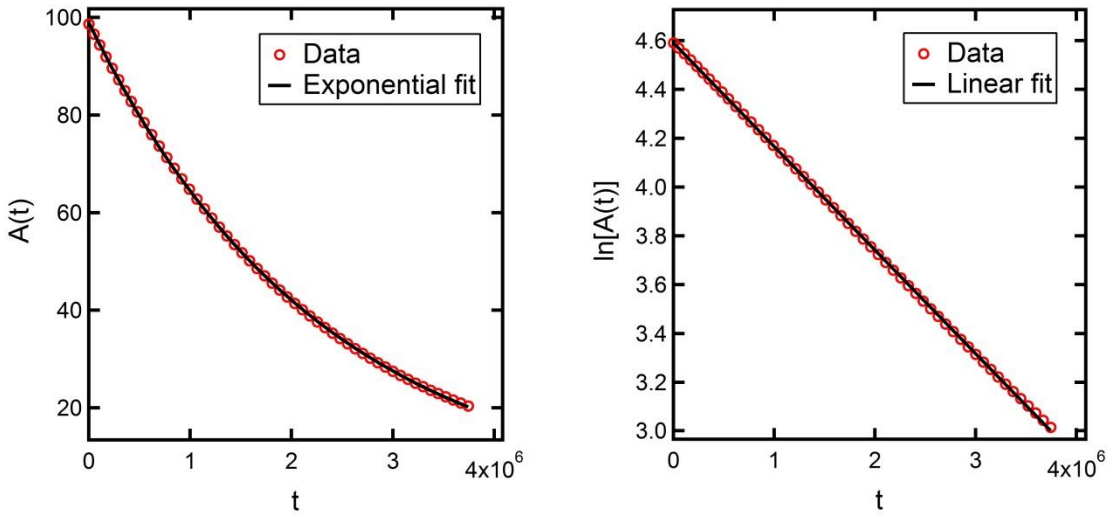

(a) (b)

Figure 4.6. The kinetics of the decay of the amplitude of a sinusoidal surface via surface diffusion: (a) exponential fit and (b) linear fit.

4.1.4 Instability of Cylindrical Second-phase Particles during Coarsening

It has been shown that cylindrical second-phase particles are unstable and transform into spherical particles during coarsening [64, 146-149]. This is the mechanism by which open porosity (interconnected cylindrical pores) changes into closed porosity (isolated

spherical pores) during the final stage of sintering. The instability of a cylindrical shape under the influence of capillarity was first shown by Rayleigh [146]. The driving force is the minimization of the interfacial free energy via the reduction of the interfacial area. The kinetic mechanism by which this process takes place may be surface diffusion, evaporation and condensation, or volume diffusion. However, there are two different evolution paths for a slightly perturbed cylindrical particle to decrease its surface energy, e,g,, ovulation and spheroidization. This is schematically depicted in Figure 4.7. It was found out that there is a critical wavelength above which ovulation takes place (i.e., the perturbation grows) and the particle breaks up into two or more spheres. This critical wavelength is given by

$$\lambda_0 = 2\pi R_0 , \tag{4.4}$$

where λ_0 is the critical wavelength and R_0 is the initial radius of the cylinder. This is a morphological instability commonly known as Rayleigh instability [146]. On the other hand, if the wavelength of the perturbation is below the critical value, spheroidization takes place (i.e., the perturbation decays) and the cylindrical particle transform into only one spherical particle.

Two simulations were performed using MARMOT in 3D to study the spheroidization and ovulation of cylindrical pores. In both cases, the initial condition is a cylindrical pore perturbed by a sinusoid and embedded in a matrix grain. The perturbation is radially symmetric, e.g.,

$$R(z) = R_0 + A\cos\frac{2\pi}{\lambda}z , \tag{4.5}$$

with $A = 10$.

The phase field model parameters took on the values: $\tilde{\kappa}_\rho = 45$, $\tilde{\kappa}_\eta = 15$, and $\tilde{M}_s = 10$.

In the first simulation, the geometrical parameters were $R_0 = 50$ and $\lambda = 200$. Therefore, according to Eq. (4.4), spheroidization takes place and only one spherical particle is formed. This is shown in Figure 4.8. In the second simulation, the geometrical parameters were $R_0 = 50$ and $\lambda = 400$. Hence, ovulation takes place and the cylindrical particle breaks up into two spherical particles. This is captured in Figure 4.9.

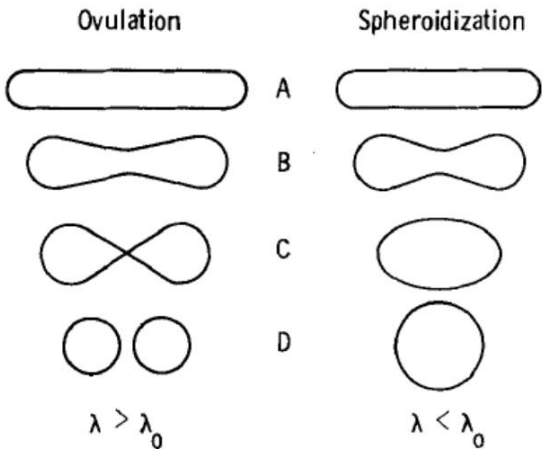

Figure 4.7. A schematic illustration of ovulation and spheroidization. If the initial wavelength of perturbation is larger than the critical wavelength (see Eq. (4.4)), ovulation takes place and the cylindrical particle breaks up into two spherical particles. Otherwise, spheroidization proceeds, and only one spherical particle is formed [149].

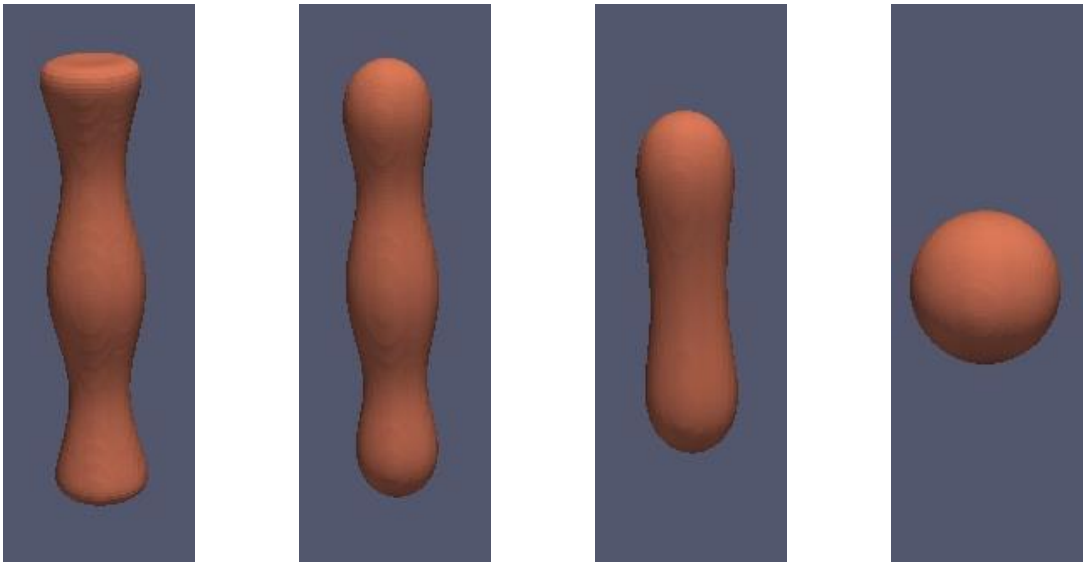

Figure 4.8. Snapshots of the evolution of the isosurface of a 3D cylindrical pore with $\lambda < 2\pi R_0$. For short-wavelength perturbations, spheroidization takes place and only one spherical particle is formed.

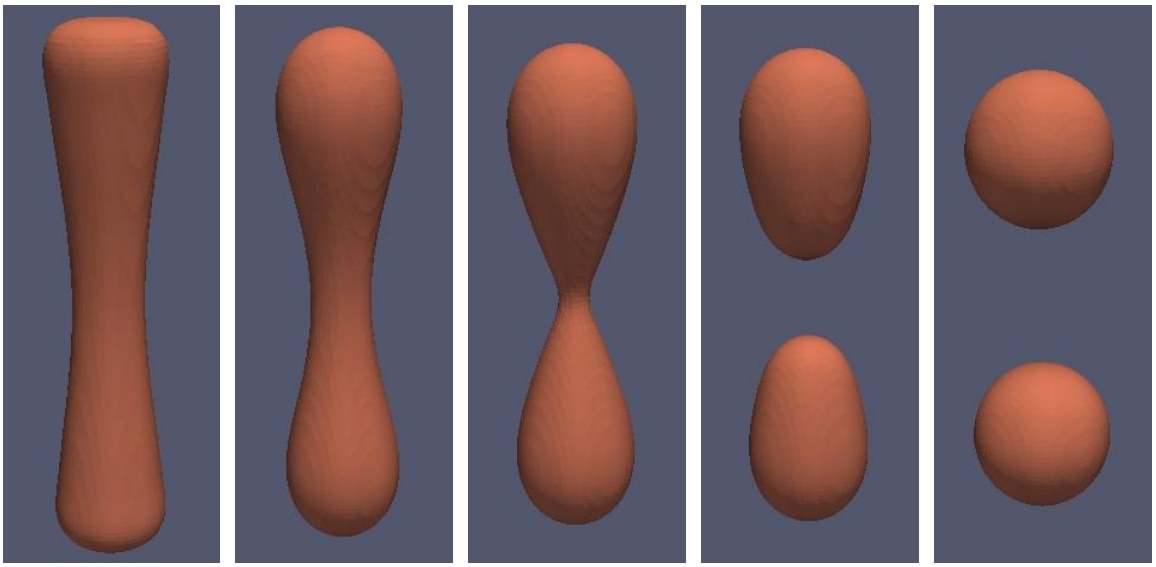

Figure 4.9. Snapshots of the evolution of the isosurface of a 3D cylindrical pore with $\lambda > 2\pi R_0$. For long-wavelength perturbations, ovulation takes place and the cylindrical particle breaks up into two spherical particles.

4.1.5 Sintering of Two Unequal-sized Grains

As a final test case, we study here the classical example of the grain growth during the sintering of two unequal-sized grains. Consider two barely touching circular grains as depicted in Figure 4.10. The small grain has a radius of 20 grid points or pixels while the large one has a radius of 30 grid points. The evolution of this two-grain system is captured in Figure 4.10. As the figure shows, the neck between the two grains is first formed with the aid of surface diffusion. Then concurrent grain and neck growth is observed. In the final stage, grain growth proceeds until the equilibrium configuration of one circular grain is established. In this simulation, we set $B = 11C$ and $\kappa_\rho = 2\kappa_\eta$, and the ratio of Cahn-Hilliard to Allen-Cahn mobility was set to 10. The radius of the small grain and the neck (now the grain boundary) size were used as indicators of the extent of system evolution. The area of each grain is calculated as $\int \eta_i \, dA$ while the neck size was approximated by $\int \eta_1 \times \eta_2 \, dA$ which has non-zero value only at the neck (grain boundary). The evolution time is presented as a fraction of the total simulation time, t_s. These quantitative results are presented in Figure 4.11. As can be seen in Figure 4.11, the overall evolution process can be divided into three stages. In the first stage, the neck (grain boundary) between the two grains grows quickly without any noticeable change in grain size. In the second stage, there is a concurrent neck growth and grain growth or shrinkage (the large grain grows while the small grain shrinks). In the third stage, the grain growth or shrinkage continues but the neck size starts to decrease. The final stage continues until the small grain disappears.

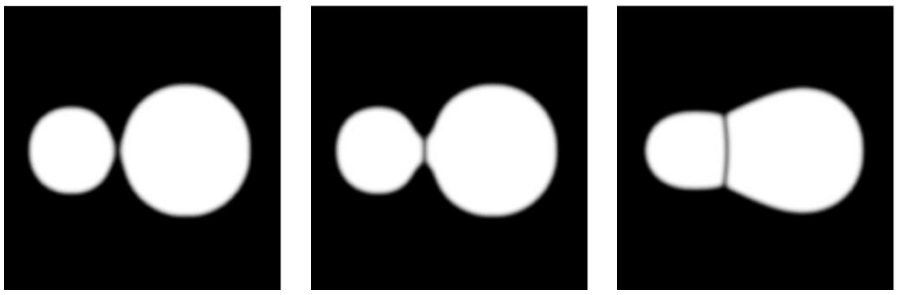

(a) $t / t_s = 0$ (b) $t / t_s = 0.1$ (c) $t / t_s = 0.25$

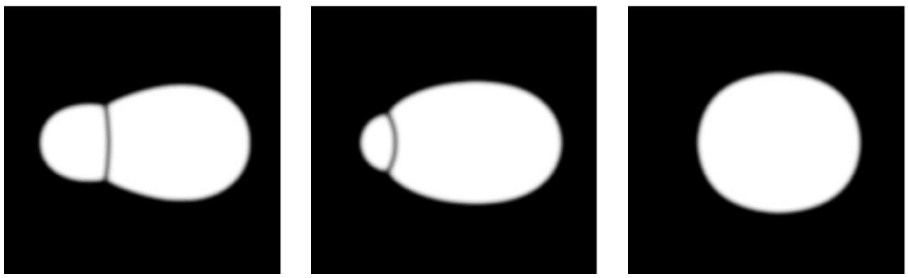

(d) $t / t_s = 0.6$ (e) $t / t_s = 0.8$ (f) $t / t_s = 1.0$

Figure 4.10. Snapshots of the evolution of a system of two unequal circular grains illustrating the stages of neck formation, concurrent widening of the neck and growth of the larger grain, and the final neck shrinkage and complete disappearance of the smaller grain [56].

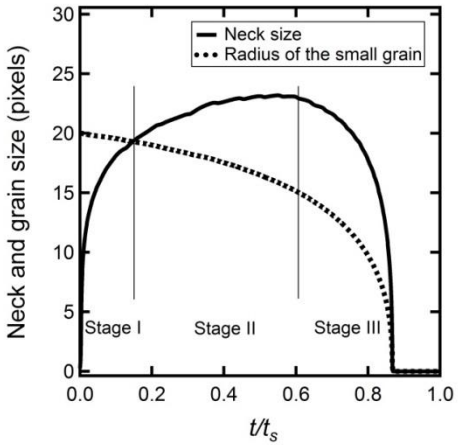

Figure 4.11. Different stages of sintering of two unequal circular grains; neck formation and growth dominate the initial stage, concurrent grain and neck growth mark the intermediate stage, and the small grain completely disappears in the final stage [56].

4.2 Pore Drag Effect on the Kinetics of Grain Growth

In this section, the effect of the presence of pores on the kinetics of grain growth is examined in details using idealized 2D configurations of the pore and the grain boundary. Tow particular cases are considered here. In the first example, the effect of pore retardation on the shrinkage kinetics of an isolated circular grain embedded in a matrix grain is discussed. The effect of the number of pores on the boundary and the pore surface mobility on the kinetics are examined. In the second example, the pore retarding effect on the shrinkage of a four-sided grain is investigated. The retarding effects of two pore configurations, e.g., edge pores (pores on two-grain junctions) and corner pores (pores on three-grain junctions) are addressed. All the simulations presented in this section were conducted using the fully-coupled, fully-implicit finite-element scheme implemented in MARMOT. Since the goal of this section is to examine the general behavior of the pore-grain boundary interactions, the model equations are solved in a non-dimensionalized setting.

4.2.1 Shrinkage of an Isolated Circular Grain with Boundary Pores

As was discussed in section 4.1, the shrinkage of an isolated circular grain embedded in a matrix grain is the simplest example to study the kinetics of ideal grain growth. Hence, it is instructive to utilize the same example to examine the pore drag effect on the grain growth kinetics in porous solids. In this case, pores were introduced on the boundary of the circular grain. The number of pores and their surface diffusivity were varied to investigate their effect on the grain growth kinetics. In the following examples, the initial grain radius was 600 and the initial pore radius was 75.

In the first set of simulations, the pore (free) surface mobility ($\tilde{M}_s$) was set to 100, while the number of pores on the grain boundary was varied to examine its effect on the grain growth process. A set of snapshots of these simulations is shown in Figure 4.12. As evident from Figure 4.12, the first notable effect that is common in all cases irrespective of the number of pores is the anisotropic shrinkage of the initially circular grain. The circular grain changes its shape while shrinking depending on the distribution of pores. Only for the case of 8 pores evenly distributed on the boundary (the last row of snapshots in Figure 4.12) that the shrinkage is near isotropic. This clearly shows that the pores act as obstacles for the grain boundary motion reducing its intrinsic velocity.

When only one pore is present (see the first two row of Figure 4.12), the boundary experiences minimal drag. This evident from the fact that the boundary drags the pore with it only for a short distance; this can be easily checked by noticing that the initial and final position of the pore is almost the same. On the other hand, when two or more pores are present, the effect of drag becomes increasingly more pronounced (see Figure 4.12). The grain boundary starts dragging the pores along with it. However, the grain boundary can manage to break away from the pore as for the cases of two and three pores (see second and third rows of Figure 4.12). Nonetheless, as the number of pores increases, the drag effect becomes more pronounced and the boundary can no longer break away from the pores. In fact, for four or more pores and after a short initial transient, the pore moves along with the grain boundary as a rigid-body. This can be explained as follows. When surface diffusion is fast enough, matter can be transported quickly from the leading surface of the pore to the trailing surface and the pore moves forward with the grain boundary as a rigid-body. Recall that all the classical models assume the rigid-body

motion of the pores [1, 46-48]. Moreover, 2D numerical solutions of the sharp-interface models showed that this is a reasonable assumption in the limit of low velocity [49-53].

The effect of the number of pores on the shrinkage kinetics of the circular grain is captured quantitatively in Figure 4.13. In that figure, the evolution of the area of the shrinking grain with different number of pores is presented. The retarding effect of the pores on the kinetics is clear. As the number of pores increases, the shrinkage rate decreases. This agrees well with the predictions of the classical models as discussed in Chapter 2, i.e., recall that the velocity of pore-boundary complex is inversely proportional to the number of pores on the boundary (see Eq. (2.15)).

In the second case study investigated here, the number of pores was held constant while the pore surface mobility was varied to investigate its effect on the kinetics. Since the shrinkage is almost isotropic when eight pores are evenly distributed on the boundary (see the last row of snapshots in Figure 4.12), this configuration was chosen to study the effect of surface mobility. Figure 4.14 captures the effect of surface mobility on the shrinkage kinetics. The figure presents the evolution of the area of the shrinking grain with different values for the pore surface mobility. As evident from the figure, higher surface mobility results in faster shrinkage kinetics. This is of course to be expected since higher surface mobility means faster surface diffusion. Fast surface diffusion kinetics allows the pores to be easily dragged by the migrating boundary. Nonetheless, this captures the main difference between the effect of pore drag and the immobile particles (Zener's type) drag on the grain growth kinetics. The latter is a static drag that depends only on geometric parameters such as the particle radius and volume fraction (recall Eq.

(2.7)), while the former is a kinetic drag that depends on kinetic parameters such as the pore surface mobility.

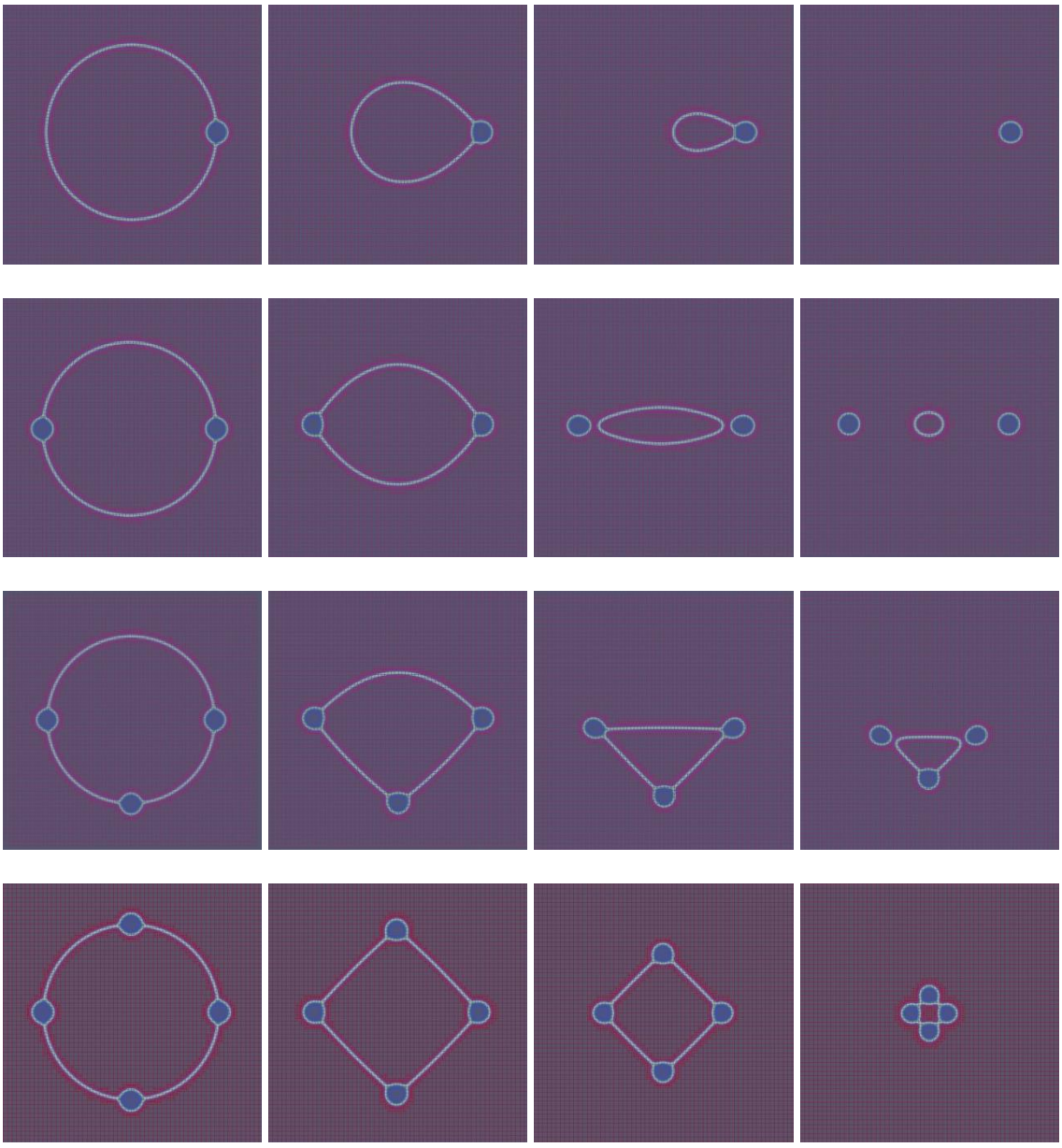

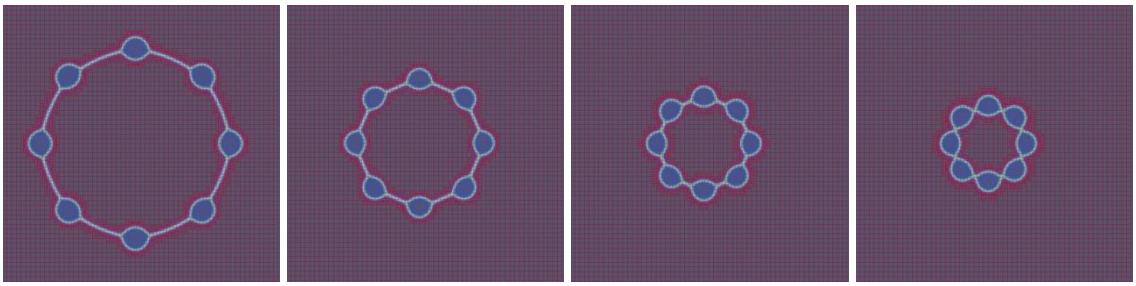

Figure 4.12. Effect of pore drag on the shrinkage of a circular grain. The presence of pores leads to anisotropic shrinkage of the initially circular grain. The shrinkage rate decreases with increasing the number of boundary pores. For only one present, the pore drag effect is minimal. When two or three pores are present, the boundary can separates from the pore. However, for higher number of pores, the boundary can no longer detaches from the pore; instead, for high enough surface mobility, the pore moves along with the boundary as a rigid-body, i.e., without changing its shape or size.

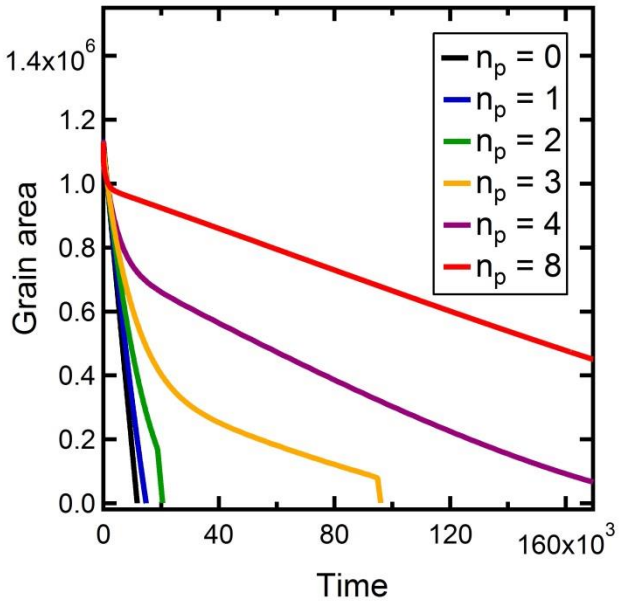

Figure 4.13. Effect of pore drag on the kinetics of the shrinkage of a circular grain with boundary pores (see Figure 4.12). The presence of pores hinders the grain boundary motion. As the number of pores increases, the shrinkage rate decreases.

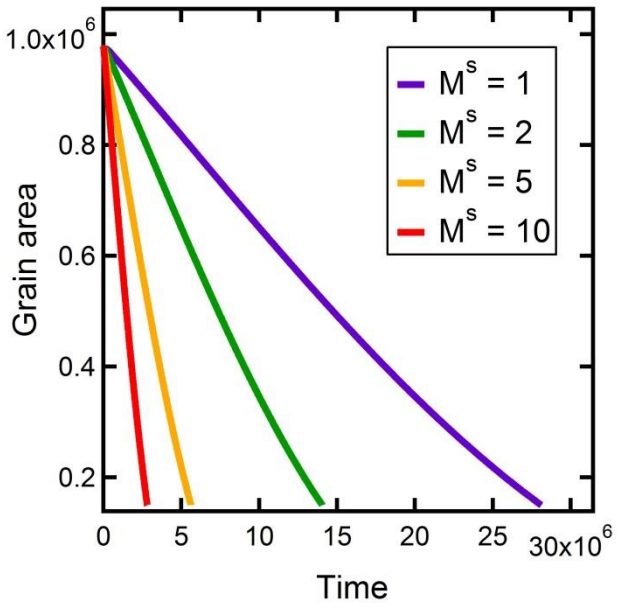

Figure 4.14. Effect of the pore (free) surface mobility on the kinetics of the shrinkage of a circular grain with eight pores on its boundary (see the last row of snapshots in Figure 4.12). Higher surface mobility leads to faster surface diffusion resulting in higher pore velocity. The higher the pore velocity, the less extent of drag the pore exerts on the grain boundary.

4.2.2 Shrinkage of a Four-sided Grain with Edge and Corner pores

Another important case study that helps in understanding the nature of pore drag is the shrinkage of a four-sided grain with different pore configurations. In this example, two different pore configurations are considered, e.g. edge pores (pores on two-grain junctions) and corner pores (pores on triple-junctions). Hence, the effect of pore configuration on the grain growth kinetics can be investigated.

Before investigating the shrinkage of a four-sided grain with different pore configuration, it is instructive to study the pore-free case first. According to the well-known topological analysis of grain growth put forward by Neumann and Mullins [4, 64], a grain with more than six sides will grow, while a grain with less than six sides will

shrink. A grain with six sides is static. The growth/shrinkage rate of a grain with *N* sides is given by [4, 64]

$$\frac{dA(N)}{dt} = \frac{\pi}{3}\gamma_{\mathrm{gb}} M_{\mathrm{b}} (N-6), \tag{4.6}$$

where, $A(N)$ is the area of a grain with *N* sides.

A simulation of the shrinkage of a four-sided grain was performed with the following values of the non-dimensionalized model parameters $\tilde{\kappa}_\eta = 15$, and $\tilde{L} = 1.0$. The initial grain size of the four-sided grain was 1200. In this example, natural boundary conditions for all the variables were applied. Snapshots of the shrinkage of the four-sided grain are presented in Figure 4.15. The shrinkage kinetics is captured in Figure 4.16 which shows the evolution of the grain area with time. As evident from the figure, the area decreases linearly with time in agreement with Eq. (4.6). The non-dimensionalized rate constant calculated from Eq. (4.6), taking into account the matching relation of Eq. (3.9a), was 31.4, while the value obtained from the simulation was 31.8.

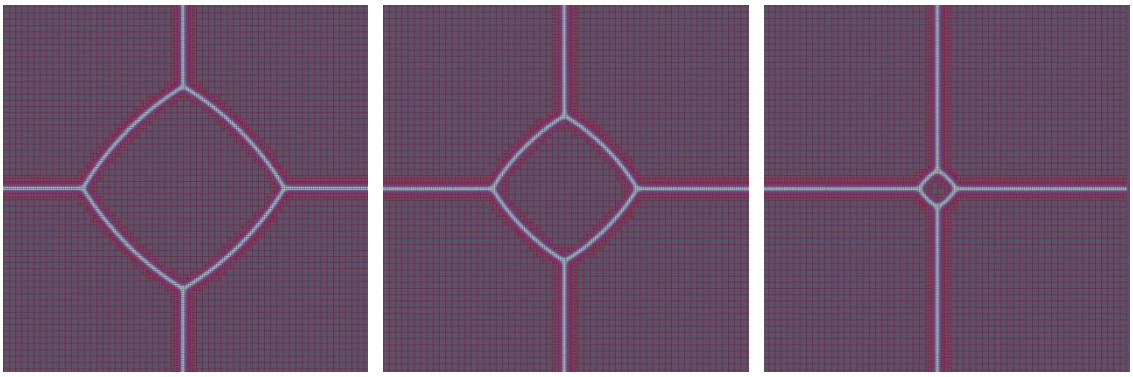

Figure 4.15. Snapshots of the shrinkage of a four-sided grain.

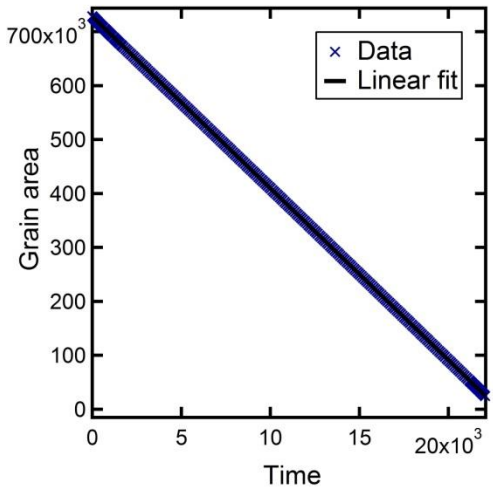

Figure 4.16. The shrinkage kinetics of a four-sided grain. The grain area decreases linearly with time in agreement with the Neumann-Mullins relation (see Eq. (4.6)).

Now we turn our attention to the case of the effect of pore configuration on the shrinkage/growth kinetics. Simulations of the shrinkage of a four-sided grain with edge and corner pores were conducted. In these simulation, the non-dimensionalized model parameters took on the values: $\tilde{\kappa}_\eta = 15$, $\tilde{L} = 1.0$, $\tilde{\kappa}_\rho = 45$, and $\tilde{M}_s = 100$. The initial grain size was 1200 and the initial pore radius was 75. Figure 4.17 shows snapshots of the shrinkage of a four-sided grain with edge and corner pores. Similar to the case of the shrinkage of a circular grain with boundary pores, pores move along with the boundary as a rigid-body when surface mobility is high. However, the rate of shrinkage depends strongly on the pore configuration. Edge pores are much easier to be dragged by the migrating boundary than corner pores. This is due to the fact that edge pores have higher curvature than corner pores. Higher curvature leads to higher surface diffusion kinetics and hence higher pore velocity. This is captured quantitatively in Figure 4.18 which presents the evolution of the grain area with edge and corner pores.

One can assign an effective rate constant for each configuration (recall that an effective mobility for the pore-boundary complex was introduced in Eq. (2.15)). This effective rate constant can be directly calculated from Figure 4.18. The non-dimensionalized effective rate constant was 1.05 for the case of edge pores and 0.85 for the case of corner pores (recall that the rate constant was 31.8 for the pore-free case).

The last case study to be considered here is the Ostwald ripening of the pores that may take place concurrently with grain growth in porous polycrystalline solids [1, 48-53]. When grain boundary and/or bulk diffusion are active, vacancies diffuse from smaller (higher curvature) pores to larger (lower curvature) pores. Hence, the number of pores decreases while their average size increases during coarsening. Hartland and Crocker [53] showed that corner pores grow at the expense of edge pores. In order to simulate this example here, bulk diffusion is considered to be active. The bulk diffusion mobility is formulated as

$$\mathbf{M}_{\mathrm{b}} = M_{\mathrm{b}}\xi(\rho)\mathbf{I}, \tag{4.7a}$$

$$\xi(\rho) = \rho^3(10 - 15\rho + 6\rho^2)\,. \tag{4.7b}$$

In the above, $\mathbf{M}_{\mathrm{b}}$ is the bulk (volume) mobility tensor, M_{b} is the bulk mobility coefficient of the material, and $\xi(\rho)$ is an interpolation function which guarantees nontrivial values of bulk mobility in the solid region and zero values in the pores. Now, the mobility tensor that appears in Eq. (3.3) is the total mobility tensor with both bulk and surface diffusion. In the example presented here, $\tilde{M}_{\mathrm{s}} = 100$ and $\tilde{M}_{\mathrm{b}} = 1$. Snapshots of the shrinkage of a four-sided grain with both edge and corner pores are shown in Figure 4.19. As evident from the figure, edge pores shrink while corner pores grow in agreement with

the results of Hartland and Crocker [53]. It is worth noting that the Ostwald ripening of the pores affects the grain growth kinetics. This is captured in Figure 4.20 which shows the shrinkage kinetics. After the edge pores disappear, the rate of shrinkage decreases. This due to the fact that the more mobile edge pores have transformed into the less mobile corner pores. Therefore, Ostwald ripening of the pores increases the extent of drag experienced by the boundary which retards the shrinkage/growth kinetics.

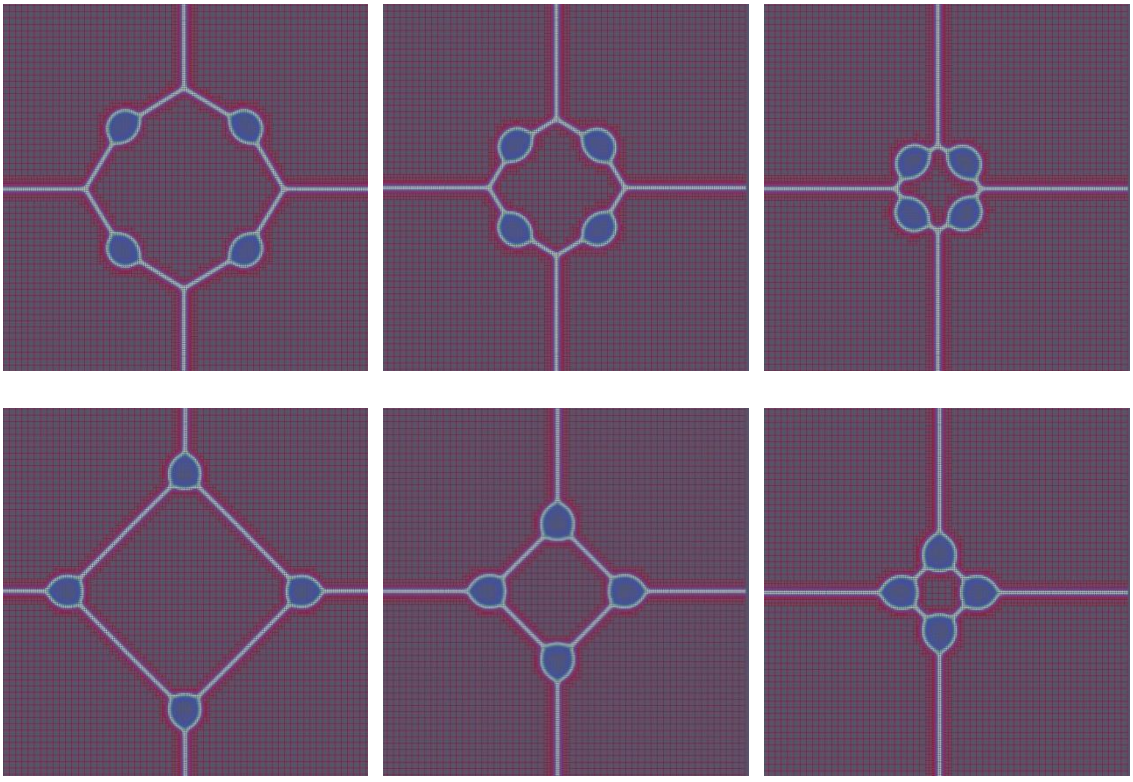

Figure 4.17. Snapshots of the shrinkage of a four-sided grain with edge (top row) and corner (bottom row) pores. In common with the case of the shrinkage of a circular grain with boundary pores (see Figure 4.12), the pore moves along with the boundary as a rigid-body when the surface mobility is high enough.

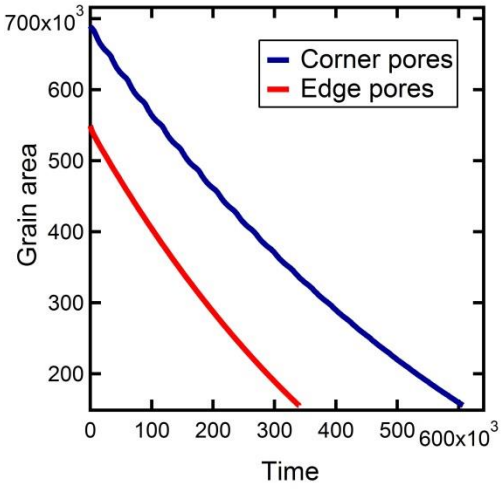

Figure 4.18. Effect of the pore configuration on the shrinkage kinetics of a four-sided grain. The grain with edge pores shrinks faster. This is due to the fact that edge pores have higher curvature and hence higher surface diffusion kinetics. Therefore, edge pores exert less drag on the boundary than corner pores.

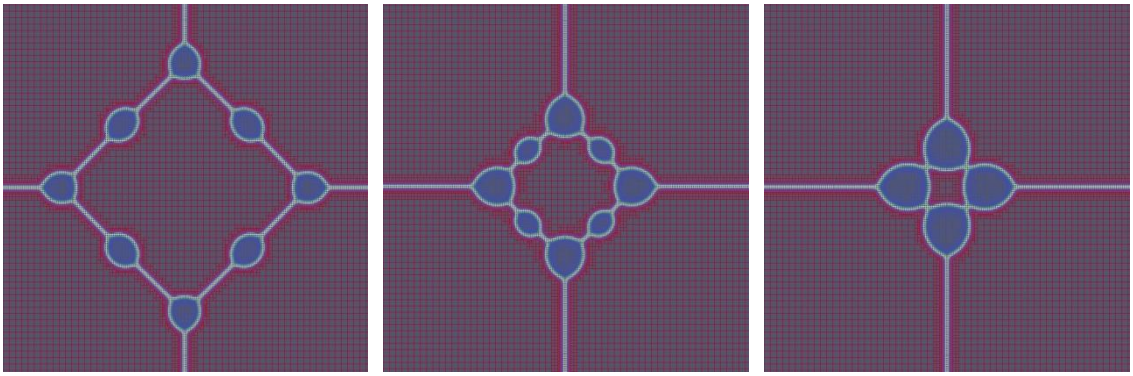

Figure 4.19. Snapshots of the shrinkage of a four-sided grain with both edge and corner pores. Edge pores shrink while corner pores grow due to the vacancy diffusion from the former to the latter. This is commonly referred to as the Ostwald ripening of the pores [1, 53].

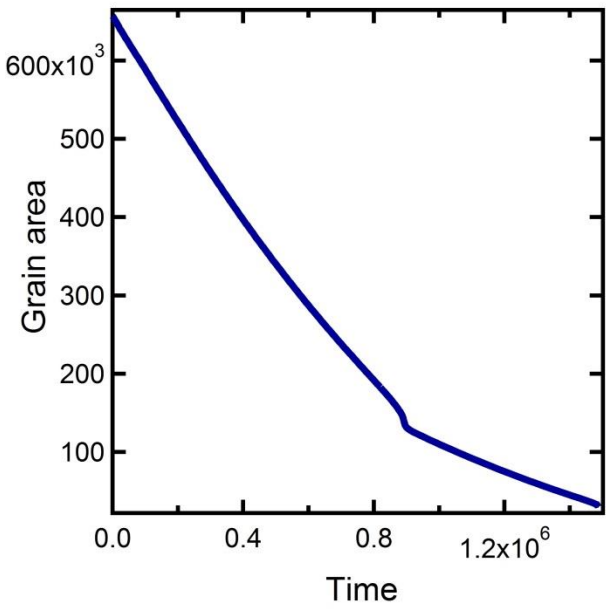

Figure 4.20. The shrinkage kinetics of a four-sided grain with edge and corner pores (see Figure 4.19). After the edge pores disappear (see Figure 4.19), the shrinkage rate decreases.

4.3 2D Simulations of Grain Growth in Porous Uranium Dioxide

In this section, we investigate the process of grain growth in porous polycrystalline uranium dioxide. In applying the model to UO_2, surface and grain boundary energies were taken to be 0.6 and 0.3 J/m^2, respectively [150]. Referring to Eq. (3.7) and assuming a grain boundary width of 1nm, the free energy parameters were determined to be: $B = 1.9176 \times 10^9$ J/m^3, $C = 1.128 \times 10^8$ J/m^3, $\kappa_\eta = 6 \times 10^{-10}$ J/m and $\kappa_\rho = 1.8 \times 10^{-9}$ J/m. The surface diffusion coefficient is directly taken from [151]. The boundary mobility is taken from [150]. The results presented here were obtained using the explicit finite-difference scheme. These results were also published in [57].

A Voronoi tessellation was utilized to generate the initial polycrystalline structure, where each grain is assigned a different order parameter to prevent the unphysical coalescence of grains during the simulation. Pores were then distributed randomly on grain boundaries to mimic the actual microstructure of materials in the final stage of sintering where grain growth takes place. In all simulations presented in this section, an ensemble of 200 grains (and equal number of non-conserved order parameters) on a 700×700 finite difference grid was used. The number, size and distribution of pores were varied to investigate their effect on the kinetics of grain growth in UO_2. Periodic boundary conditions were applied to minimize the effect of domain size on the kinetics of grain growth. Parallel computing was utilized to overcome the high computational cost associated with the large number of order parameters.

The results obtained for grain growth in the fully dense UO_2 are shown in Figures 4.21 and 4.22. Figure 4.21 captures the microstructure evolution of UO_2 at 1727°C. As

expected, in the case of fully dense ceramics, the larger grains grow at the expense of the smaller ones to reduce the excess free energy associated with grain boundary network. The kinetics of the grain growth in pore-free UO_2 is presented in Figure 4.22(a) which shows the evolution of the average grain area with time at three different temperatures. The effect of temperature was considered through the dependence of the boundary mobility on temperature [57]. The average grain area increases linearly with time in accordance with the parabolic growth law for the average grain size. Increasing the temperature accelerates the growth rate, represented by an increased slope of the linear fits in Figure 4.22(a). Figure 4.22(b) is an Arrhenius plot that was generated using the growth data at different temperatures. The activation energy, which is the negative of the slope of the Arrhenius plot, was found to be 237 KJ/mol in good agreement with the activation energy for boundary diffusion value of 239 KJ/mol, as expected for grain growth in fully dense solids.

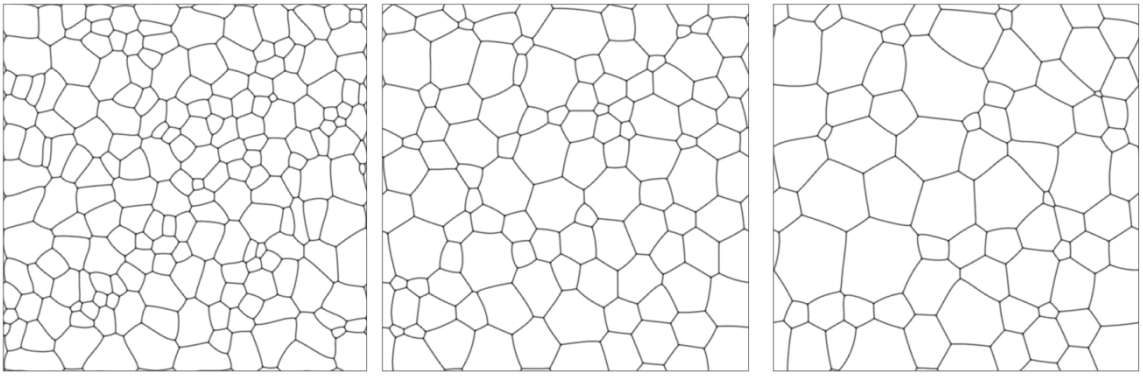

(a) t =1 min (b) t =20 min (c) t =1h

Figure 4.21. Snapshots of microstructure evolution of fully dense (pore-free) UO_2 at 1727 °C [57].

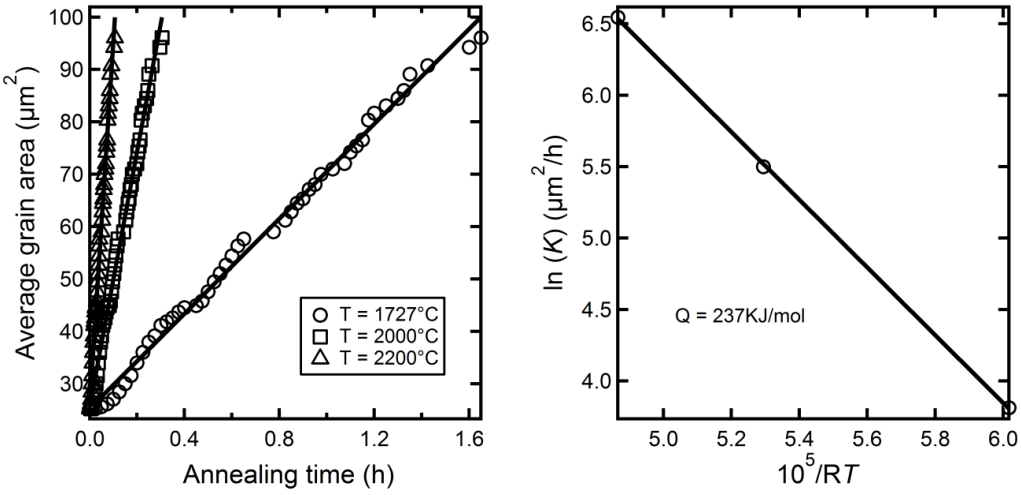

(a) (b)

Figure 4.22. Kinetics of grain growth in fully dense UO_2. (a) Evolution of average grain area at different temperatures. (b) Arrhenius plot for calculating the activation energy in non-porous UO_2 showing an activation energy value of 237 KJ/mol. The markers represent the data points while the straight lines are the best fit [57].

As mentioned earlier, in porous materials a competition between pore controlled and boundary controlled growth kinetics takes place. The boundary mobility, pore mobility and pore fraction are the key factors that determine which kinetics prevails. These factors could be stated in terms of the phase field model parameters as follows. If $M_s \gg N_p r^2 L$, the growth follows a boundary controlled kinetics. On the other hand, if $M_s \ll N_p r^2 L$, the growth follows a pore controlled kinetics. Otherwise, mixed kinetics is expected.

For the sake of investigating such scenarios in the case of UO_2, different initial ensembles of grains and pores were created. Each ensemble has 200 grains and different numbers of pores of different pore sizes. The density of pores was varied to enable the investigation the effect of porosity on the kinetics of grain growth in uranium dioxide.

Several simulation cases were considered. In the first case, an ensemble of 200 grains with initial grain size of 4.7 μm and 75 pores with pore size of 1 μm was

considered. This gives pore volume fraction, f, of 0.025 and N_p of about 0.25. Figure 4.23 depicts the microstructure evolution of that ensemble at 1727 °C. Pores migrate with boundaries and are expected to coalesce as they are swept by the grain boundaries. As expected, the figure clearly shows that pore-free boundaries migrate much faster than boundaries with pores. This could lead to abnormal grain growth if the pores are not uniformly distributed on the boundaries as will be discussed later. The grain growth kinetics is quantitatively described in Figure 4.24(a), which shows the evolution of the average grain size with time. It was found that it is best fit to a power law with exponent of 3.25. Non-integer values between 3 and 4 for the growth exponent in UO_2 were reported before [36, 37]. The value of the exponent suggests that the grain growth in the current case exhibits mixed kinetics.

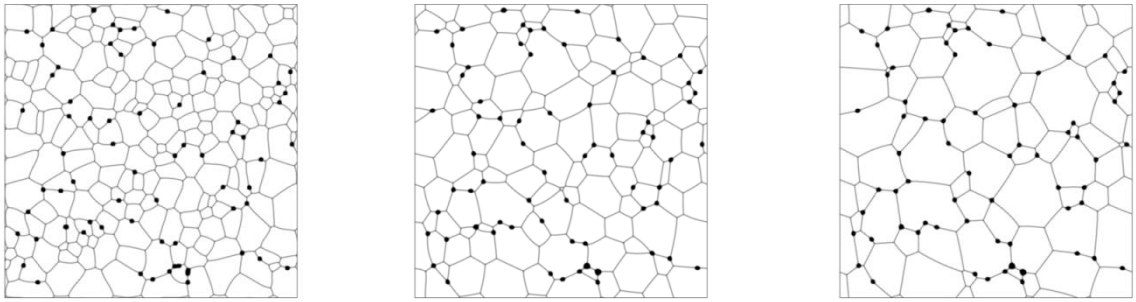

(a) *t*=1min (b) *t*=1h (c) *t*=2h

Figure 4.23. Snapshots of microstructure evolution of slightly porous UO_2 ($f = 0.025$, $N_p = 0.25$) at 1727°C [57].

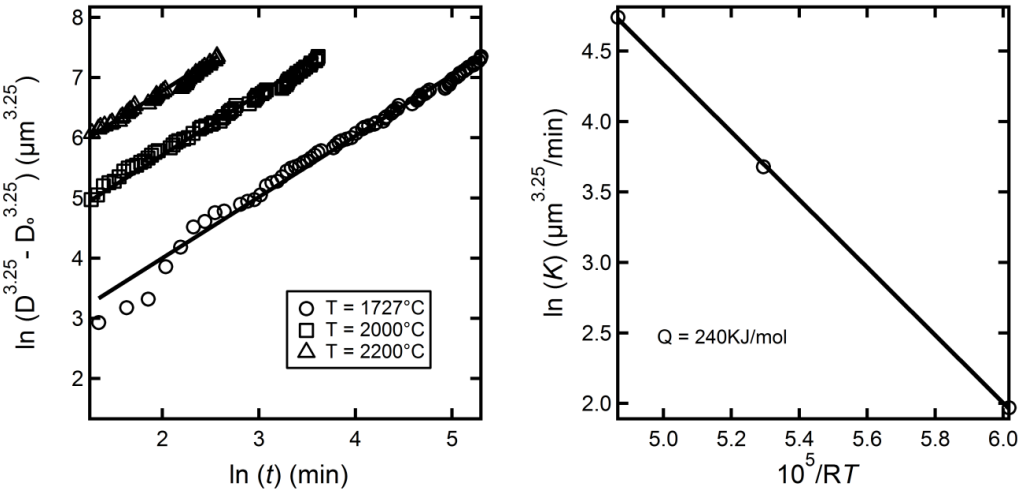

Figure 4.24. Kinetics of grain growth in slightly porous UO_2 ($f = 0.025$, $N_p = 0.25$). (a) Evolution of the average grain size at different temperatures following a power law with exponent of 3.25. (b) Arrhenius plot for the rate constant with an activation energy of 240 KJ/mol. The markers represent the data points while the straight lines are the best fit [57].

In a second example, an ensemble of 200 grains with initial grain size of 4.7 μm and 125 pores with pore size of 1 μm is considered. This fixes f as 0.04 and N_p as 0.4. Figure 4.25(a) represents the average grain size growth with time. In this case, the best fit was a power law with exponent of 4 as expected for pore controlled grain growth when pore migration takes place via surface diffusion. Hence, grain growth in UO_2 follows pore controlled kinetics when $N_p \geq 100M / Lr^2$. The activation energy was found to be 227 KJ/mol as calculated from the Arrhenius plot shown in Figure 4.25(b).

A growth exponent of 4 for grain growth kinetics in porous UO_2 was reported at least four times in experimental studies [37]. However, each investigation proposed different values for the activation energy and the pre-exponential factor. This discrepancy in the experimental data could arise from the presence of impurities or the deviation from perfect stoichiometry. Nevertheless, a correlation between the activation energy and the

pre-exponential factor of the rate constant was proposed and it was shown that the different experimental results meet such correlation [37]. That correlation simply states that, although the pre-exponential factor and activation energy differ much from one study to another, the rate constants calculated from these investigations lie within a relatively narrow range in the temperature range 1700-1800 °C. The average pore volume fraction in those investigations was between 4-6%. Therefore, one should be encouraged to compare the phase field model prediction found in the second example above with such experimental results. This comparison is depicted in Figure 4.26. This figure was produced by plotting $D^4 - D_\circ^4 = kt$, with $D_\circ = 4.7$ μm and k calculated at 1727 °C from each study. The value of the rate constant, k, calculated from the experimental data was found to lie between 977 and 1358 $\mu m^4/h$ [37]. The value predicted from the phase field model is 1132 $\mu m^4/h$. Hence the phase field model predictions lie in the middle of the empirical data, indicating good agreement with experiments.

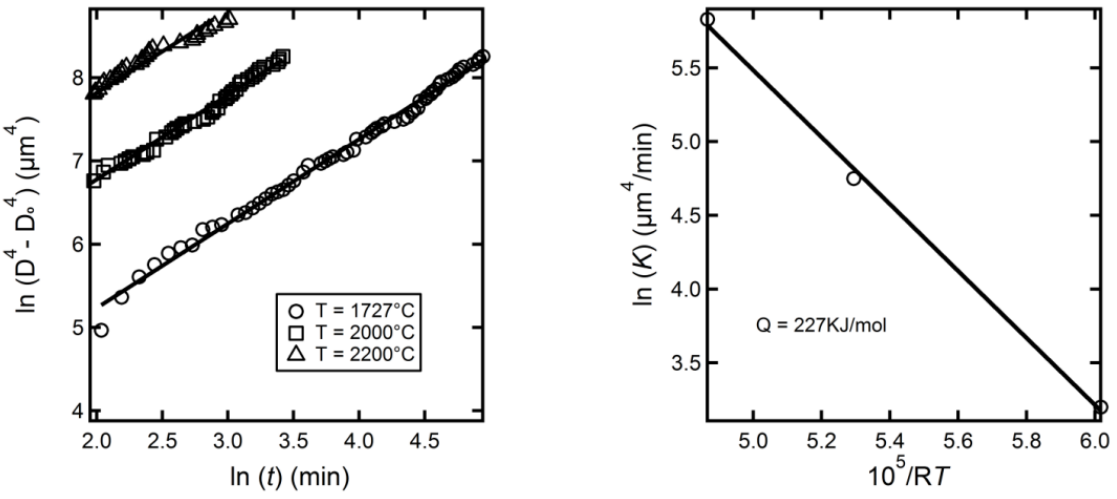

(a) (b)

Figure 4.25. Kinetics of grain growth in porous UO_2 ($f = 0.04$, $N_p = 0.4$). (a) Evolution of average grain size at different temperatures following a power law with exponent of 4, which is indicative of pore controlled growth. (b) Arrhenius plot for the rate constant showing an activation energy value of 227 KJ/mol. The markers represent the data points while the straight lines are the best fit [57].

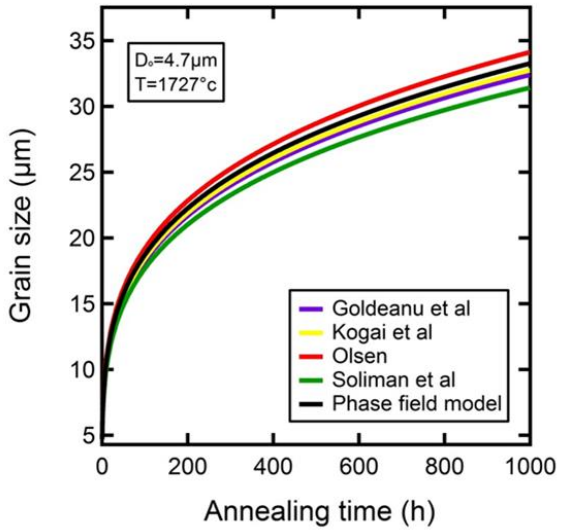

Figure 4.26. Comparison between the extrapolated phase field model prediction and the corresponding experimental results; the model predictions and experimental data were fit to the growth law: $D^4 - D_\circ^4 = kt$. Experimental data yielded a value of k in the range 977-1358 μm^4/h, while the model gave a k value of 1132 μm^4/h [57].

The above simulation cases show that the predictions of the phase field model for the kinetics of grain growth in UO_2 agree well with experimental data, both qualitatively and quantitatively. Moreover, the phase field model provides an explanation for the discrepancy in the experimental results since the precise amount of porosity seems to have a crucial effect on the grain growth kinetics in UO_2. As the amount of porosity increases, the grain growth slows down. This trend is captured in Figure 4.27, which shows the evolution of the average grain size for UO_2 with different porosity levels at1727 °C. Figure 4.27 is thus a graphical summary of all cases investigated here. The kinetics of grain growth in UO_2 changes gradually from boundary-controlled to pore-controlled kinetics with increasing the amount of porosity.

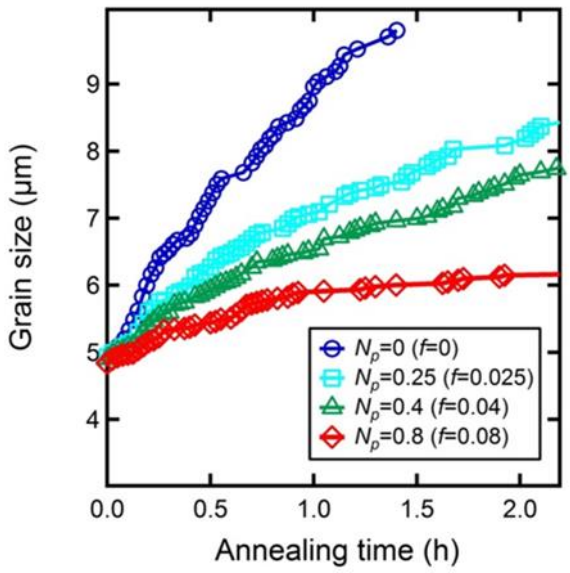

Figure 4.27. Effect of porosity on the kinetics of grain growth in UO_2 at 1727 °C. The process of grain growth retards as the amount of porosity increases [57].

The last case study considered in this section is dedicated to investigating the possibility of abnormal grain growth in porous UO_2. Abnormal grain growth refers to the

exaggerated growth of some grains relative to the normal growth for the majority of grains in a material undergoing thermal treatment at elevated temperatures. The anisotropy of grain boundary energy and mobility is considered to be the main reason for causing such abnormal growth [1]. However, the drag force experienced by the boundary due to the presence of pores, second phase particles and impurities could also lead to abnormal grain growth. A phase field model proposed by Kim et al. [124] showed that the presence of solute atoms gives rise to abnormal grain growth even in isotropic materials, i.e., when isotopic grain boundary and surface energies and mobilities were assumed to be isotropic as in the model presented here. This could be attributed to the fact that these particles tend to retard the grain growth process. Therefore, a non-uniform distribution of such particles on grain boundaries may simply cause some of the grains with fewer particles attached to them to grow much faster than the rest.

In agreement with the results obtained by Kim et al. [124], it is found that the presence of pores facilitates abnormal grain growth in porous UO_2, especially when pores are non-uniformly distributed. We used the same ensemble introduced in the second example discussed above but with pores being present only in one half of the domain. The kinetics of growth of the average grain size, in terms of the growth exponent and rate constant, remains practically the same whether the pores were uniformly or non-uniformly distributed. This is expected since the same number and size of grains and pores were used in the two cases. Nonetheless, the evolution path, i.e., the microstructure evolution, for the case of a non-uniform pore distribution is quite different from the case where the pores are distributed uniformly. This is clearly shown in Figure 4.28. Moreover,

the figure clearly demonstrates the occurrence of abnormal grain growth, as some grains grow much faster than the rest.

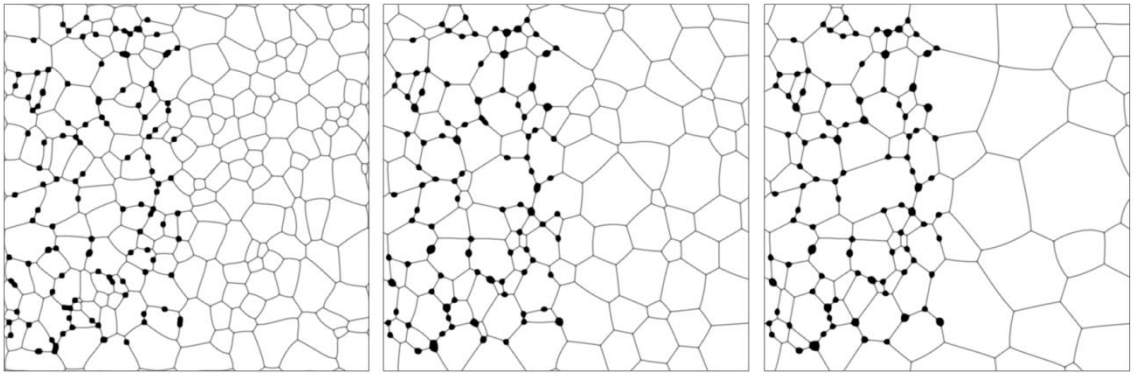

(a) *t*=1min (b) *t*=1h (c) *t*=2h

Figure 4.28. Snapshots of the microstructure evolution of porous UO_2 ($f = 0.04$, $N_p = 0.4$) at 1727 °C with non-uniform pore distribution. The grains in the pore-free part of the domain grow much faster than the grains in the porous part of the domain, giving rise to abnormal growth [57].

4.4 3D Simulations of Grain Growth in Porous Ceria

In this section, we investigate the process of grain growth in porous polycrystalline ceria using 3D simulations. In the previous section, all the results presented were for 2D solutions of the problem. The 2D solutions implicitly assume cylindrical symmetry of the pores and grains and in-plane boundary motion. Therefore, while some aspects of the underlying physics of the process were captured in the 2D solutions, 3D solutions are necessary to simulate the process of grain growth accurately and capture all the related physics. For instance, as was mentioned before in Chapter two, the phenomenon of pore breakaway is of immense importance for the sintering process [1]. However in all the 2D simulations presented here, complete pore breakaway was not observed. This is though in agreement with the analysis of Riedel and Svoboda [51, 52], which is based on the sharp-

interface modeling of the problem. As was mentioned before, they found out that 2D cylindrical pores do not separate from the grain boundary.

In applying our model to CeO_2, surface and grain boundary energies of ceria were taken to be 1.5 J/m^2 and 1.0 J/m^2, respectively [152] and orientation dependence of these energies was ignored for simplicity. The surface diffusivity of CeO_2 is given by [152]

$$D^s = 3.82\times10^{-4}\exp\left(\frac{-308250}{RT}\right)\ \mathrm{m}^2/\mathrm{s}\,. \tag{4.8}$$

The intrinsic grain boundary mobility was obtained from the experimental data by Chen and Chen [153]. Their data was chosen because their samples were pure and almost fully dense. They have deduced a value of the activation energy of 581 KJ/mole for the grain growth process. However, they did not provide a formula for the grain boundary mobility. Here, we fit their data to the expression:

$$M_b = 327.1\exp\left(\frac{-581000}{RT}\right)\ \mathrm{m}^4/\mathrm{J\ s}\,. \tag{4.9}$$

Now we turn our attention to the case of grain growth in porous ceria. As we discussed before, pores exert a drag force on the boundary that hinders its motion, and hence retards the grain growth process. However, as expected from grain growth theories and reported from experiments, there are several pore-boundary interactions that may occur. A pore may separate from the boundary or move along with it. Moreover, an isolated pore inside a grain may get picked up by a migrating boundary. Furthermore, when a pore moves along with the boundary, the kinetics of the pore-boundary complex may be pore-controlled or boundary-controlled. Therefore, a good model should be able to elucidate all these possibilities. Here we demonstrate that the phase field model is indeed capable of capturing all such scenarios.

Snapshots of the microstructure evolution in porous ceria at 1700K are shown in Figures 4.29 and 4.30 below. In this simulation, an ensemble of 100 grains with initial average grain size of 2.5 μm and 80 spherical pores with initial pore size of 0.8 μm was used. Half of the pores were distributed randomly on the grain boundary network and the rest were distributed randomly inside the grains to capture all possible pore-boundary interactions. The initially spherical pores relax quickly to a shape that satisfies locally the equilibrium dihedral angle condition at triple-junctions. Figure 4.29 presents snapshots of the 3D microstructure evolution. Figure 4.30 shows different 2D cross-sectional views of the same 3D simulation. As it is evident from the figures, there is a continuous change of the pore and boundary shapes during the migration of the pore-boundary complex. Moreover, the pore breakaway phenomenon is clearly captured. In our previous 2D simulations, the pore breakaway phenomenon was artificially suppressed due to the unrealistic cylindrical symmetry of the pores and grains implicitly assumed in 2D simulations. Such situation was also reported in the sharp-interface simulations [48-52].

In agreement with the sharp-interface predictions, the phase field model demonstrates that the pore breakaway possibility depends strongly on the pore configuration. Higher-order pore configurations, e.g., pores on three- and four-grain junctions tend to reduce to lower-order configuration before complete separation from the migrating boundary. These situations are particularly clear in Figure 4.30. The opposite scenario is also possible, i.e., migrating boundaries can attach themselves to a lower-order configuration and form a higher-order configuration; this can also be considered as a partial attachment. Moreover, a pore that started as an isolated pore inside a grain could get picked up by a migrating boundary and then separate from it and then get picked up

by another boundary and so on. Similar situation with opposite order could occur for isolated pores on grain boundaries. In another words, a specific pore could go through a series of partial and complete attachments and separations. Lastly, as can be deduced from Figures 4.29 and 4.30, most of the grains where pore separation took place are larger than their neighboring grains. This demonstrates that pore breakaway initiates abnormal grain growth as predicted from grain growth theories and reported in experiments [1, 46-58].

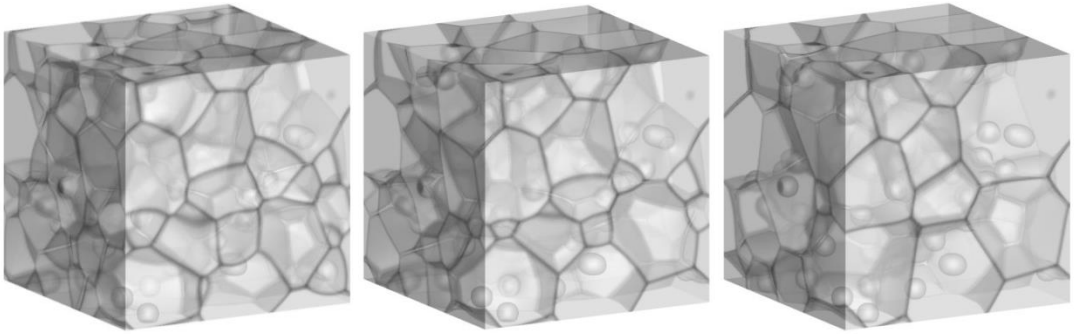

(a) (b) (c)

Figure 4.29. Snapshots of the 3D microstructure evolution in porous ceria at 1700K: (a) after 1 min, (b) at 120 min, and (c) at 360 min. Pore breakaway is evident. Some pores break away from the grain boundaries and some move along with them. The grains that left pores behind are relatively larger than the neighboring ones; this implies that pore breakaway initiates abnormal grain growth [58].

Since the 3D simulations with the current model are clearly able to account for all the possible pore-boundary interactions, it is now possible to investigate quantitatively the effects of the presence of pores on the grain growth in ceria. In doing so, we use different ensembles of grains and pores. Initially, the pores are spherical and randomly distributed on grain boundaries to mimic actual microstructures during the final stage of sintering. The initial average grain size was 2.5 μm and the pore size was 0.8 μm. The

number of pores (and hence their volume fraction, *f*) was varied to study its effect on the kinetics of grain growth.

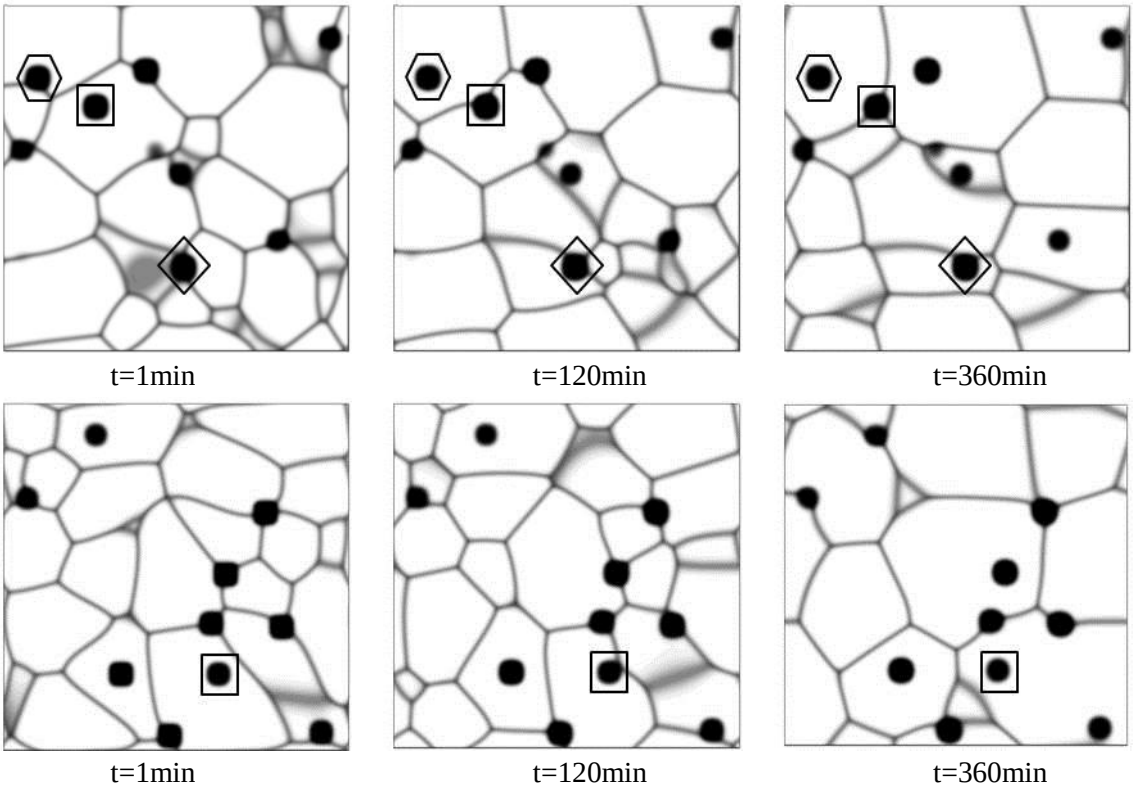

Figure 4.30. Snapshots of cross-sectional views corresponding to the results shown in Figure 4.29 revealing pore-boundary interactions: x-z plane (upper row) and y-z plane (lower row). The change of the pore shape is continuous during the movement of a pore-boundary complex. A pore can break away from or be picked up by a migrating grain boundary (e.g., the pores in hexagon and square, respectively, in the upper row). The pore breakaway possibility is highly dependent on the pore configuration. Higher-order pore configurations (e.g., the pores at three- and four-grain junctions) tend to reduce to the two-grain junction (edge pore) configuration, which represents a partial breakaway (e.g., the pore marked by diamonds in the upper row) before complete separation. A pore on a two-grain junction could also become attached to other migrating boundaries and form a higher-order configuration (e.g., the pore enclosed in squares in the upper row). A specific pore could go through a series of attachments and detachments (e.g., the pore marked by the rectangle in the lower row). The thick gray spots are due to the fact that the cutting planes are sometimes parallel to the diffuse interfaces [58].

In agreement with our previous 2D simulations, the presence of pores diminishes grain growth in porous ceria. This effect is quantitatively captured in Figure 4.31, which

shows the evolution of the average grain size with different levels of porosity at 1700K. As it is obvious from the figure, the grain growth process slows down as the amount of porosity increases. Moreover, the average kinetics of the heterogeneous system shows a transition from boundary-controlled kinetics to pore-controlled kinetics as the porosity level increases. Such situation is presented in Figure 4.32. This prediction agrees with both the classical models [46-48] and the sharp-interface models [49-52] .However, the phase field model presented here relaxes all the assumptions used in those models. For example, it does not assume a homogeneous microstructure as in the classical models [1, 46-48]. It is also not restricted to simplified geometrical descriptions of the pore/boundary configurations or steady-state situations as in the sharp-interface models [49-52]. The condition that determines which kinetics dominates is as follows. In terms of the phase field parameters, when $M_{\mathrm{s}}\kappa_{\rho} \ll f r^2 L\kappa_{\eta}$, the system follows pore-controlled kinetics, while in the case $M_{\mathrm{s}}\kappa_{\rho} \gg f r^2 L\kappa_{\eta}$, it follows boundary-controlled kinetics. Here r is the pore size. Equivalently, in terms of the regular thermodynamic and kinetic (sharp-interface) parameters, this condition becomes: if $\frac{\gamma_{\mathrm{s}} D_s w \upsilon_{\mathrm{m}}}{RT} \ll f r^2 M_b \gamma_{\mathrm{gb}}$, the growth kinetics is pore-controlled, while if $\frac{\gamma_{\mathrm{s}} D_s w \upsilon_{\mathrm{m}}}{RT} \gg f r^2 M_b \gamma_{\mathrm{gb}}$, the growth kinetics is boundary-controlled. This criterion can easily be understood if one recalls the equation of motions for the grain boundary and pore (free) surface in the diffuse- or sharp-interface descriptions (Eqs. (2.20) and (2.24) or (3.8)). Aside from the pore fraction, this condition simply examines if the grain boundary velocity is higher or lower than the pore (free) surface velocity. The pore fraction simply checks if the porosity is of significant

amount to influence the average kinetics of the system. It is also worth noting that the rate constant (or equivalently the activation energy) is sensitive to the precise amount of porosity regardless of the type of the prevailing kinetics. This is also shown in Figure 4.32 where the slope (rate constant) decreases with increasing the porosity level for both boundary- and pore-controlled kinetics. The quantitative results are summarized in Tables 1 and 2, which give the values of the rate constant as function of the pore fraction for both types of kinetics.

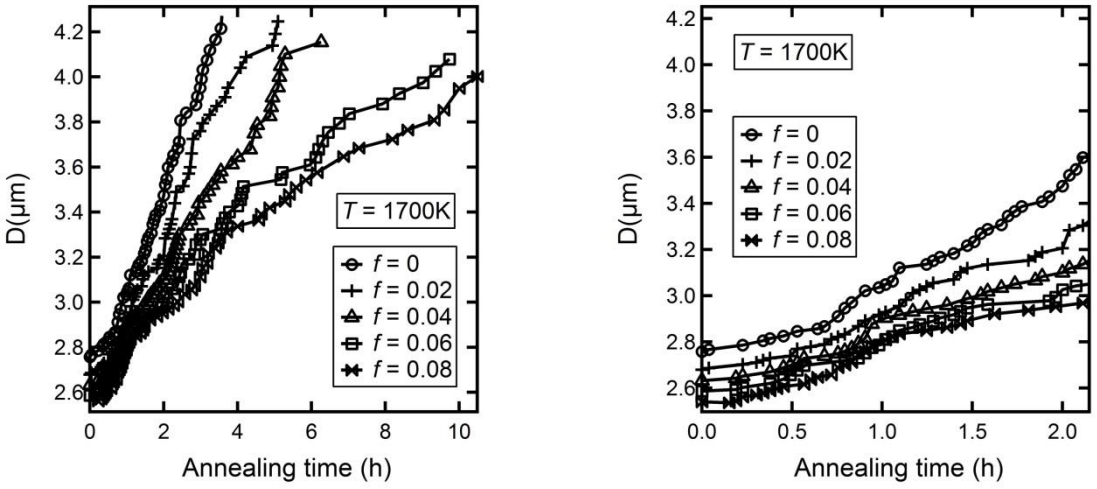

Figure 4.31. Effect of porosity on the kinetics of grain growth in CeO_2 at 1700K. (a) Evolution of the average grain size with time as function of the pore volume fraction. The main trend is the same as was captured in 2D simulations [6, 18]. That is, the process of grain growth is slowed down by increasing the amount of porosity. (b) A close up view showing the initial dense region in part (a) [58].

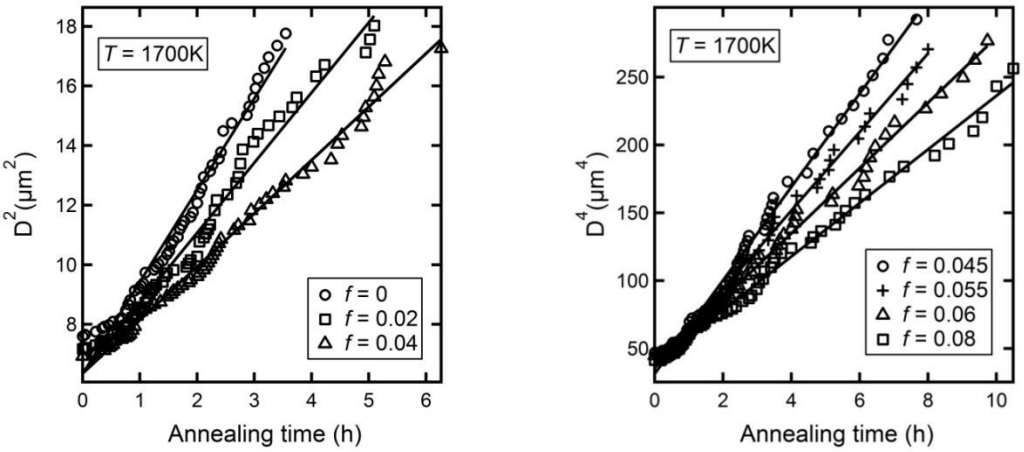

(a) Boundary-controlled growth (b) Pore-controlled growth

Figure 4.32. Kinetics of 3D grain growth in CeO_2 at 1700K at different porosity levels. There is a transition from boundary-controlled growth to pore-controlled growth as the pore fraction increases. Moreover, for each regime, the rate constant (or equivalently the activation energy) is sensitive to the precise amount of porosity. The values of the rate constant as function of porosity for both types of kinetics are given in Tables 1 and 2 [58].

Table 1: The dependence of the rate constant on the pore fraction for boundary-controlled kinetics

f (%)	$k(\mu m^2/hr)$
0	3.34
2	2.35
4	1.79

Table 2: The dependence of the rate constant on the pore fraction for pore-controlled kinetics

f (%)	$k(\mu m^4/hr)$
4.5	34.4
5.5	28.94
6	24.1
8	19.73

The strong dependence of the overall grain growth kinetics on the precise amount and distribution of pores captured by the phase field model explains the discrepancies often found in the results obtained from grain growth experiments in porous solids. For example, for the case of grain growth in ceria, different types of kinetics were reported. Chen and Chen [153] reported parabolic grain growth kinetics for highly dense ceria samples. Our model results for the boundary-controlled cases (see Figure 4.32(a)) are in good agreement with their data. Zhang and co-workers reported a growth exponent of four for Co-, Mn-, and Fe-doped porous ceria. This is similar to our results for the pore-controlled kinetics shown in Figure 4.32(b). Adding dopants is equivalent to changing the porosity level since it alters the intrinsic grain boundary mobility. In this case, as reported by Zhang and co-workers [38-40], the dopants increased the intrinsic grain boundary mobility and hence shifted the kinetics from boundary-controlled kinetics to pore-controlled kinetics.

4.5 2D and 3D Simulations of Grain Growth in Porous Solids Using MARMOT

In this section, 2D and 3D simulations of grain growth in a porous polycrystalline solid using MARMOT are presented. The main goal here is to demonstrate that the model predictions are consistent irrespective of the numerical method used to solve the model equations. Therefore, the model equations are solved here in a non-dimensionalized setting. The non-dimensionalized model parameters took on the values: $\tilde{B}=1.0$, $\tilde{C}=0.05$ $\tilde{\kappa}_{\eta}=15$, $\tilde{L}=1.0$, $\tilde{\kappa}_{\rho}=45$, and $\tilde{M}_{\mathrm{s}}=1.0$. These values of the model parameters are consistent with the magnitude of thermodynamic and kinetic parameters of most solids at high temperatures.

First, the 2D simulations are discussed. In these simulations, an ensemble of 400 grains with different number of pores was used. The domain size was 4000×4000. The initial pore radius was 60. The 400 grains were presented using only 15 orientations (order parameters) via Grain Tracker as discussed in the previous chapter. In all the simulations, adaptive mesh and time step were used. A typical adaptive mesh generated using MARMOT for simulating grain growth in porous polycrystalline solids is shown in Figure 4.33.

In common with the 2D results obtained from the explicit scheme (see Section 4.3), the 2D results obtained from the fully-coupled, fully-implicit scheme also show retardation of the grain growth process with increasing porosity. This is most evident from Figures 4.34 and 4.35. Figure 4.34 presents snapshots of the microstructure evolution of a porous polycrystalline solid with different levels of porosity. These snapshots are taken at the same time. Hence, as evident from the figure, the average grain size is smaller at higher porosity levels. This is quantitatively demonstrated in Figure 4.35 which shows the evolution of the average grain size with different pore fractions. As the pore fraction increases, the grain growth slows down. Moreover, a transition from boundary-controlled kinetics to pore-controlled kinetics takes place as the amount of porosity increases. This transition is captured in Figure 4.36. Furthermore, the absence of complete pore separation in 2D simulations is also observed here. This is most obvious in Figure 4.34 where complete pore breakaway is absent. Therefore, all the quantitative and qualitative predictions of the model that were obtained using the explicit scheme were also reproduced using the fully-coupled, fully implicit scheme implemented in MARMOT.

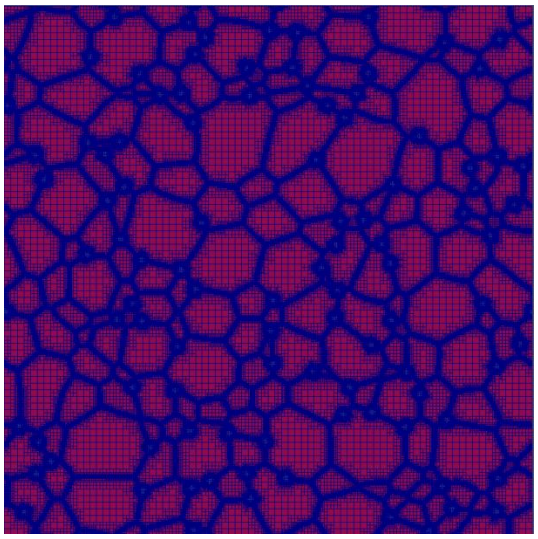

Figure 4.33. An adaptive mesh generated using MARMOT for simulating grain growth in porous polycrystalline solids. The mesh is much finer at the grain boundaries and pore surfaces than in the bulk of the grains.

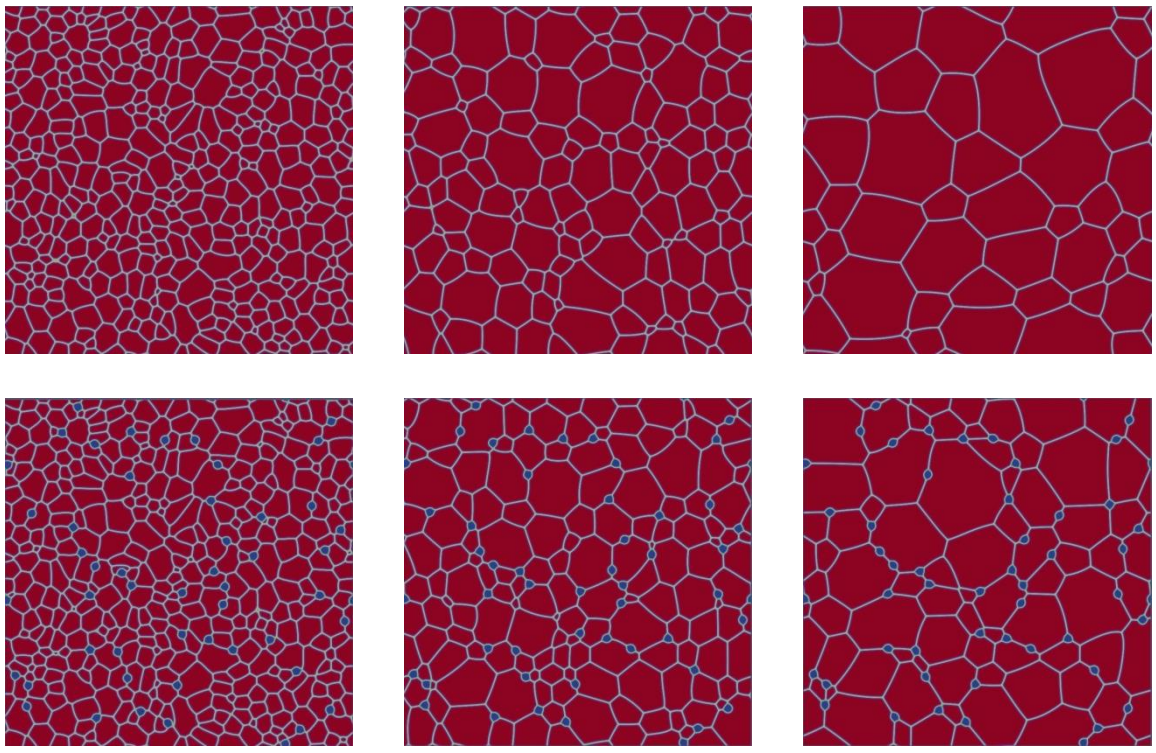

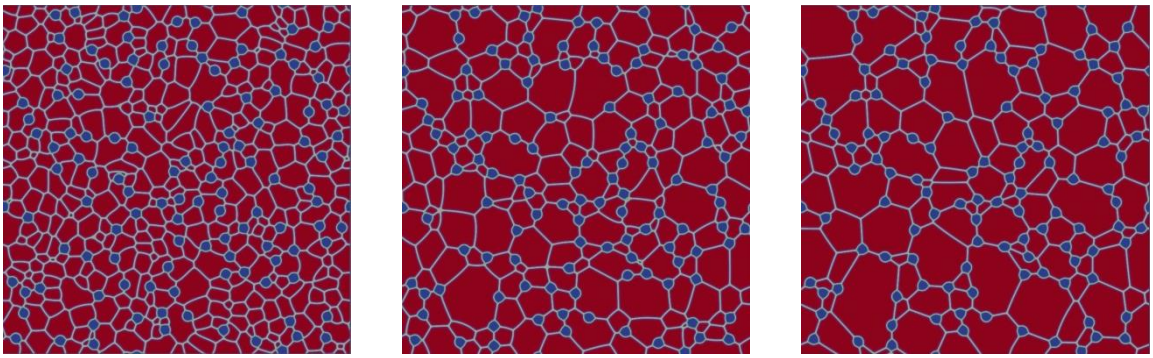

Figure 4.34. Snapshots of the microstructure evolution of a porous polycrystalline solid with different porosity levels obtained from 2D MARMOT simulations. As clear from the figure, the presence of pores diminishes the grain growth rate. This can easily be seen by noting that the average grain size is larger for lower porosity levels (the porosity level increases from top to bottom). Similar to the 2D simulations performed using the explicit scheme, complete pore separation is absent. This is due to the unrealistic assumption of cylindrical symmetry of the pore and grain shapes implied in the 2D simulation. This assumption exaggerates the contact area between the pore and the grain boundary and hence overestimates the pore drag effect.

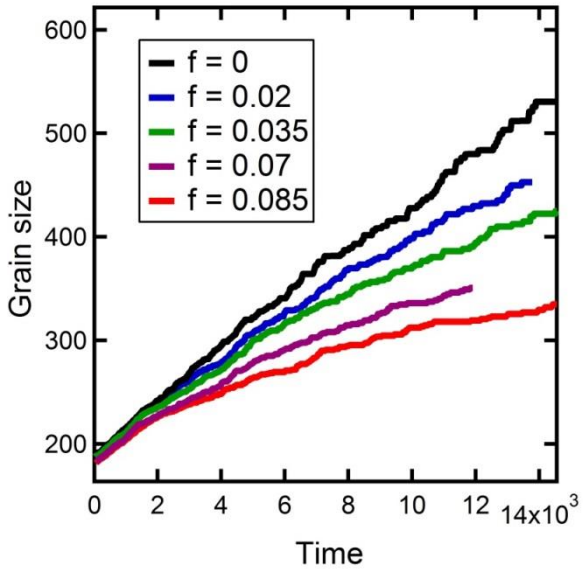

Figure 4.35. Effect of porosity on the kinetics of grain growth in a porous polycrystalline solid based on 2D MARMOT simulations (see Figure 4.34). In agreement with previous simulations performed via the explicit scheme, the growth rate diminishes as the amount of porosity increases.

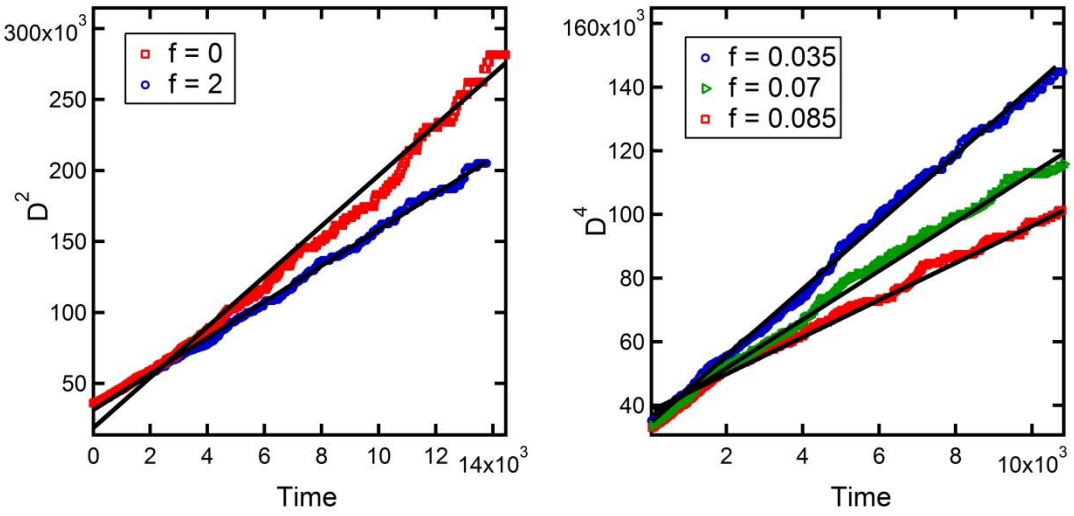

(a) Boundary-controlled growth (b) Pore-controlled growth

Figure 4.36. Dependence of the type of grain growth kinetics on the pore fraction. A transition from boundary-controlled growth to pore-controlled growth takes place as the amount of porosity increases.

3D simulations of grain growth in porous polycrystalline solids were also performed via MARMOT. The non-dimensionalized model parameters are the same as in the above 2D simulations. The domain size was $1000\times1000\times1000$. The initial pore radius was 50. An ensemble of 200 grains was used. However, the current version of Grain Tracker algorithm is inefficient in 3D. At least 50 different orientations (order parameters) had to be used to represent 200 grains. This of course leads to high computational cost since the number of degrees of freedom (DOF) is linearly proportional to the number of variables. In fact, for a typical 3D simulation with adaptive mesh, the number of elements was one million and the total number of degrees of freedom was 52 million. The 3D simulations were conducted using 600 cores on Fission cluster at Idaho National Laboratory.

Figure 4.37 shows snapshots of a 3D simulation of an ensemble of 200 grains and 200 pores. The figure clearly demonstrates that complete pore separation takes place

during grain growth in porous solids. It also shows that pore breakaway may initiate abnormal grain growth since the grains that detached from the pores are usually larger than the other grains. These deductions are also obvious in Figure 4.38 which presents different 2D cross-section views of the 3D simulation shown in Figure 4.37. Moreover, Figure 4.38 captures the fact that higher order pore configurations tend to transform into lower order configuration (partial separation) before complete separation. Hence, the 3D results obtained here using MARMOT confirm the 3D results deduced earlier via the explicit scheme (recall Section 4.4).

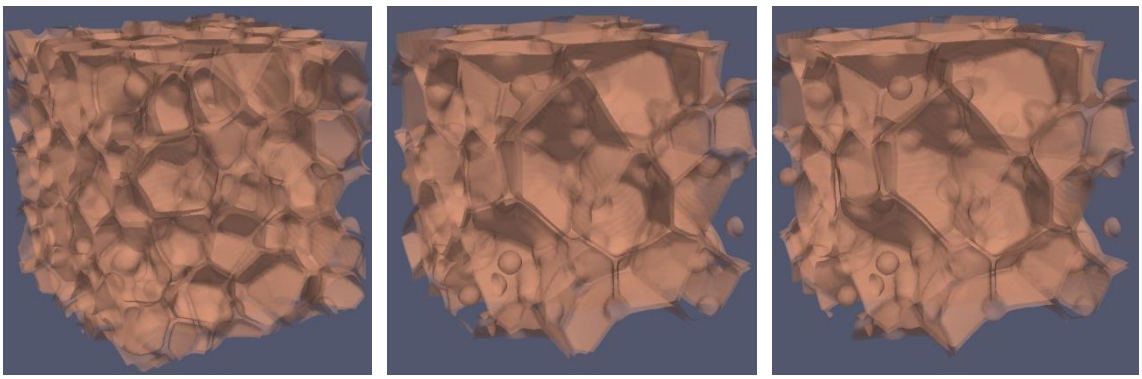

Figure 4.37. Snapshots of a 3D simulation of grain growth in a porous polycrystalline solid carried out using MARMOT. Pore breakaway is evident. This confirms that pore separation is artificially suppressed in 2D simulations as was concluded before using the explicit scheme.

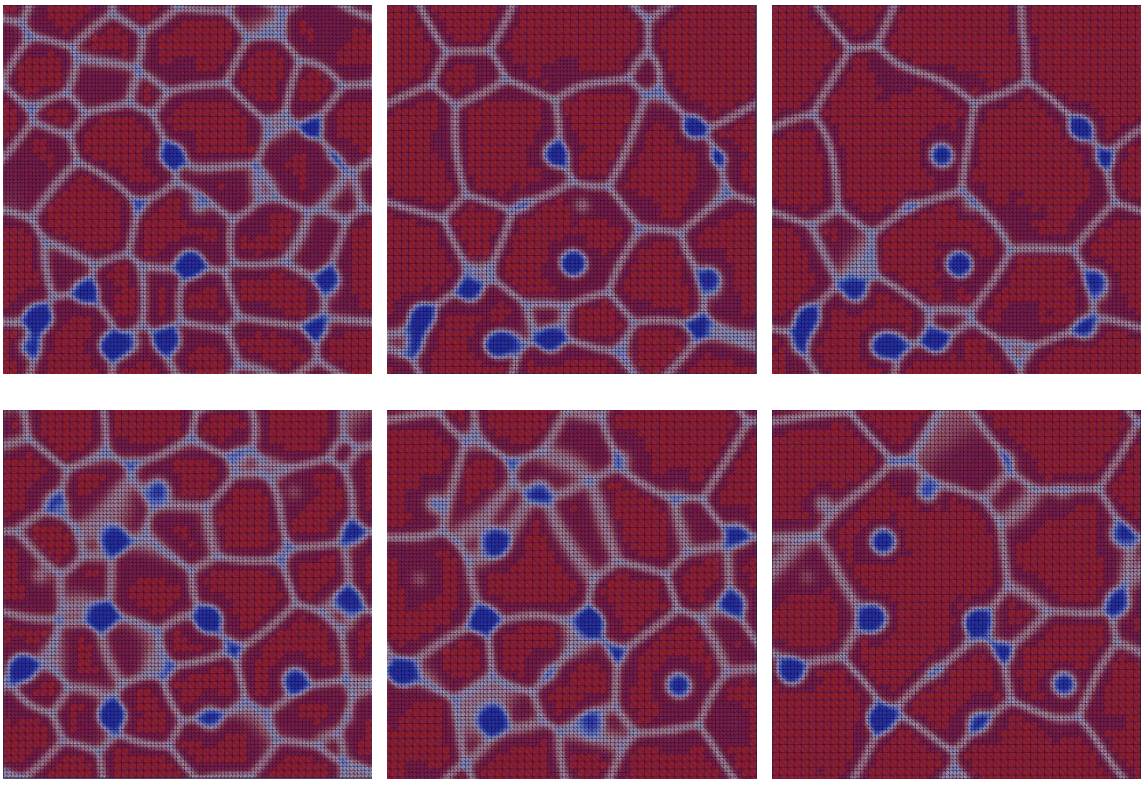

Figure 4.38. Snapshots of cross-sectional views corresponding to the 3D simulation shown in Figure 4.37 revealing pore breakaway: x-z plane (upper row) and y-z plane (lower row). Higher order pore configurations reduce to lower order configuration before complete separation. Note that the mesh is very fine in the vicinity of grain boundaries and pore surfaces.

CHAPTER 5. SUMMARY AND FUTURE DIRECTIONS

5.1 Summary

A detailed phase field model has been developed to study the kinetics of grain growth in porous polycrystalline solids. The model couples the curvature-driven grain boundary motion and pore migration by surface diffusion via constructing a dynamical system of coupled Cahn-Hilliard and Allen-Cahn equations. Hence it takes into account the interplay between the pore and the grain boundary which highly influences the overall grain growth kinetics. Moreover, the model is able to capture the concurrent pore coalescence and grain growth. We carried out a formal asymptotic analysis to demonstrate that the phase field model reduces to its sharp-interface counterpart in the limit of small diffuse-interface width. The phase field model alleviates all the unrealistic assumptions of the classical homogeneous models and obviates all the numerical difficulties of the sharp-interface models. All the model parameters were identified in terms of regular thermodynamic and kinetic parameters. The free energy parameters of the model are directly related to the surface and grain boundary energies, Cahn-Hilliard and Allen-Cahn mobilities are given in terms of the surface and grain boundary mobilities. Determination of the model parameters enables quantitative analysis of the grain growth process. The model equations were solved using two different numerical schemes, e.g., explicit and implicit. The explicit scheme uses finite-difference

discretization and was implemented using in-house codes written in FORTRAN 90. The fully-coupled, fully-implicit scheme uses finite-element discretization with adaptive meshes and was implemented using MARMOT. The kinetic trends captured by the model using the two techniques were the same, which raises the confidence in the numerical results. The high computational cost was overcome by using parallel computing. The 3D simulations presented here are the first such general simulations for 3D grain growth in porous polycrystalline solids in the literature.

The model has been used to investigate the effect of porosity on the kinetics of grain growth in porous polycrystalline solids. By using idealized 2D pore and grain shapes, the basic pore-grain boundary interactions were captured. It was shown that the presence of pores exerts a drag on the grain boundary hindering its motion and retarding the grain growth process. As the amount of porosity increases, the growth rate diminishes. Moreover, higher pore (free) surface mobility leads to faster grain growth. This is due to the fact that pores with high surface mobility are easier to be dragged by the migrating boundary, i.e., they exert less drag on the grain boundary. In fact, for high enough surface mobility, the pore moves along with the boundary as a rigid-body without changing its shape or size. Moreover, it was shown that the pore configuration influences the grain growth kinetics in porous solids. The simulations demonstrated that corner pores (pores on triple-junctions) retard the grain growth process more than edge pores (pores on two-grain junctions). This can be attributed to the fact that edge pores have higher curvature and hence higher velocity than corner pores. Obviously, the more mobile edge pores exert less retarding force on the grain boundary than corner pores. This result can be generalized to higher-order pore configuration as well. The higher the pore coordination

number (the number of grains attached to the pore) is, the lower its curvature and hence velocity. Therefore, higher-order pore configurations retard the grain growth process more than lower order configuration. Furthermore, it was shown that when the kinetic mechanism of bulk diffusion is active, corner pores grow at the expense of edge pores as part of Ostwald ripening of the pores during coarsening. Hence, the process of Ostwald ripening of the pores tends to hinder the grain growth process since it transform the more mobile lower-order pore configurations into less mobile higher-order pore configurations.

The model was then applied to investigate the effect of porosity on the kinetics of grain growth in UO_2 and CeO_2. The model parameters for both materials were calculated from their thermodynamic and kinetic data available in literature. 2D and 3D simulations were performed to study in details the grain growth process in these materials. The polycrystalline structures were produced using a Voronoi tessellation. It was demonstrated that the presence of pores slows down the grain growth process. Moreover, it was shown that the growth mode is very sensitive to the amount of porosity. As the amount of porosity increases, the growth mode changes from boundary-controlled to pore-controlled. In each growth mode, the rate constant (or equivalently the activation energy) depends strongly on the pore fraction. Only 3D simulations were able to capture the phenomenon in pore breakaway, which is commonly observed in experiments. This shows that 2D simulations artificially suppress the process of pore separation. The 3D simulations revealed that higher-order pore configurations transform into lower-order configurations before complete separation. Such transformation may be called partial breakaway. On the other hand, partial attachments where lower-order pore configurations transform into higher-order pore configurations also take place during grain growth in

porous polycrystalline solids. Lastly, it was observed that inhomogeneous pore distribution and pore breakaway lead to abnormal grain growth. Therefore, a detailed description of the microstructure (e.g., pore fraction and pore and grain sizes and distributions) is necessary for obtaining accurate grain growth rates. The strong dependence of the grain growth kinetics on the underlying microstructure in porous polycrystalline solids captured by the phase field model helps in reconciling the discrepancies found in the experimental results for such materials [1, 36-40, 153].

5.2 Future Directions

The possible directions for future research are the following:

- In our investigation, we considered surface diffusion to be the sole mechanism for pore migration. However, for a complete description of the problem, bulk diffusion and evaporation and condensation must be incorporated as possible mechanisms for pore migration. Note that bulk diffusion was already considered during the investigation of Ostwald ripening of pores in Section 4.2. It can be shown that only minor modifications are required for the current version of the model to account for evaporation and condensation.
- In all the simulations presented here, isotropic material properties, e.g., surface and grain boundary energies and mobilities were assumed. For a more accurate description of grain growth in real materials, the anisotropy of these parameters must be taken into account. Such anisotropy is known to cause abnormal grain growth in fully dense solids. For the case of porous materials, it will certainly also affect the possibility of pore breakaway and hence the overall growth kinetics. The current version of the phase field model can be generalized to take into

consideration the anisotropy of these parameters by allowing the gradient coefficients, Cahn-Hilliard mobility, and Allen-Cahn mobility to depend on the corresponding order parameters and/or their gradients. A detailed procedure for constructing such anisotropic phase field models was reported several times in the literature [59-61].

- The current model ignores the effect of deviation from perfect stoichiometry on the kinetics of grain growth in ceramics. Deviations from stoichiometric concentrations are known to affect all the thermodynamic and kinetic parameters of ceramics and hence their grain growth kinetics [36-40, 150, and 151]. Nonetheless, this effect can be incorporated into the model if one can establish direct relations between deviations from stoichiometric concentrations and the thermodynamic and kinetic parameters. This could be achieved through experiments or lower scale models such molecular dynamics and density functional theory.
- While the model presented here was used to investigate grain growth in porous UO_2, the effect of irradiation was absent. Irradiation is known to drive microstructure evolution and affect the grain growth kinetics in UO_2 [36, 37, 150, 151, and 154-156]. Two steps are required to incorporate irradiation effects in the current version of the model. The first step is to reformulate the model in terms of point defects rather than mass density. In the second step, generalized Cahn-Hilliard equations for the point defect concentrations including production and reaction terms can be derived as in the case for the phase field models for void growth [62, 101-112]. However, in order for such models to be quantitative,

formal asymptotic analyses must be performed to deduce their sharp-interface limits and connect their parameters to the regular thermodynamic and kinetic parameters. We have, in fact, taken the first step for constructing such general models by developing phase field models for porosity evolution in single crystals under irradiation [62, 154].

LIST OF REFERENCES

LIST OF REFERENCES

[1] Rahaman M N. Ceramic Processing and Sintering. New York: Marcel Dekker; 2003.

[2] Kingery W D, Bowen H K, Uhlmann D R. Introduction to Ceramics. New York: Wiley; 1976.

[3] Burke JE, Turnbull D. Prog Metal Phys 1952; 3: 220.

[4] Mullins W. J Appl Phys 1956; 27: 900.

[5] Hillert M. Acta Metall 1965; 13: 227.

[6] Armstrong RW. Met Trans 1970; 1: 1169.

[7] Turnbull JA. J Nucl Mater 1974; 50: 62.

[8] Lifshitz IM, Slyozov VV. J Phys Chem Solids 1961;19:35.

[9] Wagner CZ. Electrochem 1961;65:581.

[10] Tonks M, Zhanga Y, Bai X, Millett P. Mater Res Lett 2014; 2:23.

[11] Tonks M, Millett P, Cai W, Wolf D. Scr Mater. 2010; 63:1049.

[12] Gottstein G, Shvindlerman L. Grain Boundary Migration in Metals: Thermodynamics, Kinetics, Applications. Boca Raton (FL): CRC Press; 1999.

[13] Cahn JW, Taylor JE. Acta Mater 2004; 52:4887

[14] Upmanyu M, Srolovitz D, Lobkovsky A, Warren J, Carter W. Acta Mater 2006; 54:1707.

[15] Gorkaya T, Molodov K, Molodov D, Gottstein G. Acta Mater 2011; 59:5674

[16] Moldovan D, Wolf D, Phillpot SR. Acta Mater 2001;49:3521.

[17] Rodney D, LeBouar Y. Acta Mater 2003;51:17.

[18] Srolovitz DJ, Anderson MP, Shan PS, Grest GS. Acta Metall 1984; 32: 793.

[19] Saito Y. Mater Sci Eng A 1997; 223: 114.

[20] Xiaoyan S, Guoquan L, Nanju. Scripta Mater 2000; 43: 355.

[21] Wang C and Lui G. Mater Lett 2003; 57: 4424.

[22] Frost HG, Thompson CV, Howe CL, Whang J. Scripta Metall 1988; 22: 65.

[23] Fayad W, Thompson CV, Frost HG. Scripta Metall 1999; 40: 1199.

[24] Gill SP, Cocks CF. Acta Mater 1996; 44: 4777.

[25] Cleri F. Physica A 2000; 282: 339.

[26] Moldovan D, Wolf D, Phillpot SR, Haslam AJ. Acta Mater 2002; 50: 3397.

[27] Moldovan D, Wolf D, Phillpot SR, Haslam AJ. Phil Mag A 2002; 82: 1271.

[28] Fuchizaki K, Kawasaki K Physica A. 1995; 221: 202.

[29] Liu Y, Baudin T, Penelle R. Scripta Mater 1996; 34: 1679.

[30] Geiger J, Roosz A, Barkoczy P. Acta Mater 2000; 49: 623.

[31] Chen LQ, Yang W. Phys Rev B 1994; 50: 15752.

[32] Fan D, Geng C, Chen LQ. Acta Mater 1997; 45: 1115.

[33] Kazaryan A, Wang Y, Dregia SA, Patton BR. Phys Rev B 2001; 63: 184102.

[34] Kazaryan A, Wang Y, Dregia SA, Patton BR. Acta Mater 2002; 50: 2491.

[35] Kazaryan A, Patton BR, Dregia SA, Wang Y. Acta Mater 2002; 50: 499.

[36] Ainscough JB, Oldfield BW, Ware JO. J Nucl Mater 1973;49:117.

[37] Bourgeois L, Dehaudt P, Lemaignan C, Fredric JP. J Nucl Mater 2001;295:73.

[38] Zhang TS, Hing P, Huang H, Kilner J. J Eur Ceram Soc 2002; 22: 27.

[39] Zhang TS, Hing P, Huang H, Kilner J. Mater. Lett 2002;57:507

[40] Zhang TS, Ma J, Kong LB, Zeng ZQ, Hing P, Kilner J. Mat Sci Eng B 2003; 103:177.

[41] C. Smith. Trans. AIME. 1948;175:15.

[42] Doherty RD, Srolovitz DJ, Rollett A D, Anderson M P. Scripta Metall 1987; 21: 675.

[43] Anderson MP, Grest GS, Doherty RD, Li K, Srolovitz DJ. Scripta Metall 1989; 23: 753.

[44] Fan D, Chen LQ, Chen SP. J Am Ceram Soc 1998; 81: 526.

[45] Tonks M, Zhanga Y, Butterfield A, Bai X. Modell Simul Mater Sci Eng 2015;23:045009.

[46] Nichols FA. J Am Ceram Soc 1968;51:468.

[47] Brook RJ. J Am Ceram Soc 1969;52:56.

[48] Carpay FM. J Am Ceram Soc 1977;60:82.

[49] Hsueh CH, Evans AG, Coble RL. Acta Metall 1982; 30: 1269.

[50] Spears MA, Evans AG. Acta Metall 1982; 30: 1281.

[51] Svoboda J, Riedel H. Acta Metall Mater 1992; 40: 2829.

[52] Riedel H, Svoboda J. Acta Metall Mater 1993; 41: 1929.

[53] Hartland P, Crocker AG. J Nucl Mater 1988; 152: 310.

[54] Liu Y, Patterson BR. Acta Metall Mater 1993; 41: 2651.

[55] Klinger L, Rabkin E, Shvindlerman L, Gottstein G. J Mater Sci 2008; 43: 5068.

[56] Ahmed K, Yablinsky CA, Schulte A, Allen T, El-Azab A. Modell Simul Mater Sci Eng 2013;21:065005.

[57] Ahmed K, Pakarinen J, Allen T, El-Azab A. J Nucl Mater 2014; 446: 90.

[58] Ahmed K, Allen T, El-Azab A. "phase field modeling for grain growth in porous solids" Journal of Materials Science (2015) DOI 10.1007/s10853-015-9107-9 .

[59] Emmerich H. The Diffuse Interface Approach in Materials Science: Thermodynamic Concepts and Applications of Phase-Field Models. Berlin: Springer; 2003.

[60] Emmerich H. Adv Phys 2008;57:1.

[61] Provatas N, Elder K. Phase-Field Methods in Materials Science and Engineering. Weinheim: Wily-VCH; 2010.

[62] El-Azab A, Ahmed K, Rokkam S, Hochrainer T. Curr Opin Solid State Mater Sci 2014; 18: 90.

[63] Slattery JC, Sagis L, Oh ES. Interfacial Transport Phenomena. New York: Springer-Verlag; 2007

[64] Balluffi RW, Allen SM, Carter WC. Kinetics of Materials. New Jersey: John Wiley and Sons Inc; 2005.

[65] Taylor JE and Cahn JW. J Stat Phys 1994; 77:183.

[66] Mullins W. J Appl Phys 1956; 28: 333.

[67] Barrett JW, Garcke H, Nurnberg R. Euro Jnl of Applied Mathematics 2010; 21: 519.

[68] Boettinger WJ, Warren JA, Beckermann C, Karma A. Ann Rev Mater Res 2002;23163.

[69] Wang Y, Khachaturyan AG. Mater Sci Eng A 2006;438-440:55.

[70] Chen LQ, Yang W. Phys Rev B 1994;50:15752.

[71] Moelans N, Blanpain B, Wollants P. Phys Rev B 2008;78:024113.

[72] Henry H, Levine H. Phys Rev Lett 2004;93:105504.

[73] Rodney D, LeBouar Y. Acta Mater 2003;51:17.

[74] Wang Y, Liu Y. J Am Ceram Soc 2000;83:2219.

[75] Asp K, Agren J. Acta Mater 2006;54:1241.

[76] Wang Y. Acta Mater 2006;54:953.

[77] Mahadevan M, Bradley R. Physica D 1999;126:201.

[78] Bhate D, Kumar A, Bower A. J Appl Phys 2000;87:1712.

[79] Biben T, Kassner K, Misbah C. Phys Rev E 2005;72:041921.

[80] Rowlinson JS. J Stat Phys 1979;20:197.

[81] Landau LD, Khalatikov IM. The Selected Works of LD Landau. Oxford: Pregamon; 1963.

[82] Ginzburg VL, Landau LD. Sov Phys JETP 1950;20:1064.

[83] Cahn JW, Hilliard JE. J Chem Phys 1958;28:258.

[84] Cahn JW, Hilliard JE. J Chem Phys 1959;30:1121.

[85] Cahn JW, Hilliard JE. J Chem Phys 1959;31:688.

[86] Moelans N, Blanpain B, Wollants P. Calphad 2008; 32: 268.

[87] Chen LQ. Ann Rev Mater Res 2002;32:113.

[88] Steinbach I. Modell Simul Mater Sci Eng 2009; 17: 073001.

[89] Khachaturyan AG. Theory of structural transformations in solids. New York: John Wiley and Sons; 1983.

[90] Rokkam S. Phase Field Modeling of Void Nucleation and Growth in Irradiated Materials, Ph.D. Dissertation, Florida State University, 2011.

[91] Bi Z, Sekerka RF. Physica A 1998; 261: 95.

[92] De Groot SR, Mazur P. Non-Equilibrium Thermodynamics. Amsterdam: North-Holland Publishing Company;1962.

[93] J. Keizer Statistical Thermodynamics of Nonequilibrium Processes. New York: Springer-Verlag; 1987.

[94] I. Prigogine. Introduction to Thermodynamics of Irreversible Processes. New York: John Wiley and Sons; 1967.

[95] Y. Demirel. Nonequilibrium Thermodynamics - Transport and Rate Processes in Physical, Chemical and Biological Systems. Elsevier Science and Technology Books; 2007.

[96] Hohenberg P C, Halperin B I. Rev Mod Phys 1977; 49: 435.

[97] Glauber R J. J Math Phys 1963; 4: 294.

[98] Kawasaki K. Phys Rev 1966; 145: 224.

[99] Allen SM, Cahn JW. Acta Metall 1979; 27: 1085.

[100] Cahn JW. Acta Metall 1961; 9: 795.

[101] Yu H-C, Lu W. Acta Mater 2005;53:1799.

[102] Hu S, Henager CH, Heinisch HL, Stan M, Baskes MI, Valone SM. J Nucl Mater 2009;392:292.

[103] Hu S, Henager CH. J Nucl Mater 2009;394:155.

[104] Hu S, Henager CH. Acta Mater 2010;58:3230.

[105] Li Y, Hu S, Sun X, Gao F, Henager CH, Khaleel M. J Nucl Mater 2010;407:119.

[106] Semenov A, Woo C. Acta Mater 2012;60:6112.

[107] Rokkam S, El-Azab A, Millett P, Wolf D. Mod Sim Mater Sci Eng 2009;17:064002.

[108] Millett PC, Rokkam S, El-Azab A, Tonks M, Wolf D. Mod Sim Mater Sci Eng 2009;17:064003.

[109] Millett PC, El-Azab A, Wolf D. Comp Mater Sci 2011;50:960–70.

[110] Millett PC, El-Azab A, Rokkam S, Tonks M, Wolf D. Comp Mater Sci 2011;50:949–59.

[111] Li Y, Hu S, Montgomery R, Gao F, Sun X. Nucl Instr Meth in Phys Res B 2013;303:62.

[112] Millet PC, Tonks Michael. Curr Opin Solid State Mater Sci 2011;15:125.

[113] Pego RL. Proc Roy Soc London Ser **A** 1989; 422: 261.

[114] Dai S, Du Q. SIAM Appl Math 2012; 72: 1818.

[115] Elder K, Grant M, Provatas N, Kosterlitz J. Phys Rev E 2001; 64:021604.

[116] Fife PC, Dynamics of Internal Layers and Diffuse Interfaces. Philadelphia: SIAM; 1992.

[117] Garcke H, Nestler B, Stinner B. SIAM Appl Math 2004; 64: 775.

[118] C. Gugenberger, R. Spatschek, and K. Kassner, Phys. Rev. E **78**, 016703 (2008).

[119] Caginalp G. Phys Rev A 1989; 39: 5887.

[120] http://www.openphase.de/

[121] http://mooseframework.org/

[122] Gastona D, Newmana C, Hansena G, Lebrun-Grandieb D. Nucl Eng Des 2009; 239: 1768.

[123] Tonks M, Gaston D, Millett P, Andrs D, Talbot P. Comp Mater Sci 2012; 51: 20.

[124] Kim SG, Park YB. Acta Mater 2008;56: 3739.

[125] Cahn JW, Novic-Cohen A. Acta Mater 2000;48: 3425.

[126] Moelans N, Blanpain B, Wollants P. Acta Mater 2006; 54: 1175.

[127] Moelans N, Blanpain B, Wollants P. Acta Mater 2007; 55: 2173.

[128] http://libmesh.github.io/

[129] http://www.mcs.anl.gov/petsc/

[130] Chan PK, Rey AD. Comp Mater Sci 1995; 3: 377.

[131] M. Tonks, D. Gaston, P. Millett, D. Andrs, and P. Talbot. J Comp Phys 2013; 236: 74.

[132] Knoll D, Keyes D. J Comp Phys 2004; 193: 357.

[133] Saad Y, Schultz MH. SIAM J Sci Statist Comput 1986; 7: 856.

[134] Suwa Y, Saito Y, Onodera H. Scr Mater 2006; 55: 407.

[135] Krill CE, Chen LQ. Acta Mater. 2002; 50: 3057.

[136] Kim SG, Kim DI, Kim WT, Park Y. Phys Rev E 2006; 74: 061605.

[137] Steinbach I, Pezzolla F. Physica D 1999; 134: 385.

[138] Kim SG, Kim WT, Suzuki T, Ode M. J Cryst Growth 2004; 26: 135.

[139] Chen LQ, Ma N, Wu K, Wang Y. Scripta Mater 2004; 50: 471

[140] Shen C, Chen LQ, Wen YH, Simmons JP, Wang Y. Scripta Mater 2004; 50: 1023.

[141] Shen C, Chen LQ, Wen YH, Simmons JP, Wang Y. Scripta Mater 2004; 50: 1029.

[142] Mullins W. J Appl Phys 1959; 30: 77.

[143] Mullins W, Shewmon PG. Acta Metall 1959; 7: 163

[144] Nichols FA, Mullins W. J Appl Phys 1965; 36: 1826.

[145] Cahn JW, Taylor J E. Acta Metall Mater 1994; 42: 1045.

[146] Lord Rayleigh. Proc London Math Soc 1878; 10: 4.

[147] Coble RL. J Appl Phys 1961; 32: 787.

[148] Nichols FA. J Mater Sci 1976; 11: 1077.

[149] Gupta TK. J Am Ceram Soc 1978;61:191.

[150] Reynolds GL, Burton B. J Nucl Mater 1979; 82: 22.

[151] Maiya PS. J Nucl Mater 1971; 40: 57.

[152] Zouvelou N, Mantzouris X, Nikolopoulos P. Mat Sci Eng A 2008 ; 495 :54

[153] Chen P, Chen I. J Am Ceram Soc 1996; 79: 1793.

[154] Ahmed K, El-Azab A. "On two classes of phase field models for void growth and coarsening in irradiated crystalline solids" submitted to Physical Review E.

[155] Olander DR. Fundamental Aspects of Nuclear Reactor Fuel Element. Washington DC: US DOE; 1976.

[156] Was GS. Fundamentals of Radiation Materials Science. Berlin: Springer; 2007.

[157] Novic-Cohen A. Physica D 2000; 137: 1.

[158] Barrett JW, Garcke H, Nurnberg R. Interfaces Free Bound 2007; 9:171.

[159] Ahmed K. Phase Field Modeling of Microstructure Evolution in Thermal Barrier Coating Systems, M.SC. Thesis, Florida State University, 2011.

APPENDICES

Appendix A Determination of Model Energetic Parameters

Here, we use the equilibrium solutions of phase field variables to fix the model parameters. We perform this task in two steps. First we study the phase field profiles across a flat grain boundary between two semi-infinite different grains with orientations *i* and *j* (see Figure A1(a)). Across a grain boundary, the change in the density field is very small, $\rho \approx 1$, and can be neglected. By following Cahn and Hilliard approach [83], the specific grain boundary energy, γ^{gb}, is given by the integral

$$\gamma^{\mathrm{gb}} = \int_{-\infty}^{+\infty} f(\rho = 1, \eta_i, \eta_j) + \frac{\kappa_\eta}{2}\left[\left(\frac{\mathrm{d}\eta_i}{\mathrm{d}x}\right)^2 + \left(\frac{\mathrm{d}\eta_j}{\mathrm{d}x}\right)^2\right] \mathrm{d}x, \tag{A.1}$$

where an isotropic grain boundary energy was assumed. This assumption leads to only one gradient coefficient. Here, *x* is the coordinate perpendicular to the grain boundary, and $f(\rho = 1, \eta_i, \eta_j)$ is the bulk free energy density (see Eq. (3.2)) at the grain boundary between grain *i* and grain *j*, which reads as follows:

$$f(\rho = 1, \eta_i, \eta_j) = C\left[1 - 4\left(\eta_i^3 + \eta_j^3\right) + 3\left(\eta_i^2 + \eta_j^2\right)^2\right]. \tag{A.2}$$

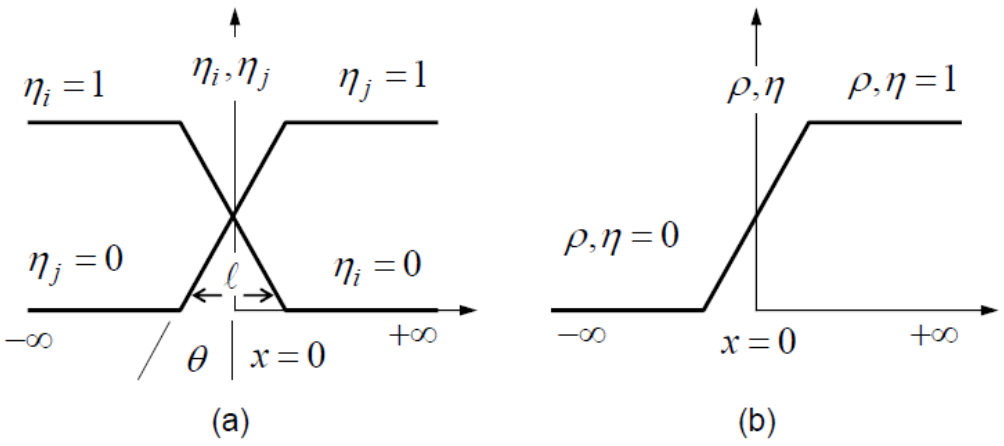

Figure A1**.** A schematic of the variation of phase field variables across (a) a diffuse flat grain boundary and (b) a diffuse flat surface.

For a grain boundary in local equilibrium, the profiles $\eta_i(x)$ and $\eta_j(x)$ must adopt a shape which minimizes the functional (A.1) and satisfies the following boundary conditions (see Figure A1(a)):

$$\eta_i = 1 \quad \text{and} \quad \eta_j = 0 \quad \text{for } x \to -\infty, \tag{A.3a}$$

$$\eta_i = 0 \quad \text{and} \quad \eta_j = 1 \quad \text{for } x \to +\infty, \tag{A.3b}$$

$$\frac{d\eta_i}{dx} = \frac{d\eta_j}{dx} = 0 \quad \text{for } x \to \pm\infty. \tag{A.3c}$$

According to the principles of calculus of variations, the functions $\eta_i(x)$ and $\eta_j(x)$ that extremize the functional (A.1) must satisfy Euler equations, namely,

$$\frac{\partial f(\rho = 1, \eta_i, \eta_j)}{\partial \eta_i} - \kappa_\eta \frac{d^2\eta_i}{dx^2} = 0, \tag{A.4a}$$

$$\frac{\partial f\left(\rho = 1, \eta_i, \eta_j\right)}{\partial \eta_j} - \kappa_\eta \frac{d^2\eta_j}{dx^2} = 0. \tag{A.4b}$$

Equivalently, these profiles satisfy

$$f(\rho=1,\eta_i,\eta_j)-\frac{\kappa_\eta}{2}\left[\left(\frac{\mathrm{d}\eta_i}{\mathrm{d}x}\right)^2+\left(\frac{\mathrm{d}\eta_j}{\mathrm{d}x}\right)^2\right]=0, \tag{A.5}$$

where the boundary conditions (A.3) were taken into account. Across a flat grain boundary, the following relation holds (see Figure A1(a)):

$$\frac{\mathrm{d}\eta_j}{\mathrm{d}x}\propto-\frac{\mathrm{d}\eta_i}{\mathrm{d}x}, \tag{A.6}$$

by integrating the above equation taking into account the boundary conditions, we simply obtain

$$\eta_j(x)=1-\eta_i(x), \tag{A.7}$$

which is readily seen from figure A1(a). This immediately modifies equation (A.6) to

$$\frac{\mathrm{d}\eta_j}{\mathrm{d}x}=-\frac{\mathrm{d}\eta_i}{\mathrm{d}x}, \tag{A.8}$$

which also gives

$$\frac{\mathrm{d}\eta_j}{\mathrm{d}\eta_i}=-1. \tag{A.9}$$

Rearranging equation (A.5) while taking into account equations (A.7) through (A.9) and the boundary conditions, we obtain

$$\frac{\mathrm{d}\eta_i}{\mathrm{d}x}=-\sqrt{\frac{f(\rho=1,\eta_i,\eta_j)}{\kappa_\eta}}, \tag{A.10}$$

$$\frac{\mathrm{d}\eta_j}{\mathrm{d}x}=\sqrt{\frac{f(\rho=1,\eta_i,\eta_j)}{\kappa_\eta}}. \tag{A.11}$$

The above two equations are needed to carry out the integral in (A.12), which comes by substituting equation (A.5) into equation (A.1).

$$\gamma^{gb} = \int_{-\infty}^{+\infty} 2 f(\rho = 1, \eta_i, \eta_j)\, \mathrm{d}x . \tag{A.12}$$

From equation (A.7) we have $\eta_j(x) = 1 - \eta_i(x)$, so by substituting this relation into equation (A.2) and skipping some algebraic details we obtain

$$f(\rho = 1, \eta_i, \eta_j = 1 - \eta_i) = f(\eta_i) = 12 C \eta_i^2 (1 - \eta_i)^2 . \tag{A.13}$$

Substituting by equation (A.10) and equation (A.13) into equation (A.12) gives,

$$\gamma^{gb} = 2\sqrt{12 C \kappa_\eta} \int_0^1 \eta_i (1 - \eta_i)\, \mathrm{d}\eta_i = \frac{2}{\sqrt{3}} \sqrt{C \kappa_\eta} . \tag{A.14}$$

Equation (A.14) establishes a direct relation between two of the model parameters and a material property which is the specific grain boundary energy.

The diffuse interface width across a flat grain boundary can be estimated from the model parameters by (see Figure A1(a))

$$\left(\frac{\mathrm{d}\eta_j}{\mathrm{d}x} \right)_{x=0} = \tan\theta = \frac{1}{\ell} . \tag{A.15}$$

From equations (A.11) and (A.13) and Figure A1(a), we have

$$\left(\frac{\mathrm{d}\eta_j}{\mathrm{d}x} \right)_{x=0} = \sqrt{\frac{f(\eta_i = 0.5)}{\kappa_\eta}} = \sqrt{\frac{3C}{4\kappa_\eta}} , \tag{A.16}$$

The last two relationships yield

$$\ell = \sqrt{\frac{4\kappa_\eta}{3C}} = \delta , \tag{A.17}$$

where δ is the grain boundary thickness. Equation (A.17) provides a relation between the model parameters and another material property which is the grain boundary thickness.

There are still two parameters in the free energy functional to be determined, B and κ_ρ. These parameters can be obtained from the phase field profiles in equilibrium across a flat free surface. Without loss of generality, we consider the phase field profiles across a flat free surface at $x=0$ between a semi-infinite solid grain and semi-infinite amorphous/pore phase (see Figure A1(b)). In this case, both fields change across the interface and hence the specific surface energy is calculated from the integral

$$\gamma^{\mathrm{s}} = \int_{-\infty}^{+\infty} f(\rho,\eta) + \frac{\kappa_\rho}{2}\left(\frac{\mathrm{d}\rho}{\mathrm{d}x}\right)^2 + \frac{\kappa_\eta}{2}\left(\frac{\mathrm{d}\eta}{\mathrm{d}x}\right)^2 \quad \mathrm{d}x\,. \tag{A.18}$$

Here $f(\rho,\eta)$ is the bulk free energy density (see equation (2)) when only one solid grain is present,

$$f(\rho,\eta) = B\rho^2(1-\rho)^2 + C\left[\rho^2 + 6(1-\rho)\eta^2 - 4(2-\rho)\eta^3 + 3\eta^4\right]. \tag{A.19}$$

At equilibrium, the functional (A.18) must be a minimum which requires

$$\frac{\partial f(\rho,\eta)}{\partial \eta} - \kappa_\eta\left(\frac{\mathrm{d}^2\eta}{\mathrm{d}x^2}\right) = 0\,, \tag{A.20a}$$

$$\frac{\partial f(\rho,\eta)}{\partial \rho} - \kappa_\rho\left(\frac{\mathrm{d}^2\rho}{\mathrm{d}x^2}\right) = 0\,. \tag{A.20b}$$

Upon integration, the above two equations yield

$$f(\rho,\eta) - \left[\frac{\kappa_\eta}{2}\left(\frac{\mathrm{d}\eta}{\mathrm{d}x}\right)^2 + \frac{\kappa_\rho}{2}\left(\frac{\mathrm{d}\rho}{\mathrm{d}x}\right)^2\right] = 0\,, \tag{A.21}$$

where the boundary conditions $\rho(\infty)=\eta(\infty)=1$ and $\rho(-\infty)=\eta(-\infty)=0$ were used. From Figure A1(b), one expect that the following relation to be valid:

$$\frac{\mathrm{d}\eta}{\mathrm{d}x} \propto \frac{\mathrm{d}\rho}{\mathrm{d}x}\,, \tag{A.22}$$

which, after applying the boundary conditions above, gives

$$\rho(x) = \eta(x)\,. \tag{A.23}$$

From the last equation one obtain

$$\frac{\mathrm{d}\eta}{\mathrm{d}x} = \frac{\mathrm{d}\rho}{\mathrm{d}x}\,, \tag{A.24}$$

and

$$f(\rho, \eta = \rho) = f(\rho) = (B + 7C)\rho^2 (1-\rho)^2\,. \tag{A.25}$$

According to Euler equations (B.20), such relations are valid only if $(1/\kappa_\rho)\,\partial f / \partial \rho = (1/\kappa_\eta)\,\partial f / \partial \eta$, which holds if the following relation holds

$$\frac{6C}{\kappa_\eta} = \frac{B + C}{\kappa_\rho}\,. \tag{A.26}$$

Following the procedure leading to equation (A.14) for obtaining the grain boundary energy, the surface energy is finally found to be

$$\gamma^{\mathrm{s}} = \frac{\sqrt{2}}{6}\sqrt{\kappa_\rho + \kappa_\eta}\,\sqrt{B + 7C}\,. \tag{A.27}$$

Equations (A.14), (A.17), (A.26) and (A.27) uniquely fix the unknown free energy parameters B, C, κ_ρ and κ_η in terms of the surface energy, grain boundary energy, and grain boundary width for any particular material.

Appendix B Asymptotic Analysis of the Phase Field Model

A typical procedure for carrying out an asymptotic analysis of a phase field model is by expanding the fields in terms of a small parameter, often given the symbol ε, that is related to the diffuse interface width [59-61, 113-119]. Two different expansions are usually employed, e.g., outer and inner expansions. The outer expansion describes the fields far away from the interface (in the bulk phases), and the inner expansion describes the fields in the neighborhood of the interface. Matching the solutions of the outer and inner problems deduced from these expansions in the limit $\varepsilon \to 0$ gives rise to the sharp-interface limit of the phase field (diffuse-interface) model. The matching conditions were derived and summarized several times before [59-61, 113-119], so we will not repeat that here. However, we will explicitly mention any matching condition we use here when necessary.

There are two phase field models [157, 158] that are relatively close to the one presented here in the sense that they also couple motion by mean curvature to motion by surface diffusion (motion by the surface Laplacian of the mean curvature). In [157], a phase field model of simultaneous order/disorder transition and phase separation was proposed. In that model, it was shown via asymptotic analysis that the antiphase boundary (the boundary between two variants of the ordered phase) moves by mean curvature flow while the interphase boundary (the boundary between the ordered and disordered phases) moves by surface diffusion provided that the curvature of antiphase boundary is small and the curvature of the interphase is large. While in principle the pore (free) surface can be considered as an interphase and the grain boundary as an antiphase,

the condition on the curvatures is restrictive. A pore moves by surface diffusion and a grain boundary moves by mean curvature flow regardless of their sizes/curvatures. In [158], a phase field model for the electromigration of intergranular voids was introduced. Using formal asymptotic analyses, the authors derived two different sharp-interface limits depending on the scaling of Allen-Cahn mobility. In one limit, the grain boundary was stationary while the void surface moves by surface diffusion. In the other limit, the grain boundary moves by mean curvature flow while the void surface moves by an evolution law that combines surface diffusion and surface attachment limited kinetics. As was first proposed by Taylor and Cahn [67], the evolution law that combines surface diffusion and surface attachment limited kinetics is considered to represent the general curvature-driven motion form which motion by mean curvature flow and motion by surface diffusion arise as limiting cases. Nevertheless, the two limits mentioned above do not reduce to the sharp-interface limit we seek here. Therefore, we present a different scaling that gives rise to a third limit. In this limit, the grain boundary moves by mean curvature flow and the pore surface moves by surface diffusion in agreement with the sharp-interface model (Eqs.(2.20) and (2.24)). Also note that in [158] the authors used a non-differentiable (non-smooth) obstacle potential while here we use a differentiable (smooth) multi-well potential.

Let us recast our model equations in a form similar to the one usually used in the asymptotic analyses reported in [59-61, 113-119]. The free energy (Eq. 3.1) is then rewritten as:

$$F = \int_{\Omega} [\, f(\rho, \eta_1, ..., \eta_\alpha, ..., \eta_p) + \frac{q\varepsilon^2}{2} |\nabla \rho|^2 + \frac{\varepsilon^2}{2} \sum_{\alpha=1}^{p} |\nabla \eta_\alpha|^2] \, d^3x \,. \tag{B.1}$$

Hence, $q = \kappa_\rho / \kappa_\eta$ is a constant and $\varepsilon = \sqrt{\kappa_\eta}$ is a small parameter proportional to the diffuse interface width (see Eq. A.17) Moreover, we define

$$\mu = \frac{\delta F}{\delta \rho} = \left[\partial_\rho f(\rho, \eta_1, \eta_2, ..., \eta_\alpha) - q\varepsilon^2 \nabla^2 \rho \right], \tag{B.2a}$$

$$u_\alpha = \frac{\delta F}{\delta \eta_\alpha} = \left[\partial_{\eta_\alpha} f(\rho, \eta_1, \eta_2, ..., \eta_\alpha) - \varepsilon^2 \nabla^2 \eta_\alpha \right] \quad \forall \alpha, \alpha = 1, 2....p\,. \tag{B.2b}$$

Here μ is a chemical potential and u_α is a generalized force that drives the evolution of the non-conserved order parameter, η_α. Furthermore, we make the slow time transformation $t \to \varepsilon^2 t$ suitable for the slow curvature-driven motion [157]. The dynamical system (Eqs. (3.3) and (3.6)) can then be rewritten as

$$\varepsilon^2 \partial_t \rho = \nabla \cdot M(\rho) \nabla \mu\,. \tag{B.3}$$

$$\varepsilon^2 \partial_t \eta_\alpha = -L u_\alpha \quad \forall \alpha, \alpha = 1, 2....p\,. \tag{B.4}$$

In Cahn-Hilliard equation above, we dropped its tensorial representation of the mobility and assumed that it is just function of ρ for simplicity. The projection tensor does not change the sharp-interface limit as was shown in [118]. In fact, in agreement with [118], we will show here that Cahn-Hilliard equation describes surface diffusion regardless of the form of the mobility as long as the bulk phases are in equilibrium. However, the importance of the projection tensor for numerical implementation will be discussed later.

As depicted in Figure B1 below, the order parameters behave differently in the vicinity of a grain boundary or a pore (free) surface. Hence, the complete asymptotic analysis consists of two steps to deduce the equation of motion for each interface as in [157, 158]. Here, we first deduce an equation of motion for the grain boundary and then its counterpart for the pore (free) surface. In both cases, along $\partial\Omega$, the boundary

conditions are $\mathbf{m}\cdot M\nabla\mu = \mathbf{m}\cdot\nabla\rho = \mathbf{m}\cdot\nabla\eta_\alpha = 0$ where $\mathbf{m}$ denotes the unit normal to $\partial\Omega$. Under these conditions, the system is closed and the mass of the system is prescribed by the initial conditions. The results of the asymptotic analysis would not be altered if an open system with Dirichlet type boundary conditions is considered instead.

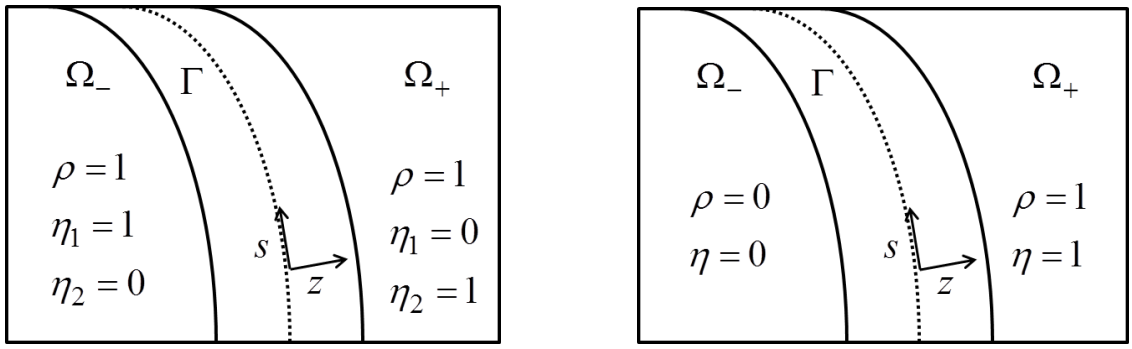

(a) (b)

Figure B1. A schematic illustration of the local coordinate system used in the asymptotic analysis showing values of the order parameters across (a) a grain boundary and (b) a free surface [58]

B.1 Derivation of the Equation of Motion of a Grain Boundary

Over a volume containing a single grain boundary (see Figure B1(a)), the free energy (Eq. (B.1)) reduces to

$$F = \int [\, f(\rho = 1, \eta_1, \eta_2) + \frac{\varepsilon^2}{2} \sum_{\alpha=1}^{2} |\nabla \eta_\alpha|^2]\, d^3x . \tag{B.5}$$

The bulk free energy density (Eq. (3.2)) is now given by

$$f(\rho = 1, \eta_1, \eta_2) = C\left[1 - 4(\eta_1^3 + \eta_2^3) + 3(\eta_1^2 + \eta_2^2)^2\right] \tag{B.6}$$

In other words, the multi-well potential given by Eq. (3.2) reduces to a double well potential (Eq. (B.6)) at a grain boundary.

Since the density is constant across a grain boundary, the dynamics is controlled by Allen-Cahn equations only. This is true as long as solute segregation is ignored. An asymptotic analysis for a phase field model of the effect of solute segregation on grain boundary motion was discussed in [125]. Hence, the dynamical system (Eqs. (B.3) and (B.4)) reduces to

$$\varepsilon^2 \partial_t \eta_\alpha = -L u_\alpha \qquad \forall \alpha,\ \alpha = 1, 2, \tag{B.7}$$

with the following initial and boundary conditions (see Figure 1(a)),

$$\eta_1(x,0) = 1 \ , \ \eta_2(x,0) = 0 \quad \forall x \in \Omega_- , \tag{B.8a}$$

$$\eta_1(x,0) = 0 \ , \ \eta_2(x,0) = 1 \quad \forall x \in \Omega_+ , \tag{B.8b}$$

$$\rho(x,0) = 1 \quad \forall x \in \Omega , \tag{B.8c}$$

$$\mathbf{m} \cdot \nabla \eta_1 = \mathbf{m} \cdot \nabla \eta_2 = 0 \quad \forall x \in \partial\Omega . \tag{B.8d}$$

In the outer region we expand the fields as

$$u_\alpha(x,t) = u_\alpha^0(x,t) + \varepsilon u_\alpha^1(x,t) + \varepsilon^2 u_\alpha^2(x,t) + \cdots \quad \forall \alpha, \alpha = 1,2 , \tag{B.9}$$

with similar expressions for η_α. Note that superscripts on ε denote exponents, while superscripts on the fields u_α, η_α, μ, and ρ denote the order in the perturbation expansion. Explicit expressions of u_α^0, u_α^1, etc. can be obtained by expanding the derivatives of the bulk free energy (Eq. B.6) in Taylor series as

$$\partial_{\eta_1} f(\eta_1,\eta_2) = \partial_{\eta_1} f(\eta_1^0,\eta_2^0) + \partial_{\eta_1}^2 f(\eta_1^0,\eta_2^0)[\varepsilon\eta_1^1 + \varepsilon^2\eta_1^2] + \partial_{\eta_2\eta_1}^2 f(\eta_1^0,\eta_2^0)[\varepsilon\eta_2^1 + \varepsilon^2\eta_2^2] + \cdots ,$$

(B.10a)

$$\partial_{\eta_2} f(\eta_1,\eta_2) = \partial_{\eta_2} f(\eta_1^0,\eta_2^0) + \partial_{\eta_1\eta_2}^2 f(\eta_1^0,\eta_2^0)[\varepsilon\eta_1^1 + \varepsilon^2\eta_1^2] + \partial_{\eta_2}^2 f(\eta_1^0,\eta_2^0)[\varepsilon\eta_2^1 + \varepsilon^2\eta_2^2] + \cdots .$$

(B.10b)

By substituting Eqs. (B.10(a) and B.10(b)) in Eq. (B.2(b)), and equating terms of the same order, we arrive at,

$$u_1^0 = \partial_{\eta_1} f(\eta_1^0, \eta_2^0), \quad u_2^0 = \partial_{\eta_2} f(\eta_1^0, \eta_2^0), \tag{B.11a}$$

$$u_1^1 = \partial_{\eta_1}^2 f(\eta_1^0, \eta_2^0)\eta_1^1 + \partial_{\eta_2\eta_1}^2 f(\eta_1^0, \eta_2^0)\eta_2^1, \; u_2^1 = \partial_{\eta_2}^2 f(\eta_1^0, \eta_2^0)\eta_2^1 + \partial_{\eta_1\eta_2}^2 f(\eta_1^0, \eta_2^0)\eta_1^1. \tag{B.11b}$$

We will need only explicit expressions for the fields up to first order in our analysis here. Substituting Eq. (B.11) in Eq. (B.7) and equating terms of the same order results in different outer equations to be solved order by order. For the leading order (ε^0) we have,

$$0 = -L u_\alpha^0 \quad \forall \alpha, \alpha = 1, 2. \tag{B.12}$$

Taking into account the initial and boundary conditions, (Eqs. (23a-d)), Eq. (27) immediately gives,

$$u_\alpha^0 = 0 \quad \forall \alpha, \alpha = 1, 2, \; \forall x \in \Omega_\pm, \tag{B.13a}$$

$$\eta_1^0 = 1, \; \eta_2^0 = 0, \; \forall x \in \Omega_-, \tag{B.13b}$$

$$\eta_1^0 = 0, \; \eta_2^0 = 1, \; \forall x \in \Omega_-. \tag{B.13c}$$

For the next-to-the leading order (ε), we obtain

$$0 = -L u_\alpha^1 \quad \forall \alpha, \alpha = 1, 2. \tag{B.14}$$

This immediately gives

$$u_\alpha^1 = 0 \quad \forall \alpha, \alpha = 1, 2, \; \forall x \in \Omega_\pm. \tag{B.15}$$

Now from the above expressions of u_α^1 and since by construction $\partial_{\eta_1\eta_2}^2 f(\eta_1^0, \eta_2^0) = \partial_{\eta_2\eta_1}^2 f(\eta_1^0, \eta_2^0) = 0$ and $\partial_{\eta_1}^2 f(\eta_1^0, \eta_2^0)$, $\partial_{\eta_2}^2 f(\eta_1^0, \eta_2^0) > 0$ when the leading order outer solutions take on their equilibrium values (given by Eqs. (B.13b) and (B.13c)), Eq. (B.15) also leads to

$$\eta_\alpha^1 = 0 \quad \forall \alpha,\, \alpha = 1,\, 2\,, \quad \forall x \in \Omega_\pm\,. \tag{B.16}$$

In other words, the leading order outer solution solves the outer problem exactly. Therefore, we have

$$u_\alpha^l = \eta_\alpha^l = 0 \quad \forall \alpha,\, \alpha = 1,\, 2\,, l > 0 \;\;, \quad \forall x \in \Omega_\pm\,. \tag{B.17}$$

Let us now define a local orthogonal coordinate system (r,s), where r is the normal distance from the point x in Ω to the interface $\Gamma(t)$, such that $r > 0$ in Ω_+ and $r < 0$ in Ω_-, and $s = \{s_1, s_2\}$ being the other two coordinates that are perpendicular to r and tangent to Γ (see Figure 1). . Moreover, since the interface width is of order ε, we further introduce a stretched variable, $z = r/\varepsilon$. Therefore, (z,s) is a local orthogonal coordinate system that moves with the interface. In the moving coordinate system (MCS), the spatial and time derivatives transform as follows:

$$\nabla^2 = \varepsilon^{-2}\partial_z^2 + \varepsilon^{-1}\kappa\partial_z + \nabla_s^2\,, \tag{B.18a}$$

$$(\partial_t)_{\mathrm{MCS}} = \partial_t + V\cdot\nabla \to \partial_t = (\partial_t)_{\mathrm{MCS}} - \varepsilon^{-1}V^n\partial_z\,. \tag{B.18b}$$

In the above, ∇_s^2 is the 2D surface Laplacian, V^n is the normal velocity of the interface with respect to a stationary frame of reference, and κ is the curvature of the interface, which is positive when the center of curvature lies within Ω_-. We will drop the subscript (MCS) in the following.

In the inner region, we expand the fields as

$$\tilde{u}_\alpha(z,s,t) \equiv u_\alpha(r,s,t) = \tilde{u}_\alpha^0(z,s,t) + \varepsilon\tilde{u}_\alpha^1(z,s,t) + \varepsilon^2\tilde{u}_\alpha^2(z,s,t) + \cdots \quad \forall \alpha, \alpha = 1,2\,, \tag{B.19}$$

with similar expressions for other field quantities. Again, similar to the outer expansion, we can get explicit expressions for these terms. By using Eqs. (26a), (33a) and (17b), we get

$$\tilde{u}_1^0 = \partial_{\tilde{\eta}_1} f(\tilde{\eta}_1^0, \tilde{\eta}_2^0) - \partial_z^2 \tilde{\eta}_1^0 \ , \ \tilde{u}_2^0 = \partial_{\tilde{\eta}_2} f(\tilde{\eta}_1^0, \tilde{\eta}_2^0) - \partial_z^2 \tilde{\eta}_2^0 , \tag{B.20a}$$

$$\tilde{u}_1^1 = \partial_{\tilde{\eta}_1}^2 f(\tilde{\eta}_1^0, \tilde{\eta}_2^0) \tilde{\eta}_1^1 + \partial_{\tilde{\eta}_1 \tilde{\eta}_2}^2 f(\tilde{\eta}_1^0, \tilde{\eta}_2^0) \tilde{\eta}_2^1 - \kappa \partial_z \tilde{\eta}_1^0 - \partial_z^2 \tilde{\eta}_1^1 , \tag{B.20b}$$

$$\tilde{u}_2^1 = \partial_{\tilde{\eta}_2}^2 f(\tilde{\eta}_1^0, \tilde{\eta}_2^0) \tilde{\eta}_2^1 + \partial_{\tilde{\eta}_2 \tilde{\eta}_1}^2 f(\tilde{\eta}_1^0, \tilde{\eta}_2^0) \tilde{\eta}_1^1 - \kappa \partial_z \tilde{\eta}_2^0 - \partial_z^2 \tilde{\eta}_2^1 . \tag{B.20c}$$

Therefore, the inner equations can now be written as

$$\varepsilon^2 \partial_t \tilde{\eta}_\alpha - \varepsilon v \partial_z \tilde{\eta}_\alpha = -L \tilde{u}_\alpha \qquad \forall \alpha, \ \alpha = 1, 2 . \tag{B.21}$$

Here v is the interface (front) normal velocity in the slow timescale defined above. Again, the above inner equations must be solved simultaneously order by order. For the leading order (ε^0), we have

$$0 = -L \tilde{u}_\alpha^0 \ \forall \alpha, \ \alpha = 1, 2 . \tag{B.22}$$

This gives

$$\tilde{u}_\alpha^0 = 0 \quad \forall \alpha, \ \alpha = 1, 2 . \tag{B.23}$$

These are basically the Euler-Lagrange equations (see Eq. (B.20a)) which, with the boundary conditions, from the outer solution, e.g., $\tilde{\eta}_\alpha^0(\pm\infty) = \eta_\alpha^0(\pm 0)$, give the equilibrium planar profiles for the order parameters [56,125]. For the next-to-the leading order (ε), we obtain

$$-v \partial_z \tilde{\eta}_\alpha^0 = -L \tilde{u}_\alpha^1 \ \forall \alpha, \ \alpha = 1, 2 . \tag{B.24}$$

Following the standard procedure implemented in all previous asymptotic analyses [59-61, 113-119], we multiply each equation by its corresponding $\partial_z \tilde{\eta}_\alpha^0$ and integrate from

$z \to -\infty$ to $z \to +\infty$. Performing integration by parts on the first and fourth terms of the right hand sides (see Eqs. (B.20b) and (B.20c)) and taking into account that the leading order profiles satisfy Euler-Lagrange equations, one obtains

$$\frac{v\gamma_1}{\varepsilon} = L(A - \frac{\kappa\gamma_1}{\varepsilon}), \tag{B.25a}$$

$$\frac{v\gamma_2}{\varepsilon} = -L(A + \frac{\kappa\gamma_2}{\varepsilon}). \tag{B.25b}$$

In the above, $A(s,t) = \int_{-\infty}^{+\infty} (\tilde{\eta}_1^1 \partial_z \tilde{\eta}_2^0 - \tilde{\eta}_2^1 \partial_z \tilde{\eta}_1^0)\, \partial^2_{\tilde{\eta}_1 \tilde{\eta}_2} f(\tilde{\eta}_1^0, \tilde{\eta}_2^0)\, dz$, and $\gamma_\alpha = \int_{-\infty}^{+\infty} \varepsilon (\partial_z \tilde{\eta}_\alpha^0)^2 dz$ such that the total grain boundary energy is $\gamma^{gb} = \gamma_1 + \gamma_2$. Hence, by eliminating A from the above two equations, we arrive at the desired result:

$$V^n = -L\varepsilon^2 \kappa. \tag{B.26}$$

Comparing this with its sharp-interface counterpart (Eq. (2.20)), we get the relation

$$L\varepsilon^2 = \gamma^{gb} M_b. \tag{B.27}$$

B.2 Derivation of the Equation of Motion of a Free (Pore) Surface

Consider a volume containing a free surface between the pore phase and a solid grain (see Figure B1(b)), the free energy (Eq. (B.1)) reduces to,

$$F = \int [f(\rho,\eta) + \frac{q\varepsilon^2}{2} |\nabla\rho|^2 + \frac{\varepsilon^2}{2} |\nabla\eta|^2]\, d^3x. \tag{B.28}$$

The bulk free energy (Eq. (3.2)) reduces to

$$f(\rho,\eta) = B\rho^2(1-\rho)^2 + C[\rho^2 + 6(1-\rho)\eta^2 - 4(2-\rho)\eta^3 + 3\eta^4]. \tag{B.29}$$

Hence at a pore surface the multi-well potential reduces to a double well potential reflecting the two equilibrium phases (see Figure B1(b)). Noting that $L = \gamma^{gb} M_b \varepsilon^{-2}$ (from Eq. (B.27)), the dynamical system (Eqs. (B.3) and (B,4)) reduces to

$$\varepsilon^2 \partial_t \rho = \nabla \cdot M(\rho) \nabla \mu , \tag{B.30a}$$

$$\varepsilon^4 \partial_t \eta = -\gamma^{gb} M_b u . \tag{B.30b}$$

with the following initial and boundary conditions (see Figure B1(b)),

$$\eta(x,0) = 0 \ , \ \rho(x,0) = 0 \ , \ \forall x \in \Omega_- , \tag{B.31a}$$

$$\eta(x,0) = 1 \ , \ \rho(x,0) = 1 \ , \ \forall x \in \Omega_+ , \tag{B.31b}$$

$$\mathbf{m} \cdot \nabla \eta = \mathbf{m} \cdot \nabla \rho = \mathbf{m} \cdot M \nabla \mu = 0, \ \ \forall x \in \partial\Omega . \tag{B.31c}$$

Performing an outer expansion as before, and substituting in Eqs. (B.2a) and (B.2b), we obtain

$$\mu^0 = \partial_\rho f(\rho^0, \eta^0) , \quad \mathrm{u}^0 = \partial_\eta f(\rho^0, \eta^0) , \tag{B.32a}$$

$$\mu^1 = \partial_\rho^2 f(\rho^0, \eta^0) \rho^1 + \partial_{\rho\eta}^2 f(\rho^0, \eta^0) \eta^1 \ , \ \mathrm{u}^1 = \partial_\eta^2 f(\rho^0, \eta^0) \eta^1 + \partial_{\eta\rho}^2 f(\rho^0, \eta^0) \rho^1 . \tag{B.32b}$$

The outer equations can now be solved as follows. For the leading order (ε^0) we have,

$$0 = \nabla \cdot M(\rho^0) \nabla \mu^0 , \tag{B.33a}$$

$$0 = -\gamma^{gb} M_b u^0 . \tag{B.33b}$$

When the initial and boundary conditions (Eqs. (B.31a)-(B.31c)) are taken into account, this gives

$$u^0 = \mu^0 = 0 \ , \ \ \forall x \in \Omega_\pm , \tag{B.34a}$$

$$\rho^0 = \eta^0 = 0 \ , \ \ \forall x \in \Omega_- , \tag{B.34b}$$

$$\rho^0 = \eta^0 = 1 \ , \ \ \forall x \in \Omega_+ . \tag{B.34c}$$

For the next-to-the leading order (ε), we obtain

$$0 = \nabla \cdot M(\rho^0)\nabla\mu^1, \tag{B.35a}$$

$$0 = -\gamma^{gb} M_b \, u^1. \tag{B.35b}$$

Hence we also deduce that

$$u^1 = \mu^1 = 0 \ , \ \forall x \in \Omega_{\pm}, \tag{B.36a}$$

$$\eta^1 = \rho^1 = 0 \ , \ \forall x \in \Omega_{\pm}. \tag{B.36b}$$

In the above, we deduced Eq. (B.36b) from (B.36a) using the same argument we utilized before in deriving Eq. (B.16) from Eq. (B.15). Therefore, once again the outer problem is solved exactly by the leading order outer solution and we have

$$u^l = \mu^l = \eta^l = \rho^l = 0 \ , \ l > 0 \ , \ \forall x \in \Omega_{\pm}. \tag{B.37}$$

In the vicinity of the free surface, we define an orthogonal coordinate system as before. The spatial and time derivatives are exactly as in Eq. (33). Additionally, here we have

$$\nabla \cdot (M\nabla\mu) = \varepsilon^{-2}\partial_z(\tilde{M}\partial_z\tilde{\mu}_\alpha) + \varepsilon^{-1}\tilde{M}\kappa\partial_z\tilde{\mu} + \nabla_s \cdot (\tilde{M}\nabla_s\tilde{\mu}), \tag{B.38}$$

where ∇_s and $\nabla_s \cdot$ are the 2D surface gradient and divergence, respectively. We then proceed by performing an inner expansion of the fields as before. We can then find explicit expressions for the different orders of $\tilde{\mu}$ and $\tilde{u}$ as follows,

$$\tilde{\mu}^0 = \partial_{\tilde{\rho}} f(\tilde{\rho}^0, \tilde{\eta}^0) - q\partial_z^2\tilde{\rho}^0 \ , \ \tilde{\mathrm{u}}^0 = \partial_{\tilde{\eta}} f(\tilde{\rho}^0, \tilde{\eta}^0) - \partial_z^2\tilde{\eta}^0, \tag{B.39a}$$

$$\tilde{\mu}^1 = \partial_{\tilde{\rho}}^2 f(\tilde{\rho}^0, \tilde{\eta}^0)\,\tilde{\rho}^1 + \partial_{\tilde{\rho}\tilde{\eta}}^2 f(\tilde{\rho}^0, \tilde{\eta}^0)\tilde{\eta}^1 - \mathrm{q}\kappa\partial_z\tilde{\rho}^0 - q\partial_z^2\tilde{\rho}^1, \tag{B.39b}$$

$$\tilde{u}^1 = \partial_{\tilde{\eta}}^2 f(\tilde{\rho}^0, \tilde{\eta}^0)\tilde{\eta}^1 + \partial_{\tilde{\eta}\tilde{\rho}}^2 f(\tilde{\rho}^0, \tilde{\eta}^0)\,\tilde{\rho}^1 - \kappa\partial_z\tilde{\eta}^0 - \partial_z^2\tilde{\eta}^1. \tag{B.39c}$$

Hence the inner equations can now be written as

$$\varepsilon^4 \partial_t \tilde{\rho} - \varepsilon^3 v \partial_z \tilde{\rho} = \partial_z (M(\tilde{\rho}^0) \partial_z \tilde{\mu}) + \varepsilon M(\tilde{\rho}^0) \kappa \partial_z \tilde{\mu} + \varepsilon^2 \nabla_s \cdot (M(\tilde{\rho}^0) \nabla_s \tilde{\mu}), \quad \text{(B.40a)}$$

$$\varepsilon^4 \partial_t \tilde{\eta} - \varepsilon^3 v \partial_z \tilde{\eta} = -\gamma^{gb} M_b \tilde{u}. \quad \text{(B.40b)}$$

The inner equations must be solved simultaneously. For the leading order (ε^0) we have,

$$0 = \partial_z (M(\tilde{\rho}^0) \partial_z \tilde{\mu}^0), \quad \text{(B.41a)}$$

$$0 = -\gamma^{gb} M_b \tilde{u}^0. \quad \text{(B.41b)}$$

The above equations to be solved with boundary conditions that can be derived from the outer solutions via the matching conditions: $\partial_z \tilde{\mu}^0(\pm\infty) = 0$, $\tilde{\mu}^0(\pm\infty) = \mu^0(\pm 0) = 0$ and $\tilde{u}^0(\pm\infty) = u^0(\pm 0) = 0$; this gives

$$\tilde{u}^0 = \tilde{\mu}^0 = 0. \quad \text{(B.42)}$$

Therefore, once again, these are simply the Euler-Lagrange equations (see Eq. (B.39a)). When these equations are supplemented with the boundary conditions from the outer solution, e.g., $\tilde{\rho}^0(\pm\infty) = \rho^0(\pm 0)$ and $\tilde{\eta}^0(\pm\infty) = \eta^0(\pm 0)$, they give the equilibrium planar profiles for the order parameters [56, 125]. For the next-to-the leading order (ε), we obtain (recall that $\tilde{\mu}^0 = 0$)

$$0 = \partial_z (M(\tilde{\rho}^0) \partial_z \tilde{\mu}^1), \quad \text{(B.43a)}$$

$$0 = -\gamma^{gb} M_b \tilde{u}^1. \quad \text{(B.43b)}$$

Taking into account the matching condition $\partial_z \tilde{\mu}^1(\pm\infty) = \partial_r \mu^0(\pm 0) = 0$, this leads to

$$\tilde{\mu}^1 = e(s,t), \quad \text{(B.44a)}$$

$$\tilde{u}^1 = 0 . \tag{B.44b}$$

Here $e(s,t)$ is a function that does not depend on z, which is to be determined. To accomplish that, we follow the same procedure we conducted before, i.e., we multiply Eq. (B.44a) by $\partial_z \tilde{\rho}^0$ and Eq. (B.44b) by $\partial_z \tilde{\eta}^0$ and integrate in z from $-\infty$ to $+\infty$, we get

$$\tilde{\mu}^1 = A_1 - \frac{\kappa \gamma_\rho}{\varepsilon} , \tag{B.45a}$$

$$0 = A_1 + \frac{\kappa \gamma_\eta}{\varepsilon} . \tag{B.45b}$$

In the above, $A_1(s,t) = \int_{-\infty}^{+\infty} (\tilde{\rho}^1 \partial_z \tilde{\eta}^0 - \tilde{\eta}^1 \partial_z \tilde{\rho}^0)\, \partial^2_{\tilde{\rho}\tilde{\eta}} f(\tilde{\rho}^0, \tilde{\eta}^0)\, dz$, $\gamma_\rho = \int_{-\infty}^{+\infty} q\varepsilon (\partial_z \tilde{\rho}^0)^2 dz$, and $\gamma_\eta = \int_{-\infty}^{+\infty} \varepsilon (\partial_z \tilde{\eta}^0)^2 dz$ such that the total surface energy is given as $\gamma^s = \gamma_\rho + \gamma_\eta$. From the above two equations, one obtains

$$\tilde{\mu}^1 = \frac{-\kappa \gamma^s}{\varepsilon} . \tag{B.46}$$

For the next order (ε^2), we have (where the fact that $\tilde{\mu}^0 = \partial_z \tilde{\mu}^1 = 0$ was taken into account)

$$0 = \partial_z (M(\tilde{\rho}^0) \partial_z \tilde{\mu}^2) , \tag{B.47a}$$

$$0 = -\gamma^{gb} M_b \tilde{u}^2 . \tag{B.47b}$$

In conjunction with the matching condition $\partial_z \tilde{\mu}^2(\pm\infty) = \partial_r \mu^1(\pm 0) = 0$, we arrive at

$$\tilde{u}^2 = \partial_z \tilde{\mu}^2 = 0 . \tag{B.48}$$

The front velocity can be obtained at order (ε^3). At this level, it suffices to consider only Eq. (B.40a) which gives (recall that $\partial_z \tilde{\mu}^2 = 0$),

$$-v\partial_z\tilde{\rho}^0 = \nabla_s\cdot(\tilde{M}\nabla_s\tilde{\mu}^1) = \frac{-\gamma^s}{\varepsilon}M(\tilde{\rho}^0)\nabla_s^2\kappa \tag{B.49}$$

In Eq. (B.49) above we have used the fact that $\tilde{\rho}^0$ does not depend on s. Multiplying Eq. (B.49) by $\partial_z\tilde{\rho}^0$ and integrating in z from $-\infty$ to $+\infty$ produces,

$$v\frac{\gamma_\rho}{q\varepsilon} = \frac{\gamma^s\bar{M}^s}{\varepsilon}\nabla_s^2\kappa\,, \tag{B.50}$$

where $\bar{M}^s = \int_{-\infty}^{+\infty} M(\tilde{\rho}^0)\partial_z\tilde{\rho}^0 dz = \int_0^1 M(\rho^0)d\rho^0$.

Note that $\bar{M}^s$ is finite whether $M\to 0$ for $z\to\pm\infty$ or simply a constant. Hence, in agreement with [118], we show that as far as the asymptotic analysis is concerned, the Cahn-Hilliard equation recovers surface motion by surface diffusion regardless of the form of the mobility as long as the outer solutions for the order parameters represent the equilibrium bulk phases. Nonetheless, using interpolation functions and projection tensors as in Eq. (3.4) to represent surface diffusion in phase field models is important from numerical point of view. Recall that we conclude that the normal gradient of the chemical potential is zero in the interfacial region ($\partial_z\tilde{\mu}=0$) using matching conditions that assume $\varepsilon\to 0$. However, in any numerical implementation the diffuse interface width is finite, and hence non-zero normal fluxes may exist in the interfacial region during simulations. The projection tensor ensures that the normal fluxes in the interfacial region vanish even if the normal gradients of the chemical potential are non-zero. On the other hand, the interpolation function ensures the bulk fluxes vanish even if the numerical values of the order parameters differ slightly from their equilibrium values due to any

numerical errors. However, this is usually negligible, and hence using interpolation functions is often unnecessary.

Finally, restoring the physical unit of the velocity, Eq. (B.50) becomes,

$$V^n = (1+q)\bar{M}^s \varepsilon^2 \nabla_s^2 \kappa . \tag{B.51}$$

In obtaining Eq. (B.51) we used the relation $q = \gamma_\rho / \gamma_\eta$, and hence $\gamma^s / \gamma_\rho = (1+q)/q$ which arises from the similar behavior of the equilibrium profiles a cross a free surface (see Appendix A for details). By comparing Eq. (B.51) with its sharp-interface counterpart, Eq. (2.24), we obtain the relation

$$(1+q)\bar{M}^s \varepsilon^2 = \frac{\gamma^s D_s w \upsilon_m}{RT} . \tag{B.52}$$

So far we have shown that the equations of motions for the free (pore) surface and the grain boundary in the phase field model reduce to their counterparts in sharp-interface model. However, in order to prove that the phase field model completely recovers the sharp-interface model, the boundary conditions at the triple-junction, namely the balance of forces, fluxes and continuity of chemical potential must be derived. Such derivation was presented in the phase field models [157, 158] which have the same structure as the one presented here as we mentioned in the beginning of this section. Their derivation is readily applicable to our model, and hence we will not repeat it here

VITA

VITA

Education

2003-2008 : B.SC., Nuclear Engineering, Alexandria University, Alexandria, Egypt.

2009-2011 : M.SC., Materials Science, Florida State University, Tallahassee, Florida, USA.

2012-2015 (expected) : Ph.D., Nuclear Engineering, Purdue University, West Lafayette, Indiana, USA.

Experience

- 2009-2011: Research Assistant, Department of Scientific Computing, Florida State University. We developed a novel phase field model of sintering in thermal barrier coatings.
- Summer 2011: Research Intern, Department of Mathematics and Computer Science, Argonne National Laboratory. I worked on developing numerical algorithms for phase field models of radiation effects in irradiated materials.
- 2012-present : Research Assistant, School of Nuclear Engineering, Purdue University. We introduced a novel phase field model of grain growth in porous ceramics. We have performed the first 3D simulations of grain growth in porous solids. We also presented a systematic approach to construct phase field (diffuse-interface) models of microstructure evolution in irradiated materials. The work is supported by the Center for Materials Science of Nuclear Fuel, an Energy Frontier Research Center funded by the U.S. Department of Energy, Office of Sciences, Office of Basic Energy Sciences.
- Spring 2014: Teaching Assistant, School of Nuclear Engineering, Purdue University, "Radiation Effects and Reactor Materials" (NUCL520). I helped students to develop a good understanding of the mechanisms of radiation damage and the microstructural evolution processes that lead to drastic changes of the physical properties of materials.
- February 2015- August 2015: Research Intern, Fuel Modeling and Simulation Department, Idaho National Laboratory. Investigating the kinetics of grain growth in porous solids using the mesoscale simulator MARMOT. MARMOT is a MOOSE (Multiphysics Object Oriented Simulation Environment) based application developed at INL to simulate microstructure evolution in materials under extreme conditions using phase field methods. The findings of this study

- will be incorporated into the nuclear fuel performance code BISON to account for the effect of microstructure evolution on the fuel performance.

Skills

- Languages: Arabic and English.
- Computer skills: Windows, MAC, and Linux Operating Systems, Microsoft Office, Matlab, Python, Fortarn90, C++, Parallel Computing (OpenMP, OpenMPI), PETSc, MOOSE, LAMMPS, ORCA, SEQQUEST.
- Techniques of Multi-Scale Modeling of Materials: Phase-field methods, Finite-element methods, Monte-Carlo methods, Molecular Dynamics, Density Functional Theory.
- Continuum mechanics, Thermodynamics, Chemical Kinetics, Statistical Mechanics, Quantum Mechanics, Mathematical Modeling, Numerical Analysis.

Honour & Affiliations

- Golden Key International Honour Society (GK)
- Gold prize poster award in the Third International Symposium on Phase Field Method, 2014, State College, PA.
- Materials Research Society (MRS)
- The Minerals, Metals and Materials Society (TMS)

Technical Presentations

- **Karim Ahmed**, Anter El-Azab, Srujan Rokkam, and Thomas Hochrainer, " Asymptotic matching of diffuse- and sharp- interface models of void growth in irradiated solids" Seventh International Conference on Multiscale Materials Modeling, 2014, Berkeley, CA.
- **Karim Ahmed**, Anter El-Azab, Srujan Rokkam, and Thomas Hochrainer, " Diffuse interface modeling of void growth in irradiated materials" Third International Symposium on Phase Field Method, 2014, State College, PA.
- **Karim Ahmed** and Anter El-Azab, "Computational modeling of grain growth in porous uranium dioxide" TMS, 2013, San Antonio, TX.
- **Karim Ahmed** and Anter El-Azab, "phase field modeling of grain growth in porous ceria" MRS, 2012, Boston, MA.
- **Karim Ahmed**, Srujan Rokkam, and Anter El-Azab, "Stress effects on void growth in irradiated metals" TMS, 2012, Orlando, FL.
- **Karim Ahmed**, Jie Deng and Anter El-Azab, "Computational Modeling of Microstructure Evolution in Thermal Barrier Coating Systems ", in Advanced Materials & Structures. Florida Center For Advanced Aero-Propulsion (FCAAP), 2010, Tallahassee, FL.
- Jie Deng , **Karim Ahmed**, and Anter El-Azab, "Phase Field Modeling of Sintering in Thermal Barrier Coating Systems ", in Advanced Materials &

Structures. Florida Center For Advanced Aero-Propulsion (FCAAP), 2009, Tallahassee, FL.

Publications

- **K. Ahmed** and A. El-Azab, "On two classes of phase field models for void growth and coarsening in irradiated crystalline solids" submitted to Physical Review E.
- **K. Ahmed** , T. Allen, and A. El-Azab, "phase field modeling for grain growth in porous solids" Journal of Materials Science (2015) DOI 10.1007/s10853-015-9107-9 .
- A. El-Azab, **K. Ahmed**, S. Rokkam, and T. Hochrainer, "Diffuse interface modeling of void growth in irradiated materials. Mathematical, thermodynamic and atomistic perspectives", Current Opinion in Solid State and Materials Science 18, 90, 2014.
- **K. Ahmed**, J. Pakarinen, T. Allen, and A. El-Azab, "Phase field simulation of grain growth in porous uranium dioxide", Journal of Nuclear Materials 446, 90, 2014.
- **K. Ahmed**, C. Yablinsky, A. Schulte, T. Allen and A. El-Azab, "Phase field modeling of the effect of porosity on grain growth kinetics in polycrystalline ceramics", Modelling and Simulation in Materials Science Engineering , 21, 065005, 2013.
- **K. Ahmed**, J. Deng and A. El-Azab, "Computational Modeling of the Sintering Process in Thermal Barrier Coating Systems ", In the Proceedings of The Fifth International Conference on Multiscale Materials Modeling MMM 2010.
- **K. Ahmed**, J. Deng and A. El-Azab, "Computational Modeling of Microstructure Evolution in Thermal Barrier Coating Systems ", In the Proceedings of FCAAP Annual Technical Symposium, Advanced Materials & Structures Section (paper number 2, pp. 1-6).2010.
- J. Deng, **K. Ahmed** and A. El-Azab, "Phase Field Simulation of Sintering of Thermal Barrier Coatings," In the Proceedings of FCAAP Annual Technical Symposium , Advanced Materials Section (paper number 1, pp. 1-6). 2009.

PUBLICATIONS

PUBLICATIONS

- **K. Ahmed** and A. El-Azab, "On two classes of phase field models for void growth and coarsening in irradiated crystalline solids" submitted to Physical Review E.
- **K. Ahmed** , T. Allen, and A. El-Azab, "phase field modeling for grain growth in porous solids" Journal of Materials Science (2015) DOI 10.1007/s10853-015-9107-9 .
- A. El-Azab, **K. Ahmed**, S. Rokkam, and T. Hochrainer, "Diffuse interface modeling of void growth in irradiated materials. Mathematical, thermodynamic and atomistic perspectives", Current Opinion in Solid State and Materials Science 18, 90, 2014.
- **K. Ahmed**, J. Pakarinen, T. Allen, and A. El-Azab, "Phase field simulation of grain growth in porous uranium dioxide", Journal of Nuclear Materials 446, 90, 2014.
- **K. Ahmed**, C. Yablinsky, A. Schulte, T. Allen and A. El-Azab, "Phase field modeling of the effect of porosity on grain growth kinetics in polycrystalline ceramics", Modelling and Simulation in Materials Science Engineering , 21, 065005, 2013.
- **K. Ahmed**, J. Deng and A. El-Azab, "Computational Modeling of the Sintering Process in Thermal Barrier Coating Systems ", In the Proceedings of The Fifth International Conference on Multiscale Materials Modeling MMM 2010.
- **K. Ahmed**, J. Deng and A. El-Azab, "Computational Modeling of Microstructure Evolution in Thermal Barrier Coating Systems ", In the Proceedings of FCAAP Annual Technical Symposium, Advanced Materials & Structures Section (paper number 2, pp. 1-6).2010.
- J. Deng, **K. Ahmed** and A. El-Azab, "Phase Field Simulation of Sintering of Thermal Barrier Coatings," In the Proceedings of FCAAP Annual Technical Symposium , Advanced Materials Section (paper number 1, pp. 1-6). 2009.